SPONTANEOUS AND STIMULATED LIGHT EMISSION

DUE TO RADIATIVE RECOMBINATION IN

FORWARD BIASED LEAD TELLURIDE P-N JUNCTIONS

Thesis by

Peter John Andrew Zoutendyk

In Partial Fulfillment of the Requirements

For the Degree of

Doctor of Philosophy

California Institute of Technology
Pasadena, California

1968

(Submitted April 26, 1968)

ACKNOWLEDGEMENT

To my wife

Nancy

ABSTRACT

Since the discovery in 1962 of laser action in semiconductor diodes made from GaAs, the study of spontaneous and stimulated light emission from semiconductors has become an exciting new field of semi-conductor physics and quantum electronics combined. Included in the limited number of direct-gap semiconductor materials suitable for laser action are the members of the lead salt family, i.e. PbS, PbSe and PbTe. The material used for the experiments described herein is PbTe. The semiconductor PbTe is a narrow band-gap material (E_g = 0.19 electron volt at a temperature of $4.2^{\circ}K$). Therefore, the radiative recombination of electron-hole pairs between the conduction and valence bands produces photons whose wavelength is in the infrared ($\lambda \approx 6.5$ microns in air).

The p-n junction diode is a convenient device in which the spon-taneous and stimulated emission of light can be achieved via current flow in the forward-bias direction. Consequently, the experimental devices consist of a group of PbTe p-n junction diodes made from p-type single crystal bulk material. The p-n junctions were formed by an n-type vapor-phase diffusion perpendicular to the (100) plane, with a junction depth of approximately 75 microns. Opposite ends of the diode structure were cleaved to give parallel reflectors, thereby forming the Fabry-Perot cavity needed for a laser oscillator. Since the emission of light originates from the recombination of injected current carriers, the nature of the radiation depends on the injection mechanism.

The total intensity of the light emitted from the PbTe diodes was observed over a current range of three to four orders of magnitude. At the low current levels, the light intensity data were correlated with data obtained on the electrical characteristics of the diodes. In the low current region (region A), the light intensity, current-voltage and capacitance-voltage data are consistent with the model for photon-assisted tunneling. As the current is increased, the light intensity data indicate the occurrence of a change in the current injection mechanism from photon-assisted tunneling (region A) to thermionic emission (region B). With the further increase of the injection level, the photon-field due to light emission in the diode builds up to the point where stimulated emission (oscillation) occurs. The threshold current at which oscillation begins marks the beginning of a region (region C) where the total light intensity increases very rapidly with the increase in current. This rapid increase in intensity is accompanied by an increase in the number of narrow-band oscillating modes. As the photon density in the cavity continues to increase with the injection level, the intensity gradually enters a region of linear dependence on current (region D), i.e. a region of constant (differential) quantum efficiency.

Data obtained from measurements of the stimulated-mode light-intensity profile and the far-field diffraction pattern (both in the direction perpendicular to the junction-plane) indicate that the active region of high gain (i.e. the region where a population inversion exists) extends to approximately a diffusion length on both sides of

the junction. The data also indicate that the confinement of the oscillating modes within the diode cavity is due to a variation in the real part of the dielectric constant, caused by the gain in the medium. A value of $\tau \approx 10^{-9}$ second for the minority-carrier recombination lifetime (at a diode temperature of $20.4^{\circ}K$) is obtained from the above measurements. This value for τ is consistent with other data obtained independently for PbTe crystals.

Data on the threshold current for stimulated emission (for a diode temperature of $20.4^{\circ}K$) as a function of the reciprocal cavity length were obtained. These data yield a value of $J'_{th} = (400 \pm 80)$ amp/cm^2 for the threshold current in the limit of an infinitely long diode-cavity. A value of $\alpha = (30 \pm 15)$ cm^{-1} is obtained for the total (bulk) cavity loss constant, in general agreement with independent measurements of free-carrier absorption in PbTe. In addition, the data provide a value of $\eta_s \approx 10\%$ for the internal spontaneous quantum efficiency. The above value for η_s yields values of $t_b \approx \tau \approx 10^{-9}$ second and $t_s \approx 10^{-8}$ second for the nonradiative and the spontaneous (radiative) lifetimes, respectively.

The external quantum efficiency (η_d) for stimulated emission from diode J-2 (at $20.4^{\circ}K$) was calculated by using the total light intensity vs. diode current data, plus accepted values for the material parameters of the mercury-doped germanium detector used for the measurements. The resulting value is $\eta_d \approx 10\%$-20% for emission from both ends of the cavity. The corresponding radiative power output (at $\lambda = 6.5$ micron) is 120-240 milliwatts for a diode current of 6 amps.

Table of Contents

INTRODUCTION

Spontaneous light emission from semiconductors has been studied since about 1952 (1). Although the maser was discovered in 1954 (2), it was not until 1962 that stimulated light emission was observed from semiconductor laser diodes made of GaAs (3). Since 1962, numerous semiconductor materials have been used to produce stimulated light emission (4). Of the various methods which may be used to obtain laser action in semiconductors (4), the p-n junction diode is the most convenient. Laser action in forward-biased diodes made of lead telluride (PbTe) was first observed in 1964 (5). Aside from the fact that stimulated emission can occur at a wavelength of about 6.5 microns, very few of the details of the mechanisms involved in either the spontaneous or stimulated emission of light from PbTe diodes have been heretofore investigated.

An experimental study of the spontaneous and stimulated emission of light from a group of PbTe diodes is reported here. Because of the narrow band-gap of PbTe (about 0.2 electron-volt), the diodes must be cooled to temperatures below 100°K before diode action occurs. The spontaneous emission at low current levels is investigated in parallel with the electrical characteristics, with each type of data complementing the other. Several aspects of the stimulated emission at high current levels are investigated. Among the diode laser properties studied are the (a) spectral intensity and mode separation, (b) mode-

confinement in the diode cavity and (c) threshold current-density for laser action as a function of diode cavity length.

I. THEORY AND REVIEW

1.1 Semiconductor Theory--Lead Telluride

1.1.1 General Remarks

The semiconductor lead telluride (PbTe) is a member of the family of IV-VI compounds commonly known as lead salts. The complete lead salt group consists of PbS, PbSe and PbTe. The three members of this group are quite similar with regard to their semiconductor properties. The following paragraphs are concerned with the general properties of semiconductors, with specific reference to PbTe.

1.1.2 Crystal Binding and Structure

1.1.2.1 General considerations. There are four principal types of binding in the solid state, namely (a) the ionic bond, (b) the covalent bond, (c) the metallic bond, and (d) the Van der Waals bond. The types of bonds which are of concern in semiconductor materials are types (a) and (b), i.e., the ionic and the covalent bonds. Pure ionic bonding exists in cases where one type of atom completely gives up one (or more) electrons to another type of atom, with each atom thereby achieving a stable closed shell electron configuration. As a result, positive and negative ions are formed and the lattice binding energy is due mainly to Coulomb attraction between the ions. Crystals of this type usually form cubic structures, as in the case of the alkali halides (e.g. NaCl). On the other hand, covalent bonding exists in cases where stable electronic configurations are achieved through the sharing of electrons by several atoms. The origin of the covalent bond is the atomic sharing of paired electrons of opposite spin, a

result which follows from quantum mechanics. The only semiconductors having bonds which are purely covalent are the group IV semiconductors (e.g. Ge, Si). These materials form tetrahedral crystal arrays which allows the sharing of their four valence electrons with four nearest neighbor atoms.

All semiconductors but the group IV single element class have bonds which are a mixture of the ionic type and the covalent type. The so-called III-V semiconductors, consisting of elements from the third and fifth columns of the periodic table (e.g. GaAs), have predominantly covalent bonding but also contain an ionic bonding component. These substances generally form crystals with either the zinc blende structure or with one of the related structures.

1.1.2.2 Lead Telluride. The lead salt group belongs to a class of semiconductors whose bonding is mainly ionic in character. This class, known as polar semiconductors, tends to form crystals with one of the cubic structures. In particular, PbTe has a face-centered cubic structure like that of NaCl (hence the name "lead salt"), with a lattice spacing of 6.50Å (6). The cleavage surfaces in PbTe are the (100) crystal planes.

1.1.3 Band Structure

1.1.3.1 General considerations. The band theory of electrons in solids utilizes extensively the one-electron approximation (OEA). In short, the electronic contribution to the total wave function of a solid (which satisfies Schrodinger's equation) is constructed from single electron wave functions (wave functions involving the

coordinates of a single electron). As a result, the interactions
between the valence electrons due to their Coulomb repulsion is
ignored. These effects, namely of correlation and exchange, are
introduced as perturbations to the OEA solutions and as higher order
corrections. Examples of some special methods utilizing the OEA are
(a) the nearly-free-electron method and (b) the tight-binding method
(or linear combination of atomic orbitals).

The energy-band structure for a semiconductor crystal is illus-
trated in Figure 1-1(a). The conduction and valence bands are
separated by the band-gap (E_g). Near the band extrema in the Bril-
louin zone, the electron energy is given by

$$E(\vec{k}) = \frac{\hbar^2 k^2}{2m_e^*} \qquad (1-1)^*$$

where $\vec{k}$ is the "crystal momentum" divided by $\hbar$, $k = |\vec{k}|$, and
m_e^* is the so-called electron effective mass. For completely free
electrons m_e^* is replaced by the free-electron mass (m_0). In general,
m_e^* may be non-isotropic and therefore is a tensor of the form

$$\left(\frac{1}{m_e^*} \right)_{ij} = \frac{1}{\hbar^2} \frac{\partial^2 E}{\partial k_i \partial k_j} \qquad (1-2)$$

It follows that a minimum in the electron energy curve of the conduc-
tion band (the lowest energy band with only partial occupation or with

---

*The quantity $\hbar$ is Planck's constant divided by 2π .

$$E(\vec{k}) = \frac{\hbar^2 k^2}{2m_e^*}$$

$$E(\vec{k}) = \frac{\hbar^2 k^2}{2m_h^*}$$

Conduction Band

E_g

Valence Band

$\vec{k}$

$k = 0$

BZ Boundary
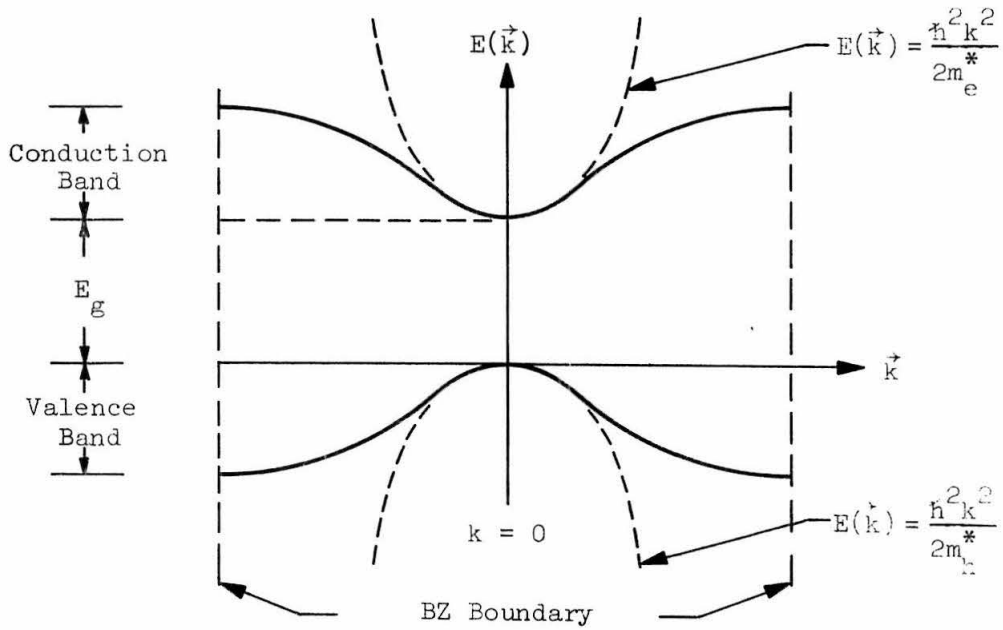
(a) Conduction and Valence Bands in the Brillouin Zone (BZ)

$E(\vec{k})$

$(\vec{k}_c)_{min} = (\vec{k}_v)_{max}$

Direct

Conduction Band

E_g

Valence Band

$E(\vec{k})$

$(\vec{k}_c)_{min} \neq (\vec{k}_v)_{max}$

Indirect

$\vec{k}$
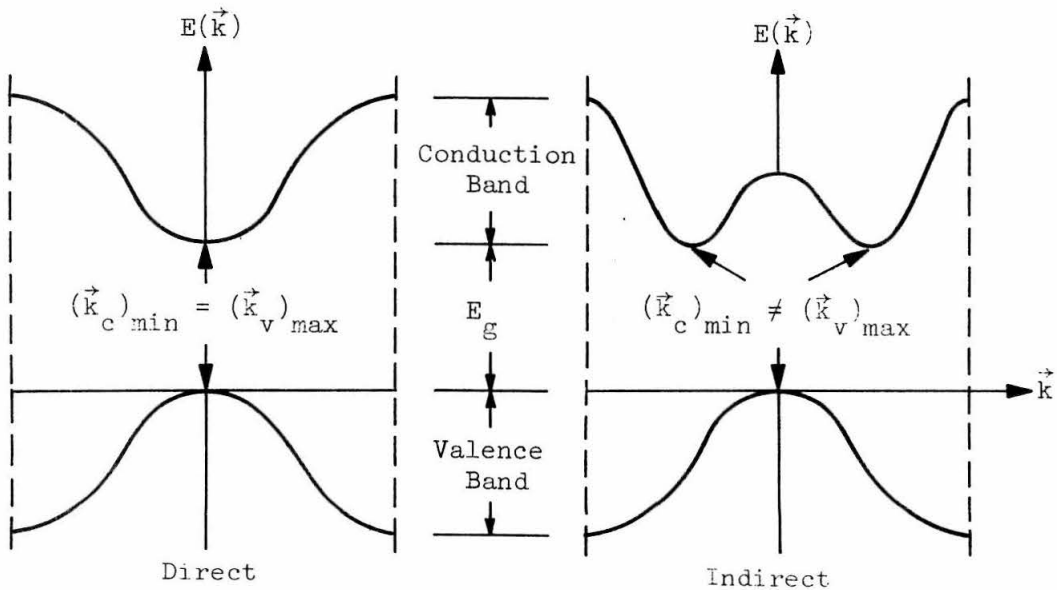
(b) Direct and Indirect Semiconductors

Figure 1-1.   Energy Bands in Semiconductors

a complete lack of occupation by electrons) will yield a positive value for the electron effective mass. Now, electrons in a completely full valence band (the band directly below the conduction band) cannot produce a net current flow in the presence of an electric field. The zero net current obtains since there are equal numbers of electrons with opposite values of momentum. This is a direct result of the inversion symmetry of energy in the reduced Brillouin zone; that is

$$E(\vec{k}) = E(-\vec{k}) \tag{1-3}$$

Therefore, a net current flow is achieved only when electrons are removed from the valence band, i.e. by introducing "holes" in the valence band. This gives rise to the concept of hole effective mass. In order to explain their transport properties, holes are assigned a positive charge and mass negative that of the electrons. It follows that a maximum in the electron energy curve of the valence band will yield a positive hole effective mass defined by

$$\left(\frac{1}{m_h^*}\right)_{ij} = -\frac{1}{\hbar^2}\frac{\partial^2 E}{\partial k_i \, \partial k_j} \tag{1-4}$$

This is the origin of the concept of electron and hole effective masses associated with electron energy minima in the conduction band and maxima in the valence band, respectively. For k-values well away from the band extrema, the energy $E(k)$ may become non-parabolic in k , as shown in Figure 1-1(a).

An important distinction for semiconductors (especially in the consideration of optical energy transitions) is that of direct and

indirect band structures. A direct semiconductor is one in which the valence band energy maximum and conduction band energy minimum occur at the same k-value in the Brillouin zone. Conversely, an indirect semiconductor is one in which the band extrema do not occur at the same k-value, as illustrated in Figure 1-1(b).

1.1.3.2 Lead Telluride. The band structure of PbTe has been studied quite extensively by a considerable number of investigators and with the aid of several experimental techniques. Band properties such as (a) the symmetry of the Fermi surfaces, (b) the location of the bands in the Brillouin zone and (c) the magnitude and energy dependence of the electron and hole effective masses have been investigated. The experimental techniques used for these investigations have included (a) Shubnikov-deHaas effect (oscillatory magnetoresistance), (b) magneto-absorption, (c) deHaas-vanAlphen (oscillatory magnetic susceptibility) effect and (d) Azbel-Kaner cyclotron resonance measurements. The major result of these studies has been the discovery of conduction band minima and valence band maxima at the L-points on the (111) faces of the Brillouin zone. (Since PbTe has a face-centered cubic crystal structure, the Brillouin zone is a truncated octahedron with eight hexagonal (111) faces. The <111> points at the center of the (111) faces are called the L-points.) The Fermi surfaces near the conduction and valence band extrema have been determined to be prolate ellipsoids of revolution centered at the L-points and with quite large effective mass anisotropies. Hence, PbTe is a direct semiconductor with four complete constant energy ellipsoids (eight halves) located

in the Brillouin zone. The best estimates of the direct energy gap (E_g) and the longitudinal and transverse effective masses at the L-point (at $4.2^{\circ}K$) have been given by Mitchell et al (7) (energy gap) and Cuff et al (8) (effective masses). These values are given in Table 1-1, with the effective masses in units of the free-electron mass (m_o). The data in Table 1-1 indicate the magnitudes of the mass anisotropies (the ratio of the longitudinal and transverse mass components (m_{ℓ}^*/m_t^*), which are 10 and 14 for the conduction and valence bands respectively.

TABLE 1-1

PbTe Band Edge Parameters at $4.2^{\circ}K$			
Band (Carriers)	(m_t^*/m_o)	(m_{ℓ}^*/m_o)	$E_g(ev)^*$
Conduction Band (electrons)	0.024 ± 0.003	0.24 ± 0.05	0.190 ± 0.002
Valence Band (holes)	0.022 ± 0.003	0.31 ± 0.05	

Cuff et al (8) have also shown the energy bands to be quite non-parabolic away from the band edges. Washwell and Cuff (9) have determined the temperature coefficient of the direct-band-gap to be

$$\frac{dE_g}{dT} = 4.4 \times 10^{-4} \text{ ev}/^{\circ}K \tag{1-5}$$

in the range of $20^{\circ}K$ to $300^{\circ}K$ (E_g increases with increasing temperature). Other investigations have demonstrated the existence of other

---

* 1 ev $\equiv$ 1 electron-volt $\equiv 1.60 \times 10^{-19}$ joule

band extrema within the Brillouin zone. Indirect, band-to-band optical absorption measurements by Tauber et al (10) have confirmed the existence of a valence band maximum at the <000> point, yielding an indirect energy gap (with the <111> conduction minima) whose value at $4.2^{O}K$ and temperature coefficient nearly match that of the direct gap. However, the direct band-gaps are of primary importance with regard to <u>radiative</u> energy transitions.

1.1.4 Intrinsic, N-type and P-type Semiconductor Materials

1.1.4.1 General considerations. The electrons in a semiconductor obey Fermi-Dirac statistics, in accordance with the Pauli exclusion principle for indistinguishable particles with half-integral spin. It then follows that for the condition of thermal equilibrium at temperature T, the probability of an electron occupying a state of energy E is given by the Fermi-Dirac distribution function

$$f(E) = \frac{1}{e^{[(E-E_F)/kT]}} \tag{1-6}$$

where E_F in equation 1-6 is the Fermi energy (level) and k is Boltzmann's constant. The density of electrons in the solid is therefore given by

$$N = \int_{-\infty}^{\infty} f(E)\, \rho(E)\, dE \tag{1-7}$$

where $\rho(E)$ in equation 1-7 is the electron density of states. For energy bands of the parabolic form given by equation 1-1, the density of states is

$$\rho(E) = \frac{1}{2\pi^2} \left(\frac{2m^*}{\hbar^2}\right)^{3/2} E^{1/2} \tag{1-8}$$

where m^* in equation 1-8 is the density-of-states effective mass (which may or may not be equal to the energy effective mass of equation 1-4). For an electron effective mass m_e^*, the density of electrons in the conduction band is

$$n = \frac{1}{2\pi^2} \left(\frac{2m_e^*}{\hbar^2}\right)^{3/2} \int_{E_c}^{\infty} \frac{(E-E_c)^{1/2} \, dE}{e^{[(E-E_F)/kT]}+1} \tag{1-9}*$$

where E_c is the electron energy at the conduction band edge. Now, for the case of holes in the valence band, the probability for hole occupation of a state of energy E at temperature T is just

$$f_p(E) = 1 - f(E) = \frac{1}{e^{[(E_F-E)/kT]}+1} \tag{1-10}$$

For the hole energy extending downward from the edge of the valence band and an effective hole mass m_n^*, the density of holes in the valence band is

$$p = \frac{1}{2\pi^2} \left(\frac{2m_h^*}{\hbar^2}\right)^{3/2} \int_{-\infty}^{E_v} \frac{(E_v-E)^{1/2} \, dE}{e^{[(E_F-E)/kT]}+1} \tag{1-11}*$$

where E_v is the hole energy at the valence band edge. With the

---

*The infinite limits of integration in equations 1-9 and 1-11 are based on the assumption that the respective conduction and valence bandwidths are much greater than kT.

following change of variables into dimensionless form, namely

$$\gamma_n \equiv (E - E_c)/kT$$

$$\gamma_p \equiv (E_v - E)/kT$$

$$\gamma_i \equiv E_g/kT = (E_c - E_v)/kT$$

$$\delta \equiv (E_F - E_c)/kT \qquad (1\text{-}12)$$

equations 1-9 and 1-11 may be written in analogous form as

$$n = N_c \int_0^\infty \frac{\gamma_n^{1/2}\, d\gamma_n}{1 + e^{(\gamma_n - \delta)}} \qquad (1\text{-}13)$$

$$p = N_v \int_0^\infty \frac{\gamma_p^{1/2}\, d\gamma_p}{1 + e^{(\gamma_p + \gamma_i + \delta)}} \qquad (1\text{-}14)$$

where

$$N_c = 2 \left(\frac{2\pi m_e^* kT}{h^2}\right)^{3/2}$$

$$\qquad (1\text{-}15)$$

and

$$N_v = 2 \left(\frac{2\pi m_h^* kT}{h^2}\right)^{3/2}$$

Equations 1-13 and 1-14 may be used to determine the Fermi level (E_F) in terms of the density of charge carriers in the two bands.

In an intrinsic semiconductor, electrons and holes are generated in their respective conduction and valence bands by the excitation of electrons from the valence band to the conduction band. Since the electrons and holes are formed in pairs, there are equal numbers of electrons in the conduction band and holes in the valence band. It

follows from this that the Fermi level in an intrinsic semiconductor lies about in the middle of the energy gap, as illustrated in Figure 1-2(a). For the condition of thermal equilibrium at a temperature T in an intrinsic semiconductor, we have

$$n = p = n_i \tag{1-16}$$

or

$$np = n_i^2 \tag{1-17}$$

with n and p given by equations 1-13 and 1-14. For cases where the energy $(E-E_F)$ is a fairly large multiple of kT , the Fermi-Dirac distribution of equation 1-6 becomes the classical Boltzmann factor, or

$$f(E) \simeq e^{[(E_F-E)/kT]} \tag{1-18}$$

In the above limit, the integrals of equations 1-13 and 1-14 yield the result

$$n_i = N_c e^{\delta} = N_v e^{-(\gamma_i+\delta)} \tag{1-19a}$$

or

$$n_i^2 = N_c N_v e^{-\gamma_i} = N_c N_v e^{-E_g/kT} \tag{1-19b}$$

From this it follows that

$$e^{\delta} = \left(\frac{N_v}{N_c}\right)^{1/2} e^{-\frac{1}{2}\gamma_i} \tag{1-20}$$

or

$$E_F = E_c - \frac{1}{2} E_g + \frac{3}{4} kT \ln \left(\frac{m_e^*}{m_h^*}\right) \tag{1-21}$$

Equation 1-21 shows that for $T = 0^{\circ}K$, the Fermi level lies exactly in

E_C

E_F

E_V

(a)   Intrinsic Semiconductor

E_C —— E_F
E_D

E_C

E_A
E_V —— E_F

n-type   p-type
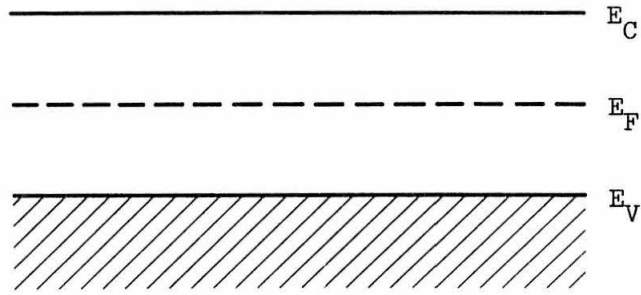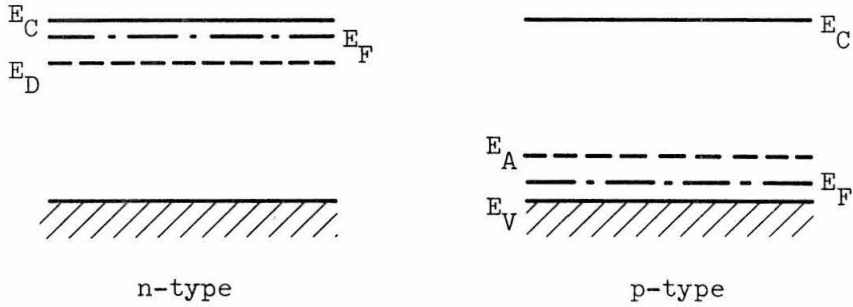
(b) Impurity Semiconductors (non-degenerate case)

E_{FC}
E_D

E_C

E_A

E_V E_{FV}

n-type   p-type
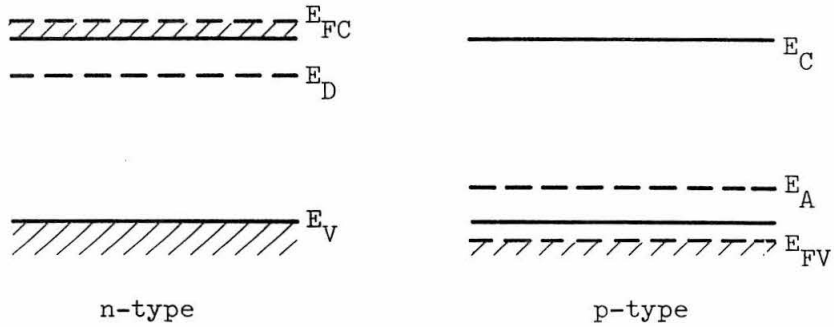
(c) Impurity Semiconductor (degenerate case)

Figure 1-2. Energy Bands in Semiconductors

the middle of the energy gap. However, for $T \neq 0^{\circ}K$, the equation demonstrates the possibility of the Fermi level lying quite far from the middle of the gap for a large difference in electron and hole effective masses and/or for large temperature values.

With the addition of impurities to a semiconductor, the mobile charge carriers derive mainly from the thermal ionization of impurity levels. The requirement of total charge neutrality yields a corresponding change in the Fermi level. For impurity states within the energy gap and near the conduction band (called donors or n-type impurities), the Fermi level shifts upward toward the conduction band. Similarly, for impurity states within the gap and near the valence band (called acceptor or p-type impurities), the Fermi level shifts toward the valence band. For the impurity dominated (extrinsic) case, the carrier concentrations n and p still obey the law of "mass-action" obtained for the intrinsic case, i.e.

$$np = n_i^2 \qquad (1-22)$$

However, for the extrinsic case

$$n \neq p \qquad (1-23)$$

For relatively low impurity concentrations (N_D or N_A), the donor and acceptor Fermi levels lie between the actual impurity energy levels and the conduction or valence band edges respectively, as illustrated in Figure 1-2(b). For impurity atom concentrations of low magnitude relative to the host lattice, the wave functions of the isolated impurity atoms do not overlap. Therefore, N impurity atoms (per unit

volume) may be regarded as N non-interacting systems, all having the same energy (i.e. and N-fold degenerate energy level). However, as the impurity concentration is increased, the impurity wave functions begin to overlap, giving rise to an interaction between the impurity atoms. This causes a banding of the energy levels, just as in the case of energy banding in the host crystal. Thus we have an impurity band within the energy gap. As still larger concentrations of impurity atoms are achieved, the impurity band of electron states begin to overlap either the conduction band (donor impurities) or the valence band (acceptor impurities). This overlapping of the host and impurity energy bands causes a perturbation in the host band parabolic density of states. Indeed, the effective density of states of the host band may now extend slightly into the energy gap, a condition known as "band-tailing". As the impurity bands approach the host bands, the corresponding Fermi levels must approach the host energy bands in advance of the actual impurity energy levels in order to satisfy equations 1-13 and 1-14. Thus, in the limit of high impurity concentrations, the impurity Fermi levels enter either the conduction or the valence band, as shown in Figure 1-2(c). When the Fermi level of an impurity-doped material enters one of the host energy bands, the material is called a degenerate semiconductor.

For parabolic energy bands, the Fermi level of a degenerate semi-conductor may be calculated using equations 1-13 and 1-14. The results for $T = 0^{\circ}K$ are

$$E_{FC} = \frac{h^2}{2m_e^*} (3\pi^2 n)^{3/2} \tag{1-24}$$

$$E_{FV} = \frac{h^2}{2m_h^*} (3\pi^2 p)^{3/2} \tag{1-25}$$

where E_{FC} and E_{FV} are the Fermi levels for the conduction and valence bands (measured from the band edges) respectively, with n and p the corresponding electron and hole densities. It should be noted that (a) any impurity (extrinsic) semiconductor can become intrinsic at temperatures for which the quantity kT approaches the value of the band gap (E_g), and (b) impurity carriers in an extrinsic semiconductor can be "frozen out" of the conduction or valence band if kT is much less than E_D or E_A, respectively. The above two facts follow directly from the temperature dependence of the Fermi-Dirac distribution function in equation 1-6.

So far we have been concerned with only the thermal equilibrium concentration of electrons in the conduction band and holes in the valence band. However, electrons and holes may be created by external means (aside from thermal excitation) in either an intrinsic or impurity semiconductor. One such means is the photo-production of electron-hole pairs, involving the excitation of electrons from the valence to the conduction band by light photons. The conservation of energy requires that

$$E_{photon} = h\nu \geq E_g \tag{1-26}$$

where ν is the photon frequency. For this case we see the need for

nonthermal equilibrium Fermi levels. In fact, we need one Fermi level
for electrons in the conduction band (E_{FC}) and one for holes in the
valence band $(E_{FV})^*$. The quantities E_{FC} and E_{FV} are called quasi-
Fermi levels. Through this or other methods of external generation of
electrons and holes, a semiconductor may be made doubly degenerate.

1.1.4.2 Lead Telluride and the hydrogen model. The polar bond-
ing in PbTe crystals yields the following ionic valencies

$$PbTe \longrightarrow Pb^{++} + Te^{--} \tag{1-27}$$

Extrinsic PbTe crystals are obtained by having either Pb or Te atoms
in excess of the stoichiometric proportions. This is done during
either the crystal growth or through a diffusion process. In the case
of excess Pb, the Pb atoms act as donors by giving up two electrons to
the lattice, or

$$Pb \longrightarrow Pb^{++} + 2 \text{ electrons} \tag{1-28}$$
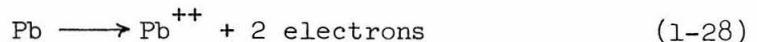
Each excess Pb atom in the lattice displaces a Te atom which has two
extra electrons. The result is a net addition of four electrons to
the lattice. Conversely, the addition of each excess Te atom in the
lattice, or

$$Te \longrightarrow Te^{--} + 2 \text{ holes} \tag{1-29}$$

results in the net addition of four holes. Thus, excess Pb or Te is
used to achieve n-type or p-type PbTe respectively.

---

* This is true only because thermal relaxation inside the bands is much
faster than between bands.

The impurity-carrier energy levels (E_D and E_A) of a semiconductor may be estimated in terms of the hydrogen model. In the hydrogen model, the ionized impurity electrons are regarded as electrons in a potential of the form

$$V(r) = \frac{-q^2}{4\pi\epsilon r} \qquad (1-30)$$

where q is the electronic charge, r is the distance from the ionized impurity atom and ϵ is the static dielectric constant of the host crystal. The impurity electron energy levels are simply obtained from a modified solution to the Schrodinger equation for the hydrogen atom, and are given by

$$E_\ell = \left[\left(\frac{m^*}{m_o}\right)\left(\frac{\epsilon_o}{\epsilon}\right)^2 \frac{1}{\ell^2} \right] E_o \qquad (1-31)$$

In equation 1-31, ℓ takes on integer values from 1 up, E_o is the ground-state energy for hydrogen (13.6 eV), ϵ_o is the permittivity of free space (8.85×10^{-14} f/cm), and (m^*/m_o) is the ratio of the impurity carrier effective mass to the free-electron mass. Equation 1-31 applies to both donor and acceptor impurities, with the electron and hole effective masses used, respectively, and where the energy is measured from the edge of the conduction or valence band, respectively. In both the donor and acceptor cases, the impurity levels lie within the energy-gap as shown in Figure 1-2; i.e. a positive amount of energy is needed to put either a donor valence electron into the conduction band or a valence band electron into an acceptor energy level. Similarly, the radii of the electron Bohr orbits (r_ℓ) are of the *modified*

form

$$r_\ell = \left[(\frac{m_o}{m^*})(\frac{\varepsilon}{\varepsilon_o}) \ell^2 \right] r_o \tag{1-32}$$

where r_o is the radius of the first Bohr orbit for hydrogen $(0.53 \times 10^{-8}$ cm$)$.

The hydrogen model is obviously best suited for singly ionized impurities, such as an As$^+$ ion replacing an un-ionized Ge atom in a covalent-bond germanium crystal. However, the salient features of this model, as expressed in equations 1-31 and 1-32 are still valid for qualitative considerations in the case of the doubly ionized "impurities" Pb^{++} and Te^{--} in n-type and p-type PbTe, respectively. Qualitatively, the small effective masses (given in Table 1-1) have the effect of reducing the impurity energy levels in a linear manner through the ratio (m^*/m_o) in equation 1-31. Even more dramatic, however, is the inverse square dependence of the impurity levels on the static dielectric constant ε . Since PbTe forms ionic crystals, there is a large ionic contribution to the dielectric constant. Specifically, we would expect that

$$(\varepsilon/\varepsilon_o) >> n_r^2 \tag{1-33}$$

where n_r is the refractive index at optical frequencies. Indeed, this turns out to be the case. The refractive index has been measured by Walton and Moss (11), yielding a value of 5.75 at (vacuum) wave-length of 6μ^* (n_r is only weakly dependent on wavelength, with a

---

*1$\mu \equiv$ 1 micron $\equiv 10^{-6}$ meter.

dispersion of only $4 \times 10^{-2}\mu^{-1}$ at 6μ). The measurement of the transverse optical phonon frequency has been used to calculate the static dielectric constant for PbTe (12), with the resultant value of 400 for (ϵ/ϵ_o). Thus we would expect the donor and acceptor energy levels in PbTe to be small by virtue of the large value for ϵ. The donor and acceptor energy levels in PbTe have been observed to be very small (13). This is based on the absence of impurity carrier "freeze out" at a temperature of 1^oK (kT has a value of 8.6×10^{-5} eV at 1^oK). The evidence for very shallow impurity levels also leads one to conclude that (a) extrinsic PbTe becomes degenerate at relatively low impurity concentrations and (b) there should be no significant amount of "band-tailing" of the host energy bands due to the impurities. Conclusion (a) is also supported by equation 1-32 in the following way. The Bohr radii of impurity electrons are increased by the linear dependence of r_ℓ on ϵ, thereby increasing the wave function overlap of the impurity electrons. This gives rise to enhanced impurity level banding and thus provides for overlap with the host bands, even for moderate impurity concentrations. Experimental evidence for conclusion (b) has been given by Washwell and Cuff (9) (radiative recombination data from bulk PbTe).

Since excess Pb or Te atoms act as donor or acceptor impurities in PbTe, the problem of purification is far more difficult than for the single element semiconductors. Not only must foreign atoms be removed, but the compound must be very nearly stoichiometric in composition. Needless to say, this makes it practically impossible to

achieve pure (intrinsic) PbTe at low temperatures. The minimum impurity concentrations achieved to date in PbTe crystals is approximately $8 \times 10^{16} cm^{-3}$ (14). The intrinsic behavior of PbTe can therefore be seen only at high enough temperatures for sufficient thermal excitation of electrons across the band-gap (above $300^{O}K$) (15).

1.2 Spontaneous and Stimulated Emission of Radiation

1.2.1 General Ideas

The emission of light from semiconductors is, as we shall see, a direct result of the (radiative) recombination of electrons in the valence band with holes in the conduction band. The frequency of emitted light photons (ν_p) is just the change in electron energy due to recombination divided by Planck's constant (h). In general terms, we may represent such a system by energy levels E_1 and E_2 ($E_2 > E_1$) , with electron occupation densities of N_1 and N_2 and energy level degeneracies g_1 and g_2, respectively. A radiative energy transition by this system will generate photons whose frequency is given by

$$\omega_p = \frac{(E_2 - E_1)}{\hbar} \tag{1-34}$$

The relative distribution of electrons in levels E_1 and E_2 under thermal equilibrium at temperature T is given (for $(E_2 - E_1) >> kT$) by the Boltzmann factor, or

$$\frac{N_2}{N_1} = \frac{g_2}{g_1} e^{-[(E_2 - E_1)/kT]} = \frac{g_2}{g_1} e^{-(\hbar\omega_p/kT)} \tag{1-35}$$

Electrons in energy level E_2 will spontaneously decay to level E_1 and thereby emit a photon. For the condition of thermal equilibrium, the spontaneous emission of photons is sustained by the thermal excitation of electrons from E_1 to E_2. However, there is an interaction between the electrons and the electric field produced by the photons in the cavity of the system. It is intuitively obvious that this interaction can result in the excitation of an electron from E_1 to E_2 via the absorption of a photon. In addition to photon absorption, the photon field may also induce (stimulate) a downward transition from E_2 to E_1 with the concomitant emission of a photon. The idea of stimulated photon emission was first postulated and treated using classical arguments by Einstein (16). The quantum mechanical treatment of stimulated emission utilizes the interaction Hamiltonian of a single electron atom with the quantized electric field $\vec{E}_p(\vec{r},t)$ associated with the photons of frequency ω_p in the cavity of the system. Assuming that the electric field has only an x component at the position of the electron $(\vec{r})$ at time t, the interaction Hamiltonian is given by

$$H = q\,\vec{E}_p(\vec{r},t) \cdot \vec{r} = q\,E_{px}(\vec{r},t)\,x \tag{1-36}$$

Using equation 1-36 and applying Fermi's golden rule, the total transition rate ($2 \to 1$) in a photon field of frequency (ω_p) is (17)

$$W' = \frac{8\pi^2 q^2\,\omega_p x_{12}^2}{V}\,(n_p+1)\,\delta(E_2 - E_1 - \hbar\omega_p) \tag{1-37}^{*}$$

---

* Here δ is the Dirac delta function.

where n_p is the number of photons, V is the volume of the radiating system, and x_{12}^2 is the square of the matrix element for an electric dipole transition from E_2 to E_1 , namely $|\langle 1|x|2\rangle|^2$. In equation 1-37 we see that the total transition rate is the sum of the spontaneous and induced rates, or

$$W' = W'_s + W'_i \qquad (1-38)$$

where

$$W'_s = \frac{8\pi^2 q^2 \omega_p x_{12}^2}{V} \delta(E_2 - E_1 - h\omega_p) \qquad (1-39)$$

and where the induced transition rate is just the spontaneous rate multiplied by the number of quanta, or

$$\frac{W'_i}{W'_s} = n_p \qquad (1-40)$$

where for thermal equilibrium n_p is given by

$$n_p = \frac{1}{e^{h\omega_p/kT} - 1} \qquad (1-41)$$

The equality $|\langle 1|x|2\rangle|^2 = |\langle 2|x|1\rangle|^2$ shows that the induced absorption rate $(1 \to 2)$ is equal to the induced emission rate. Therefore, for thermal equilibrium, the system will absorb and emit light quanta in accordance with the condition that the power absorbed equal the power emitted, or

$$N_1 W'_1 = N_2(W'_s + W'_i) \qquad (1-42)$$

with N_2/N_1 given by equation 1-35.

So far we have talked about transitions into a single mode (ω_p) only. For the total spontaneous transition rate, we must multiply 1-39 by the density of modes in energy space and integrate over all energies. The resulting total spontaneous rate for the interaction with a continuum of modes is (17)

$$W_s \equiv \frac{1}{t_s} = \frac{8\pi\, q^2 \omega^3 x_{12}^2}{hc^3} \tag{1-43a}$$

where

$$\omega = \frac{(E_2 - E_1)}{\hbar} \tag{1-43b}$$

and c is the velocity of light in the radiating medium. Equation 1-43 serves to define the spontaneous lifetime (t_s). The total induced rate is obtained by multiplying W_i' by a normalized lineshape function $g\left[\dfrac{(E_2 - E_1)}{h}\right]$ (which accounts for the fact that the atomic transitions are not exactly discrete but slightly "smeared") and again integrating over all energies. The result gives the total induced transition rate into a mode of frequency ν,

$$W_i(\nu) = \frac{8\pi^2 q^2\, \omega x_{12}^2}{h\nu}\, n_p\, g(\nu) \tag{1-44}$$

For a photon field (with a center frequency ν) whose spectral width is much less than the width of $g(\nu)$ and with a power per unit area (I_ν), the total induced rate is (17)

$$W_i(\nu) = \frac{\lambda^2\, I_\nu}{8\pi\, h\nu\, t_s}\, g(\nu) \tag{1-45a}$$

Equation 1-45 shows that the induced transition rate by a field of frequency ν is weighted by $g(\nu)$ where

$$\int_{-\infty}^{\infty} g(\nu) \, d\nu = 1 \tag{1-45b}$$

Equations 1-43 and 1-44 may be combined to show that the ratio of the total induced and spontaneous rate is just

$$\frac{W_i}{W_s} = \frac{n_p c^3}{4\pi \, \nu^2 V} \, g(\nu) \tag{1-46a}$$

Now, we may define a (spontaneous) linewidth $\Delta\nu$ by

$$\int_{-\infty}^{\infty} g(\nu) \, d\nu = [g(\nu)]_{max} \, \Delta\nu = 1$$

or

$$[g(\nu)]_{max} = \frac{1}{\Delta\nu} \tag{1-46b}$$

Assuming that $g(\nu) \simeq \frac{1}{2} [g(\nu)]_{max}$ for the stimulating field (I_ν), from 1-46a we get

$$\frac{W_i}{W_s} = \frac{n_p c^3}{8\pi \, \nu^2 \Delta\nu \, V} = \frac{n_p}{n_m} \tag{1-47a}$$

where

$$n_m = \frac{8\pi \, \nu^2 \Delta\nu \, V}{c^3} \tag{1-47b}$$

is the number of modes contributing to the total spontaneous emission. It is clear that n_m is just the density of modes in frequency space $(\frac{8\pi\nu^2 V}{c^3})$ multiplied by the spontaneous linewidth $(\Delta\nu)$. Equation 1-47a

also follows directly from 1-40 for a single stimulated mode. For several stimulated modes oscillating simultaneously, the ratio of the total stimulated emission rate to the total spontaneous emission rate is just

$$\frac{W_I}{W_s} = \frac{N_p}{n_m} \qquad (1\text{-}47c)$$

where N_p is the total number of photons in all oscillating modes.

1.2.2 Light Absorption and Amplification (Stimulated Emission)

Using the ideas developed in Section 1.2.1, we may now define the rate of change in intensity (I_ν) per unit distance traversed by a light beam of frequency (ν) through a system with electron energy levels E_1 and E_2 (etc.) as (17)

$$\frac{dI_\nu}{dx} = [N_2 W_{21} - N_1 W_{12}] \, h\nu$$

$$= -\left[N_1 \frac{g_2}{g_1} - N_2 \right] \frac{c^2 g(\nu) I_\nu}{8\pi \, \nu^2 \, t_s} \qquad (1\text{-}48)$$

The intensity will decay like $I_\nu(x) = I_\nu(0) \, e^{-\alpha(\nu)x}$, where

$$\alpha(\nu) = -\frac{dI_\nu/dx}{I_\nu} = \left[N_1 \frac{g_2}{g_1} - N_2 \right] \frac{c^2 g(\nu)}{8\pi \nu^2 \, t_s} \qquad (1\text{-}49)$$

The absorption coefficient $\alpha(\nu)$ is a positive quantity for the case of thermal equilibrium given by equation 1-35. However, if by some means the occupation number N_2 were made larger than $N_1 \frac{g_2}{g_1}$, then $\alpha(\nu)$ would become negative. The case of $\alpha(\nu) < 0$ corresponds

physically to an exponential growth of I_ν with distance, or an ampli-
fication of the photon field intensity as it traverses the material.
The condition $N_2 > N_1 \dfrac{g_2}{g_1}$ is referred to as a population inversion,
vis-a-vis the thermal equilibrium energy level populations given by
1-35. Given the condition of population inversion and hence an ampli-
fying medium, we may construct two types of devices which will utilize
the amplification. The first type of device is just a traveling wave
laser, which simply amplifies the photon field intensity by a factor
$e^{|\alpha|x}$ as it passes through the medium. With such a device, the ampli-
fication increases as the total length of the amplifier is increased.
This motivates the basis of the second type of amplifier, namely the
laser oscillator. In the laser oscillator the photon field is reflec-
ted back into the amplifying medium by providing reflecting surfaces
at each end. The oscillating modes inside the cavity must satisfy the
condition

$$m\lambda = 2Ln_r \qquad\qquad (1\text{-}50)$$

where m is an integer, λ is the photon wavelength in "free-space",
L is the length of the cavity, and n_r is the index of refraction of
the cavity material. This allows only fields of well defined frequen-
cies (or very narrow spectral bandwidths) and with a high degree of
spatial coherence to build up in the cavity. This monochromatic,
coherent radiation is brought outside the cavity by using reflectors
whose reflectivity is less than 1.

1.2.3 Direct and Indirect Radiative Transitions in Semiconductors

We have already mentioned (Section 1.1.2) the difference between direct and indirect semiconductors. If we define $(\vec{k}_c)_{min}$ and $(\vec{k}_v)_{max}$ as the electron momentum vectors at the edges of the conduction and valence bands respectively, then

$$(\vec{k}_c)_{min} = (\vec{k}_v)_{max} \tag{1-51a}$$

for a direct semiconductor and

$$(\vec{k}_c)_{min} \neq (\vec{k}_v)_{max} \tag{1-51b}$$

for an indirect semiconductor. The electron wave functions in the semiconductor are given by

$$\psi_c(\vec{r}) = u_{\vec{k}_c}(\vec{r})e^{i\vec{k}_c \cdot \vec{r}} \tag{1-51c}$$

$$\psi_v(\vec{r}) = u_{\vec{k}_v}(\vec{r})e^{i\vec{k}_v \cdot \vec{r}} \tag{1-51d}$$

for the conduction band and the valence band, respectively. For radiative transitions from the conduction band to the valence band, the matrix element x_{12} in equation 1-37 is given by

$$x_{12} = \int\limits_{space} \psi_v(\vec{r})^* x \ \psi_c(\vec{r})dV$$

$$= \int\limits_{space} e^{i(\vec{k}_c - \vec{k}_v)} u_{\vec{k}_v}^* x u_{\vec{k}_c} dV$$

$$= \delta'(\vec{k}_c - \vec{k}_v) \left\langle u_{\vec{k}_v} | x | u_{\vec{k}_c} \right\rangle \tag{1-51e}$$

where $\delta'(\vec{k}_c - \vec{k}_v)$ is one for $\vec{k}_c = \vec{k}_v$ and zero otherwise. It is clear from 1-51e that only direct transitions in which $\vec{k}_c = \vec{k}_v$ will give a nonzero matrix element (x_{12}) for radiative transitions.

The condition for a nonzero matrix element is met by a direct semiconductor, since $(\vec{k}_c)_{min} = (\vec{k}_v)_{max}$. The only way in which radiative transitions can occur in an indirect semiconductor is if the total momentum and energy is conserved. This can be obtained in the following two ways. First, the transition may take place away from the band edges with $\vec{k}_c = \vec{k}_v$. However, electrons and holes usually experience thermal relaxation to energy states near the band edges before radiative recombination can occur. Secondly, the transition may involve the emission or absorption of a lattice phonon, with momentum conservation expressed as

$$\vec{k}_c = \vec{k}_v \pm \vec{k}_{phonon} \qquad (1\text{-}52a)$$

and energy conservation as

$$\hbar\omega_{photon} = E_c - E_v \pm \hbar\omega_{phonon} \qquad (1\text{-}52b)$$

The probability for phonon-assisted radiative recombination to occur is much less than that for direct transitions. Therefore, the probability for radiative recombination is much higher in direct semiconductors than in indirect semiconductors.

1.3 Emission of Radiation due to Recombination in Semiconductor
    P-N Junction Diodes

1.3.1 General Ideas

The condition of population inversion, which was discussed in
Section 1.2 and is required for a net stimulated emission (amplifica-
tion) of radiation, can be obtained in a semiconductor material by
exciting electrons from the valence band to the conduction band by some
external means. The resulting nonthermal equilibrium condition causes
the electron and hole quasi-fermi levels to enter the conduction and
valence bands, producing a doubly degenerate situation and hence a
population inversion. Population inversion may be achieved in bulk
semiconductors by several methods, such as (a) photon absorption,
(b) electron beam excitation, and (c) avalanche production of electron-
hole pairs. Methods (a) and (b) require special external sources,
while method (c) requires extremely high applied voltages. However,
the semiconductor p-n junction diode provides, by virtue of its indi-
genous structure and electrical characteristics, an excellent scheme
for producing stimulated emission of radiation. The usual form of
semiconductor diode lasers is the laser oscillator. The necessary
feedback reflectors are formed by either cleaving or polishing two
prallel ends of the diode structure.

The energy band diagram for a degenerate p-n junction is shown in
Figure 1-3a, for the condition of zero bias $(V = 0)$. The built-in
voltage (V_B) is such that there is equal and opposite "thermionic"
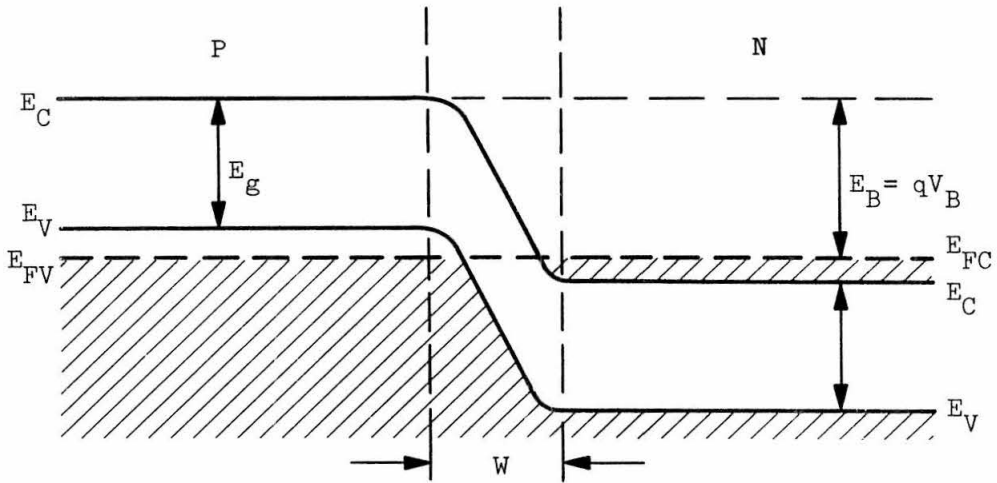current flow of magnitude I_o from the two sides of the junction,

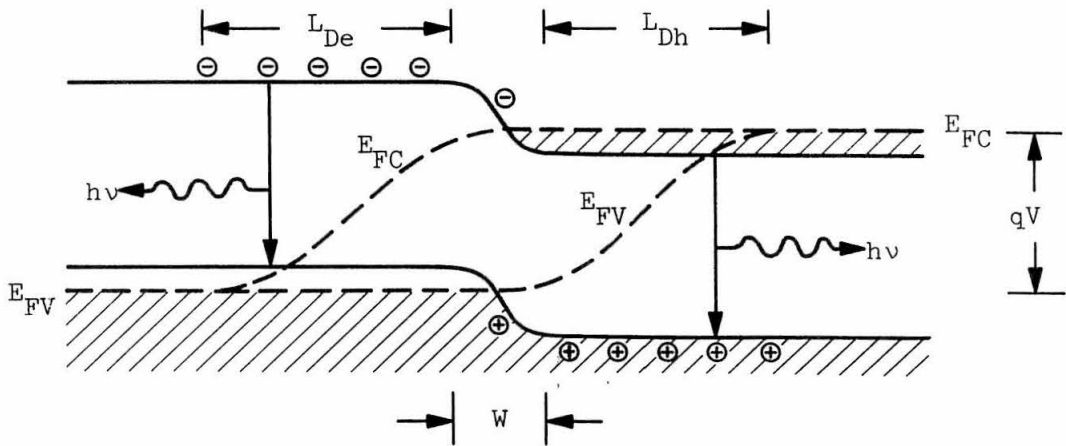Figure 1-3(a). A Degenerate P-N Junction with Zero Bias

Figure 1-3(b). A Degenerate P-N Junction with Forward Bias (V)

resulting in a net zero current. The voltage barrier V_B results from the formation of excess negative and positive bound-charge regions on the p and n sides, respectively. This excess-charge dipole layer is formed via the flow of mobile electrons from the n to the p region, required to equalize the fermi-levels on each side of the junction (a necessary condition for thermodynamic equilibrium). For an abrupt junction (i.e. homogeneous electron and hole densities on the p and n sides), the width of the dipole (depletion) layer (or junction width) is given by (18)

$$W = W_1(V_B - V)^{1/2} \qquad (1\text{-}53a)$$

with

$$W_1 \equiv (\frac{2\varepsilon}{q})^{1/2} \left[\frac{N_a + N_d}{N_a N_d}\right]^{1/2} \qquad (1\text{-}53b)$$

where N_a and N_d are the acceptor and donor densities on the p and n sides, ε is the static dielectric constant of the material, and q is the magnitude of the electronic charge.

The depletion layer of an abrupt junction behaves like a parallel plate capacitor with a capacitance per unit junction area (both differential and total) of (18)

$$C = (\frac{\varepsilon}{W_1})(V_B - V)^{-1/2} \qquad (1\text{-}54)$$

With the application of a forward bias voltage (V) (Figure 1-3b), the minority carriers injected over the barrier increase by a factor $e^{qV/\beta kT}$, while the opposing thermally generated majority carrier current remains the same (I_o). The net flow of thermionic current across

the junction is therefore given by

$$I = I_o(e^{qV/\beta kT} - 1)$$ (1-55)

where k is Boltzmann's constant and β is a numerical constant.
For large reverse bias voltages, the injected minority carrier current
approaches zero and the net current flow approaches $-I_o$. The
quantity I_o is called the saturation current. The numerical constant
(β) in equation 1-55 is determined by the amount of generation and
recombination of carriers which occurs in the depletion region, and
the minority carrier injection level (19).

The p-n junction shown in Figure 1-3 consists of degenerate p
and n materials. This condition is necessary in order to provide a
population inversion. Figure 1-3b illustrates the presence of an
effective population inversion within the junction width (w) of a
forward biased diode, as indicated by the quasi-fermi levels E_{FC} and
E_{FV} within the junction. However, the inversion may carry over into
the bulk regions beyond the junction via the injected minority car-
riers. Since the bulk regions are relatively field-free (owing to the
high conductivity of the degenerate materials used), the injected
minority carrier current flow is due mainly to diffusion. The injected
minority carrier density (n_m) decreases with a distance x from the
edge of the junction according to

$$n_m(x) = n_m(0) \, e^{-(x/L_D)}$$ (1-56a)

where

$$L_D = \sqrt{D\tau} \qquad (1\text{-}56b)$$

with D and τ being the minority carrier diffusion constant and recombination lifetime, respectively. Thus, a population inversion may persist to an approximate distance L_D from the junction, as illustrated in Figure 1-3b. The width of the active region where the emission of radiation occurs may therefore be determined by the recombination lifetime (τ).

1.3.2 Spontaneous Emission from Forward Biased Diodes

As indicated by equation 1-43a, the spontaneous emission rate (W_s) and lifetime (t_s) are independent of the emission intensity, and therefore are also independent of the injection current level. The minority carrier lifetime (τ) in equation 1-56b is the lifetime due to all recombination mechanisms in the semiconductor, including nonradiative recombination. Therefore an injected minority carrier in a forward biased diode may recombine with a majority carrier via a radiative process, at a rate W_s, or via a nonradiative process, at a rate W_b. The total recombination rate is the sum of the two

$$W_T = W_b + W_s \qquad (1\text{-}57a)$$

which is equivalent to

$$\frac{1}{\tau} = \frac{1}{t_b} + \frac{1}{t_s} \qquad (1\text{-}57b)$$

where t_b is the nonradiative recombination lifetime. The total current (I) may be written as

$$I = qn_2W_T = qn_2(W_b + W_s) \qquad (1\text{-}58a)$$

or

$$I = I_b + I_s \qquad (1\text{-}58b)$$

where n_2 is the total upper level population and I_b and I_s are
the current components due to nonradiative and radiative recombination,
respectively. It follows from 1-58 that the bulk photon emission rate
($\mathcal{R}$) is

$$\mathcal{R} \equiv \frac{I_s}{q} = \frac{I}{q}\,\eta_s \qquad (1\text{-}59a)$$

and

$$\frac{I}{q}\,\eta_s = \frac{n_2}{t_s} \qquad (1\text{-}59b)$$

where

$$\eta_s \equiv \frac{W_s}{W_T} = \frac{W_s}{W_b + W_s} = \frac{t_b}{t_s + t_b} \qquad (1\text{-}59c)$$

is defined as the (internal) spontaneous emission quantum efficiency
(the fraction of electrons and/or holes which recombine via the spon-
taneous emission of radiation). If the photon emission rate is
empirically found to have the following dependence on current

$$\mathcal{R} \sim I^m \qquad (1\text{-}60)$$

where m is a numerical constant, it then follows from 1-59a that

$$\eta_s \sim I^{m-1} \qquad (1\text{-}61a)$$

Clearly, for $m = 1$, the quantum efficiency (η_s) and t_b are indepen-
dent of current. However, for $m \neq 1$ there is a dependence of η_s

on I , given by 1-61a. Using 1-59c, 1-61a may be expressed as

$$\eta_s \equiv \frac{t_b}{t_s} \left[1 + \frac{t_b}{t_s} \right]^{-1} \sim I^{m-1} \qquad (1\text{-}61\text{b})$$

For the case of $(t_b/t_s) \ll 1$, this reduces to

$$\frac{t_b}{t_s} \sim I^{m-1}$$

and

$$\eta_s \simeq \frac{t_b}{t_s} \qquad (1\text{-}61\text{c})$$

Since t_s is independent of I, 1-61c expressed the dependence of t_b on I .

1.3.3 Stimulated Emission from Forward Biased Diodes

1.3.3.1 Gain due to stimulated emission. As was discussed in Section 1.2.2, there is a gain associated with the stimulated emission produced by an energy level population inversion. Using equation 1-49, we may write the gain per unit length for a photon field of frequency in a semiconductor diode as

$$\gamma(\nu) = \frac{(n_2 - n_1) \, c^2 \, g(\nu)}{8\pi\nu^2 \, t_s \, V} \qquad (1\text{-}62)$$

where now t_s represents the radiative recombination lifetime as discussed in Section 1.3.2. The quantity $(n_2 - n_1)/V$ takes the place of $(N_2 - \frac{g_1}{g_2} N_1)$ in equation 1-49, with n_2 and n_1 being the upper and lower energy level populations and with V now representing the volume in which the stimulated electromagnetic modes are contained. For the

case of electron injection into the p-side of the junction n_2 and n_1 are the electron populations in the conduction and valence bands, respectively.

Using 1-59b and 1-62 we may express the gain as

$$\gamma(\nu) = \frac{I\ c^2 \xi \eta_s g(\nu)}{8\pi q \nu^2\ V} \qquad (1\text{-}63a)$$

where the quantity ξ is given by

$$\xi = [1 - (n_1/n_2)] \qquad (1\text{-}63b)$$

and is called the (population) inversion factor. For sufficiently low temperatures ξ approaches a value of unity. The achievement of $\xi \simeq 1$ is, of course, possible only with degenerate semiconductor materials (20). The mode volume (V) in 1-63a is the product of the junction area (A) and the width (d) of the region containing the modes. Expressing the measured radiative (spontaneous) line width as $\Delta\nu = 1/g(\nu)$, we may write the gain as

$$\gamma(\nu) = \frac{J\ c^2\ \xi\ \eta_s}{8\pi\ qd\ \nu^2\ \Delta\nu} \qquad (1\text{-}64)$$

where J is now the current per unit junction area (I/A).

1.3.3.2 Threshold current for stimulated emission. Before the stimulated emission of radiation can occur in the forward biased p-n junction, the gain realized in one pass between the parallel faces of the diode cavity must be sufficient to overcome the losses due to the

traversal of the semiconductor medium and the imperfect reflection at the end of the cavity. This threshold condition may be expressed as

$$R \, e^{(\gamma - \alpha)L} = 1 \qquad (1\text{-}65)$$

where γ is given by 1-64, α is the effective loss coefficient for the cavity, R is the reflectivity of the cavity ends, and L is the length of the cavity. For the emission wavelengths of interest here, R is just $(n_r - 1)^2/(n_r + 1)^2$, where n_r is the index of refraction of the material. Using 1-64, the threshold condition becomes

$$J_{th} = \frac{8\pi q \, d\nu^2 \Delta\nu}{c^2 \, \xi \, n_s} \left[\alpha + \frac{1}{L} \ell n(\frac{1}{R}) \right] \qquad (1\text{-}66)$$

with J_{th} being the threshold current per unit junction area.

   1.3.3.3 Spectral separation of stimulated modes.   The spectral separation of stimulated modes, or mode-spacing, derives from the condition for constructive intereference given by 1-50. The resulting separation in terms of the change in wavelength between adjacent modes is (21)

$$\Delta\lambda = \frac{\lambda^2}{2 \, L n_r [1 - (\frac{\lambda}{n_r})(\frac{dn_r}{d\lambda})]} \qquad (1\text{-}67)$$

where λ and $\Delta\lambda$ are the "free-space" wavelength and wavelength separation, respectively, as determined experimentally in air. Again, n_r is the index of refraction of the diode material. The difference term in the denominator of 1-67 can become important if the dispersion

in the index of refraction $(dn_r/d\lambda)$ is sufficiently large.

1.3.4 Electromagnetic Mode Confinement in Laser Diodes

The volume (V) in which the electromagnetic (EM) modes producing light emission are confined in the laser diode cavity does not necessarily coincide with the volume of the active region where amplification occurs. In general, there can be a confinement of radiating modes due to variations in the real part of the dielectric constant near the active layer. This may have a lenslike focussing effect, whereby the mode intensity will be enhanced in a middle region of high dielectric constant, bounded by regions of lower dielectric constant and with spatially decaying intensities. The situation may be represented to first order by a middle region with thickness 2t and with a (real) dielectric constant $K\epsilon$ (K > 1), surrounded on both sides by regions with dielectric constant ϵ (illustrated in Figure 1-4a). The corresponding solutions to the Maxwell equations* $\vec{\nabla} \times \vec{E} = -(\partial\vec{B}/\partial t)$ and $\vec{\nabla} \times \vec{H} = (\partial\vec{D}/\partial t)$ have been examined in (22) for the additional condition that the magnitudes of $\vec{E}$ and $\vec{H}$ (the electric and magnetic field vectors) be constant in planes parallel to the junction. The solutions for the electric field in the transverse electric (TE)-even mode, propagating as $\exp(-i\beta z)$, are of the form

$$|\vec{E}| = E_y = B \cos(hx) \exp(-i\beta z) \quad \text{for} \quad |x| \leq t \qquad (1\text{-}68a)$$

---

*The vectors $\vec{B}$ and $\vec{D}$ are related to $\vec{H}$ and $\vec{E}$ by the constitutive equations $\vec{B} = \mu\vec{H}$ and $\vec{D} = \epsilon\vec{E}$.
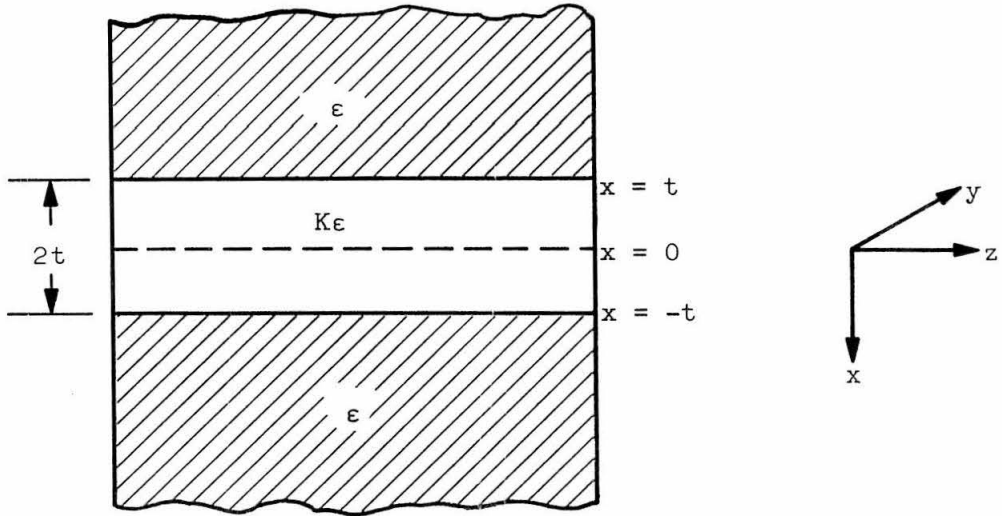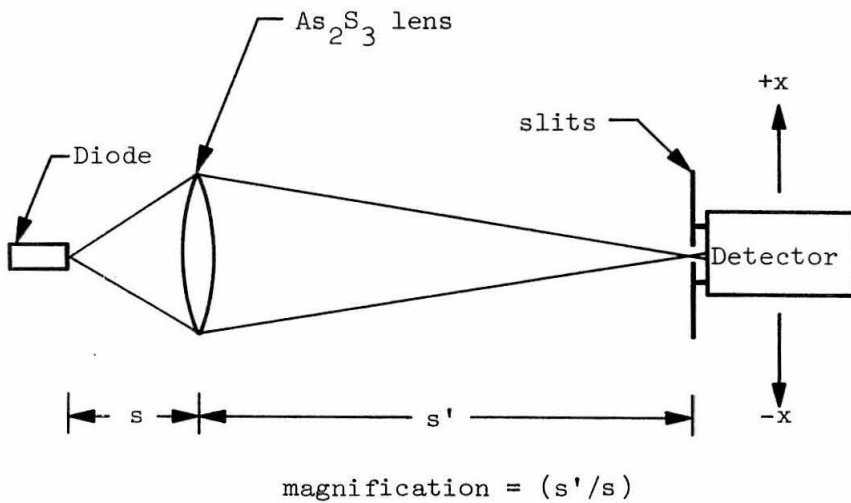
Figure 1-4(a).   Geometry of Diode Dielectric Cavity

magnification = (s'/s)

Figure 1-4(b).   Image-Scan Intensity Experiment

and

$$|\vec{E}| = E_y = A \exp[-p(|x| - t) - i\beta z] \qquad \text{for} \quad |x| \geq t \qquad (1\text{-}68b)$$

where A and B are constants. The only other non-zero field components are H_x and H_z. For a medium in which $(|\sigma|/\omega) \ll \varepsilon^*$, E_y and H_x are related by

$$\frac{E_y}{H_x} = \sqrt{\frac{\mu}{\varepsilon}} \qquad (1\text{-}69)$$

where μ is the magnetic permeability and ε is the real part of the dielectric constant. The boundary condition that E_y be continuous at $x = t$ gives

$$A = B \cos(ht) \qquad (1\text{-}70)$$

Using 1-70 and the additional boundary condition that H_z be continuous at $x = t$, we obtain the following relation between p, h, and t:

$$pt = ht \tan(ht) \qquad (1\text{-}71a)$$

Applying the wave equation $\nabla^2 E_y + k^2 E_y = 0$ (where $k^2 = \omega^2 \mu \varepsilon$) at $x \leq t$ and $x \geq t$, we obtain the additional relation

$$(pt)^2 + (ht)^2 = (K - 1)k^2 t^2 \qquad (1\text{-}71b)$$

The relations in 1-71 provide two equations and four unknowns (p, h,

---

* The quantities σ and ω are the electrical conductivity of the medium and the field frequency, respectively.

t, K). Therefore, the experimental determination of any two unknowns will allow the calculation of the other two. Since K is not directly measurable, the direct measurement of any two of p, h and t is required.

The radiation intensity ($\mathcal{J}$) of an EM field is proportional to the real part of the complex Poynting vector (E × H*), where the (*) denotes complex conjugation. It then follows from 1-69 that the intensity of energy flow per unit time in the z-direction is

$$\mathcal{J} \sim EE^* = E_y E_y^* \qquad\qquad (1\text{-}72a)$$

for the case under consideration. The intensity as a function of the position (x) in the direction perpendicular to the junction plane, is obtained from 1-68 and 1-72a and is given by

$$\mathcal{J}(x) = B^2 \cos^2(hx) \qquad \text{for} \qquad |x| \leq t \qquad (1\text{-}72b)$$

and

$$\mathcal{J}(x) = A^2 \exp[-2p(|x| - t)] \qquad \text{for} \qquad |x| \geq t \qquad (1\text{-}72c)$$

with A and B related by 1-70.

The intensity in 1-72 is that which would be experimentally observed by moving a detector (with input baffle-slits parallel to the plane of the diode junction) perpendicular to the junction (i.e. in the x direction),while the image of the light-emitting end of the diode is focussed on the detector slits. This experiment, illustrated in Figure 1-4b, would determine the intensity profile of the radiating mode(s) of the diode. We may now take the same detector (with slits)

and scan it in the same x direction, but now in the natural radiation field (without the aid of any intermediate optical devices) and at a distance D from the radiating end of the diode. The latter experiment, illustrated in Figure 1-5a, would yield the diffraction (intensity) pattern of the light-emitting mode(s) of the diode. The electric field of the diffraction pattern may be related to the electric field at the radiating source by using Huygen's principle. Since, for our case, $E_y(x)$ is constant in a given plane which is parallel to the junction, we have simply a one-dimensional diffraction problem. Using the notation and construction shown in Figure 1-5b, the diffraction field $E_y(x')$ due to the source field $E_y(x)$ is of the form (23)

$$E_y(x') \sim \int_F \frac{E_y(x)\ e^{-\frac{2\pi i}{\lambda} s(x',x)}}{s(x',x)}\ dx \qquad (1\text{-}73\text{a})$$

In 1-73a it is assumed that the phase of the field $E_y(x)$ is constant over the width (F) of the emitting surface, allowing $E_y(x)$ to be a real quantity. The validity of this assumption is aided by the phase coherence of the light coming from the laser diode cavity.

For the case of far-field (Fraunhofer) diffraction, where $x' >> x$ and $x'x << D^2$, 1-73a becomes

$$E_y(x') \sim \int_F E_y(x)\ e^{2\pi i(\frac{x}{\lambda})(\frac{x'}{D})}\ dx \qquad (1\text{-}73\text{b})$$

The integral in 1-73b is just the Fourier transform integral for E_y
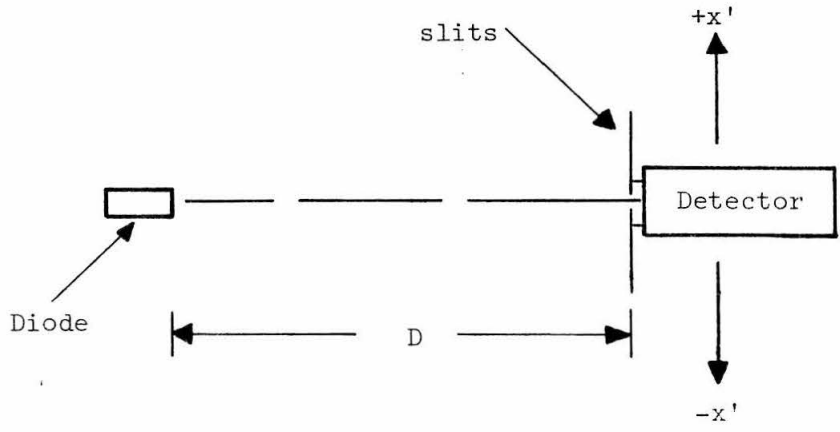
Figure 1-5(a). Far-field Diffraction Intensity Experiment
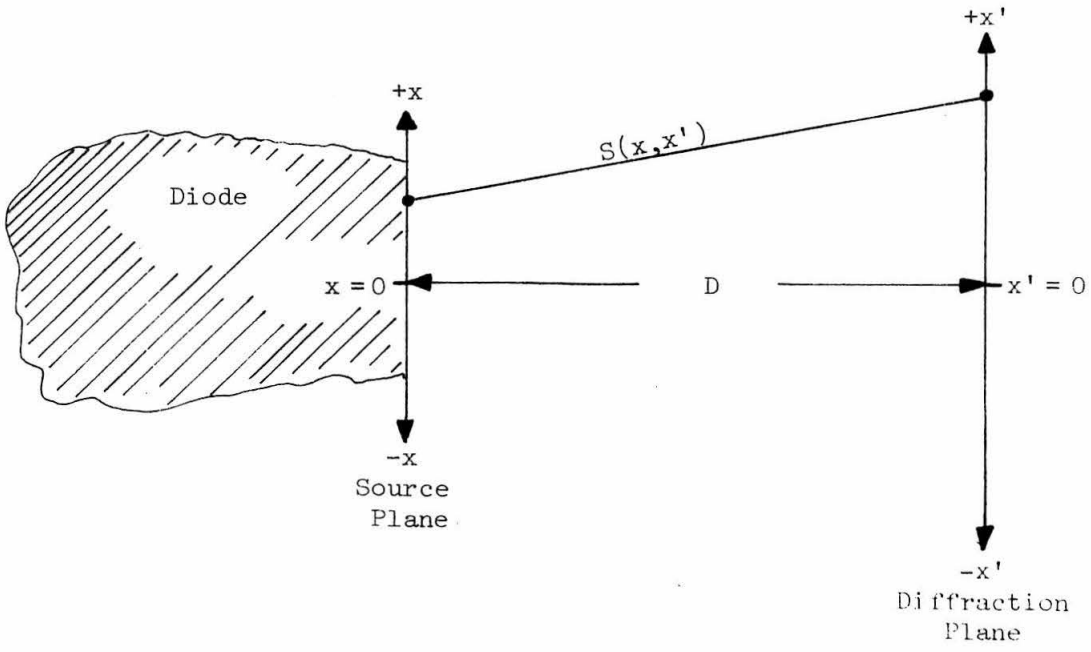

Figure 1-5(b). Geometry for Diffraction Field Calculation

in terms of the variables x and x' . The inversion of 1-73b gives

$$E_y(x) \sim \int_{F'} E_y(x') \; e^{-2\pi i (\frac{x}{\lambda})(\frac{x'}{D})} \; dx' \qquad (1\text{-}73c)$$

(where F' is the width of the far-field pattern), thus completing the relationship between the Fourier transform pair of $E_y(x)$ and $E_y(x')$. Now, the far-field intensity $\mathcal{J}(x')$ follows from 1-72 and is just

$$\mathcal{J}(x') \sim E_y(x') \; E_y(x)^* = E_{yr}^2(x) + E_{yi}^2(x) \qquad (1\text{-}74a)$$

where $E_{yr}(x)$ and $E_{yi}(x)$ are the real and imaginary parts of $E_y(x')$; that is, $E_y(x') = E_{yr}(x') + iE_{yi}(x')$. However, it immediately follows from 1-73b that $E_{yi}(x')$ can be non-zero only if $E_y(x)$ is a nonsymmetric function of x . If we take $E_y(x)$ to be symmetric in x we then obtain $E_y(x')$ as a real quantity (as is $E_y(x)$). We may therefore use the experimentally measured values of $\mathcal{J}(x')$ to determine $E_y(x')$. Using 1-74 we have

$$E_y(x') \sim [\mathcal{J}(x')]^{1/2} \qquad (1\text{-}74b)$$

under the stated condition that $E_y(x)$ be real and symmetric. We may therefore obtain, from the experimental data for $\mathcal{J}(x')$, the intensity profile $\mathcal{J}(x)$ at the radiating surface of the diode, using 1-74b in 1-73c and the relationship $\mathcal{J}(x) \sim E_y^2(x)$.

In order for the above analysis to be self-consistent, the far-field intensity profile $\mathcal{J}(x')$ should be symmetric in x' . This

obtains since a nonsymmetric $\mathcal{J}(x')$ would yield a non-zero imaginary part for $E_y(x)$ in direct contradiction with our basic premise that $E_y(x)$ is real. By calculating the "imaginary part" of $E_y(x)$ from the far-field data and comparing its magnitude with that of the calculated real part, a check can be made on the validity of the analysis. It should be remembered that the use of this method masks the information regarding any asymmetry which might exist in $\mathcal{J}(x)$.

1.3.5 Photon-Assisted Tunneling in Forward Biased Diodes

1.3.5.1 <u>General background.</u> The spontaneous and stimulated emission discussed in the previous sections are due to the "thermionic" injection of minority carriers across the forward biased diode junction. However, for low enough temperatures and forward bias voltages, the injection of minority carriers across the voltage barrier may be less than the injection due to tunneling through the barrier. The tunneling process may be aided by the radiative recombination of the tunneling electrons and holes. This mechanism of photon-assisted tunneling has been discussed in detail by Leite et al (24) in conjunction with experiments using GaAs p-n junctions. The effect is the result of the connection of exponentially decaying electron wave functions via a radiative transition matrix element. The matrix elements involved are similar to those discussed in Section 1.2, with the exception that the "crystal" momentum $(\vec{k})$ need no longer be conserved in order for the matrix elements to be nonzero. There are two possible tunneling models for radiative recombination (24), namely those of (a) "diagonal" tunneling and (b) impurity-band tunneling.

1.3.5.2 The "diagonal" tunneling model.   The diagonal tunneling model, illustrated in Figure 1-6a, is based on the simultaneous tunneling by an electron (from the n-side) and a hole (from the p-side) into the junction region, where they recombine via the emission of a photon. The net result is the diagonal transition of an electron from the n-side to a hole state on the p-side.   The diagonal tunneling is therefore a source of current flow as well as a source of radiation. At the point in the junction where the integrand of the matrix element for the radiative transition of an electron to a hole state is a maximum, the probability for radiative recombination is also at a maximum.   For the completely symmetric case of equal electron and hole effective masses and equal impurity doping, the point of maximum transition probability will occur exactly at the middle of the junction.   If we take the total radiated light intensity ($\mathcal{J}$) to be proportional to the radiative transition probability at midjunction, the dependence of $\mathcal{J}$ on the applied voltage (V) for an abrupt junction is (18)

$$\mathcal{J} \sim e^{S_T V} \tag{1-75a}$$

with

$$S_T \equiv (q/2)^{3/2} \alpha \, W_1 \tag{1-75b}$$

and

$$\alpha \equiv \frac{\pi m_T^{1/2}}{2q\hbar} \tag{1-75c}$$

For 1-75, W_1 is given by 1-53b and m_T is the reduced (effective) tunneling mass for electrons and holes. In addition, the slope S_T
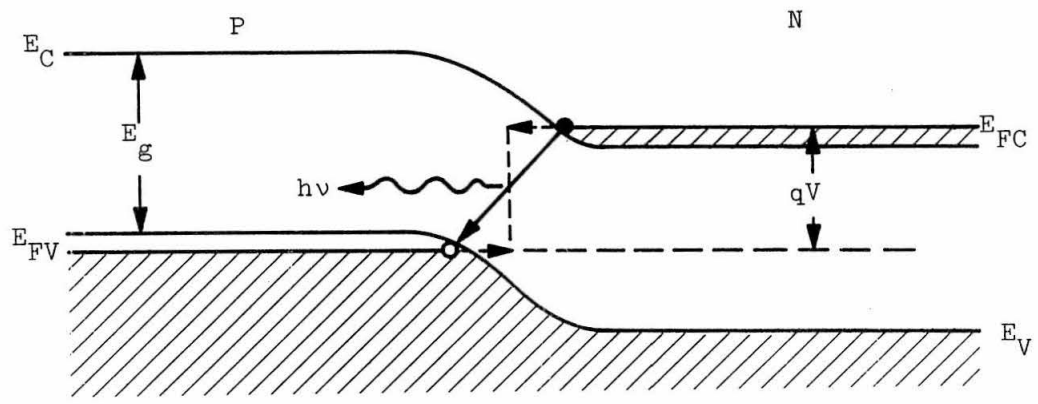
Figure 1-6(a). The "Diagonal" Tunneling Model

$$E = \frac{h^2}{2}\left[\frac{k_t^2}{m_t} + \frac{k_\ell^2}{m_\ell}\right]$$
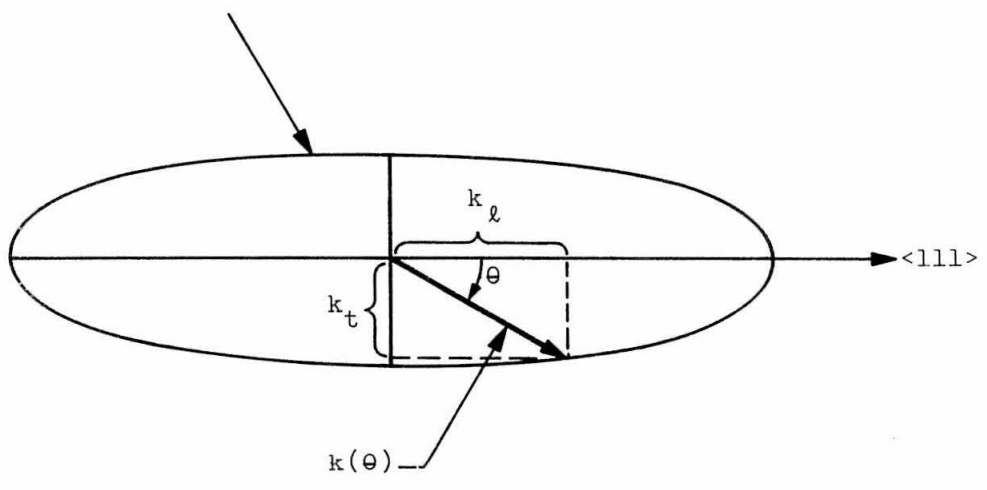

Figure 1-6(b). Constant-Energy Ellipse for PbTe

should be independent of temperature.

The quantity W_1 may be obtained from the experimental measurement of the (differential) junction capacitance per unit area (C) as a function of the applied (DC) voltage. The quantity needed for the determination of W_1 is the slope (S_c) of the plot of $1/C^2$ vs. V . We have, from 1-54, the following expression for W_1 in terms of S_c

$$S_c \equiv \frac{d}{dV} (1/C^2) = - \frac{W_1^2}{\epsilon^2} \qquad (1\text{-}76a)$$

or

$$W_1 = \epsilon[|S_c|]^{1/2} \qquad (1\text{-}76b)$$

Following (18), the inverse tunneling mass ($1/m_T$) is obtained from the reciprocal addition of the effective electron and hole tunneling masses (m_T^e and m_T^h) , written as

$$\frac{1}{m_T} = \frac{1}{m_T^e} + \frac{1}{m_T^h} \qquad (1\text{-}77)$$

Recalling our discussion on band structure in Section 1.1.2, the constant energy surfaces for PbTe are ellipsoids of revolution, with the major axes oriented along the <111> directions. The diodes used for the experiments to be discussed here possess diffused junctions which are intended to be parallel to the (100) cleavage planes of the material. We can therefore determine the ideal effective tunneling masses by calculating the magnitude of the momentum vector ($\vec{k}$) in the <100> direction. For a constant-energy (E) ellipsoid, we may write

$$E = \frac{\hbar^2 k^2(\theta)}{2m(\theta)} \qquad (1\text{-}78)$$

where $k(\theta)$ is the magnitude of the vector $\vec{k}(\theta)$, which makes an angle θ with the major axis of the ellipsoid (as illustrated in Figure 1-6b), and where $m(\theta)$ is the corresponding effective mass. For an ellipsoid of revolution, we need only consider a cross sectional plane containing the major axis, where the major axis represents the longitudinal direction of heavy mass (see Table 1-1). Following this construction, we can express 1-78 as

$$E = \frac{\hbar^2}{2}\left[\frac{k_t^2}{m_t} + \frac{k_\ell^2}{m_\ell}\right] \qquad (1\text{-}79a)$$

where m_t and m_ℓ are the transverse and longitudinal effective masses. However, by geometry we have

$$k_t = k(\theta) \sin \theta \qquad (1\text{-}79b)$$

$$k_\ell = k(\theta) \cos \theta$$

and 1-79a becomes

$$E = \frac{\hbar^2 k^2(\theta)}{2}\left[\frac{\sin^2\theta}{m_t} + \frac{\cos^2\theta}{m_\ell}\right] \qquad (1\text{-}79c)$$

Using 1-78 and 1-79c, we obtain

$$\frac{1}{m(\theta)} = \frac{\sin^2\theta}{m_t} + \frac{\cos^2\theta}{m_\ell} \qquad (1\text{-}80)$$

with $m(\theta)$ now being the tunneling mass in the θ direction. Now, for

the exact case of tunneling in the <100> direction $(\cos \theta = 1/\sqrt{3}$, $\sin \theta = \sqrt{2/3})$, the effective mass value obtained from 1-80 is, in the limit of $m_{\ell} \gg m_t$, just $(3/2 \, m_t)$. However, from 1-75 and Table 1-1 we see that tunneling along the direction of transverse mass is greatly favored by virtue of its very small magnitude (as compared with the longitudinal mass). Therefore, any irregularities or "waviness" in the diffused junction, which would give rise to local orientations other than in a (100) plane, would also allow for tunneling to occur in the preferred direction of low effective mass. Such preferred tunneling would tend to dominate all other directions of current flow, and hence the tunneling current would exhibit the characteristics of the small transverse mass. This is very likely to be the case in diffused junctions, where it is expected that diffusion irregularities do produce a microscopically multidirectional junction. Therefore, the most probable (reduced) tunneling mass for holes and electrons in PbTe may be obtained from the values for transverse mass, given in Table 1-1, by using 1-77. The result for (m_T/m_o) is 0.11, where m_o is the free electron mass.

1.3.5.3 The impurity-band tunneling model. With the presence of impurity (energy) states lying in the band gap, electrons and holes may tunnel from the n and p sides, respectively, into the impurity states, as illustrated in Figure 1-7. Radiative recombination of an electron and hole may then occur, with the resultant emission of a photon. As indicated in Figure 1-7, an increase in applied voltage provides for the filling of higher energy impurity states. If the

P   N

donor impurity
"band-tail"

$h\nu$

qV

acceptor impurity
"band-tail"
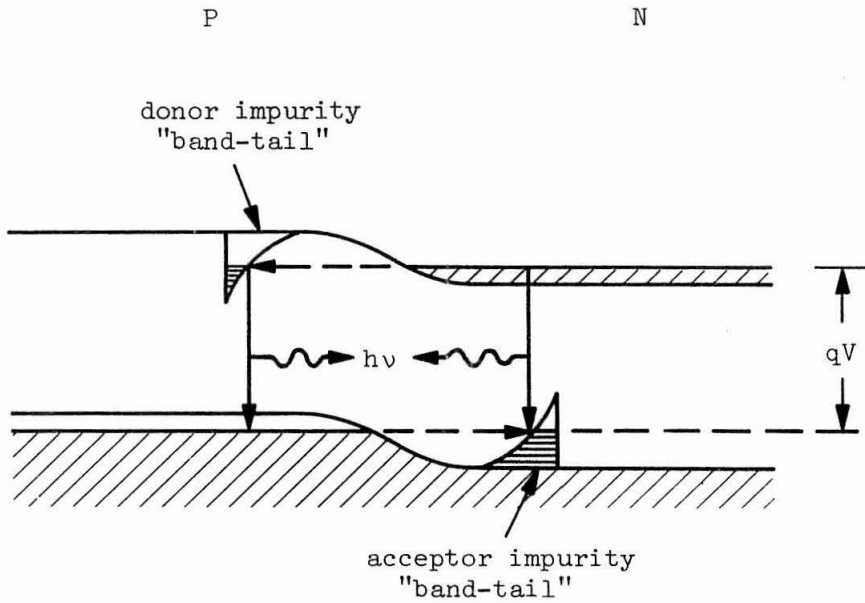
Note: The impurity "band-tail" density-of-states is
        indicated on the horizontal axis.

Figure 1-7.   The Impurity Band Tunneling Model

current flow through the impurity states is limited by the finite
recombination rate, then the impurity states will be filled, up to an
energy which is proportional to the applied voltage. Therefore, both
the $\mathcal{J}$-V and I-V characteristics will exhibit the energy dependence
of the impurity density of states, and should also be temperature
independent. The doping impurity states in extrinsic semiconductors
lie near the band edges, where minority carrier impurity states may be
left vacant due to compensation in the material. These states may
therefore be filled via (photon-assisted) tunneling. Recalling our dis-
cussion in Section 1.1.3, the compound PbTe forms n and p materials
by having excess stoichiometric proportions of Pb and Te respectively.
Therefore, one would expect a large amount of compensation to occur,
leaving a fairly large number of minority carrier impurity states
vacant. However, we also pointed out that the large (static) dielec-
tric constant of PbTe ($400 \ \varepsilon_0$) meant that the impurity "band-tails"
could penetrate the band gap by only a small amount. Therefore, donor-
acceptor band-filling via tunneling into band-tails is not likely to
occur in PbTe, since the thermionic emission given by 1-55 would pre-
dominate for such small barrier voltages.

II. DESCRIPTION OF THE EXPERIMENT

2.1 General Remarks

The experiment consisted basically of (a) the preparation of
PbTe p-n junction diodes and (b) the measurement of the electrical
characteristics (i.e. the current-voltage behavior) and (c) the mea-
surement of the radiation characteristics of the diodes. Concomitant
with the specific task of diode fabrication was the application of
ohmic electrical contacts to the diodes. The p-n junctions were
obtained using a closed-tube vapor-phase diffusion of bulk PbTe mate-
rial. Owing to the small size of the diode specimens, a great deal of
their preparation had to be done with the aid of a microscope and with
the use of special tools and techniques. The measurement of electrical
and radiation characteristics of the diodes called for a variety of
apparatus. Included were infrared (photoconductive) detectors, cryo-
genic dewars and specialized electronic equipment.

The purpose of this chapter is the description of the tasks and
equipment involved in the total experiment.   The following sections
describe the details of the experiment which are briefly introduced in
the above paragraph.

2.2 Investigation of Metal-Semiconductor Contacts with PbTe

In order for a p-n junction diode to exhibit its true current-
voltage (I-V) characteristics, the impedance of the electrical contacts
to the diode must be small compared to that of the junction. For our
case, the initial criterion for the contacts was that they be ohmic in

nature, i.e. that the contacts do not by themselves exhibit rectifica-
tion properties with I-V characteristics of the type given by 1-55.
The origin of rectification in metal-semiconductor contacts may be
stated briefly as follows. In bringing a metal and a semiconductor
into contact, a redistribution of charge takes place in order to satisfy
Poisson's equation, resulting in the formation of a potential barrier
between the two materials. The height of the potential barrier may
result from (a) the presence of surface states whose energies lie
within the energy gap of the semiconductor, or (b) the relative differ-
ence between the work-functions of the electrons in the metal and
electrons in the semiconductor.

Let us consider a simple example where the contact properties
are determined by (b) alone, and where the metal work-function $(\emptyset_m)$ is
greater than the n-type semiconductor work-function $(\emptyset_s)$. Figure 2-1
(a) shows the electron energy levels before contact, with the donor
Fermi level (E_{DF}) of the extrinsic n-type semiconductor lying near the
conduction band (E_C). When contact is made, electrons flow from the
semiconductor into the metal, providing a bound-charge dipole layer.
This sets up a potential barrier $(\emptyset_m - \emptyset_s)$ which will display a nonlinear
I-V behavior (see Figure 2-1(b)). A basic law of thermodynamics
requires that the Fermi level (chemical potential), designated E_F, be
constant for the two systems in contact (in thermal equilibrium).
However, for the case of $\emptyset_s > \emptyset_m$, a non-rectifying barrier is built
up at the contact, as shown in Figure 2-1(c). In this case electrons
flow from the metal into the semiconductor upon contact, causing a

(a) METAL-SEMICONDUCTOR BEFORE CONTACT

$\boxed{\phi_m > \phi_s}$

(b) RECTIFICATION-BARRIER CONTACT
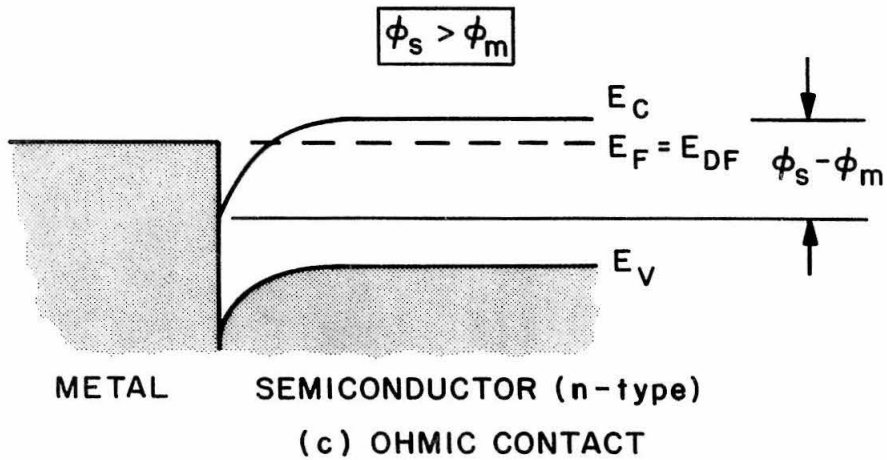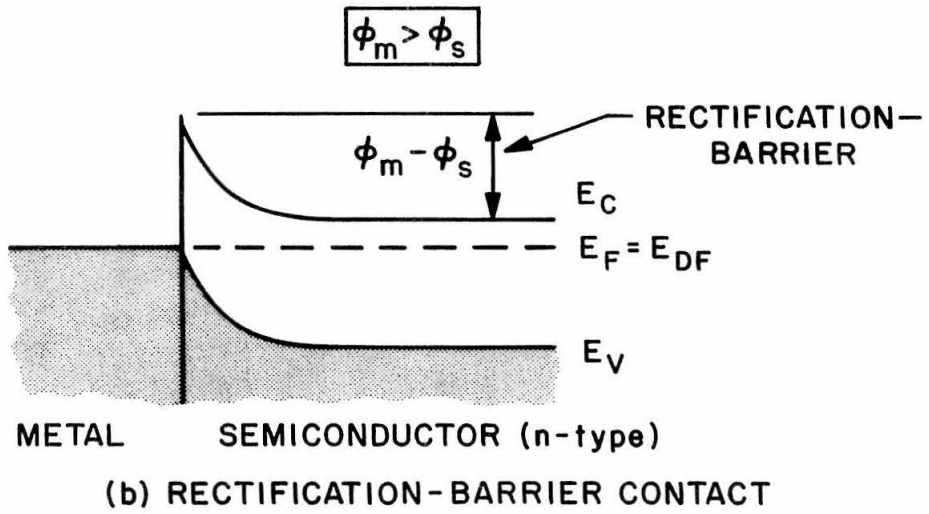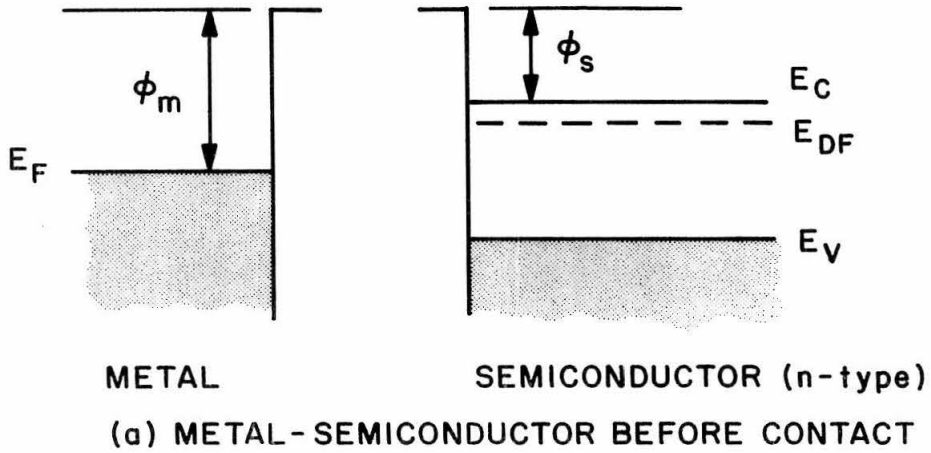
$\boxed{\phi_s > \phi_m}$

(c) OHMIC CONTACT

Figure 2-1

depression in the potential at the contact surface. Hence an ohmic contact between the metal and the semiconductor is achieved. In an analogous manner, cases of both rectifying and ohmic contacts between a metal and a p-type semiconductor may be constructed. It should be noted that in actual cases the rectifying barrier height is not usually just $(\emptyset_m - \emptyset_s)$ as shown in Figure 2-1(b). Indeed, some experimental data indicate that the barrier height may be almost independent of $\emptyset_m$, in which case the barrier height is determined by semiconductor surface states (25).

In looking for metals which will provide ohmic contacts with a semiconducting material, those which act as donors are needed for the n-type material and those which act as acceptors are needed for the p-type material. In general, Se, Te Ag, Au and Tl have been found to behave as acceptors and Pb, In, Sn and Bi as donors in PbTe (26). This provided the basic direction in seeking proper soldering alloys for PbTe contacts. Other criteria for selection were relative convenience in use (oxidizing characteristics, melting point, etc.) and availability (either commercially or made in the laboratory). For the investigation of the I-V behavior of different alloys with PbTe, experimental samples were made by using the alloys to solder copper wire contacts to single crystals of PbTe. The quantitative investigation of such contacts involves several questions regarding (a) the directions of forward and reverse biasing, (b) the geometry and symmetry of the contacts, and (c) the temperature dependence of the I-V characteristics. However, the main concern here was not the detailed investigation of the contacts, but a qualitative determination of

whether or not a given metal-semiconductor combination exhibited ohmic properties. Hence, the results presented here will be very qualitative and will center mainly on those cases which exhibit no rectification properties.

The metal-semiconductor pairs investigated are listed in Table 2-1. Out of the total of five combinations studied, four displayed rectification characteristics and two ohmic behavior. All six candidates were measured at three temperatures: (a) room temperature (300°K), (b) liquid nitrogen (77°K) and (c) liquid hydrogen (20°K). All six exhibited ohmic conduction at room temperature. All those which showed nonlinear I-V characteristics did so at both 77°K and 20°K. In general, the voltage at a given current was higher at 20°K than at 77°K, as shown in Figure 2-2(a). An exception to this was noted in the case of sample MS-1 in the third quadrant (Figure 2-2(b)). These figures illustrate the general asymmetry of the I-V curves. The two successful candidates were MS-5 and MS-6, with their data shown in Figure 2-3. Both samples clearly exhibit ohmic conduction by their linear I-V curves. The fact that the resistance exhibited by MS-5 and MS-6 decreased with decreasing temperature lends further credence to their ohmic behavior.
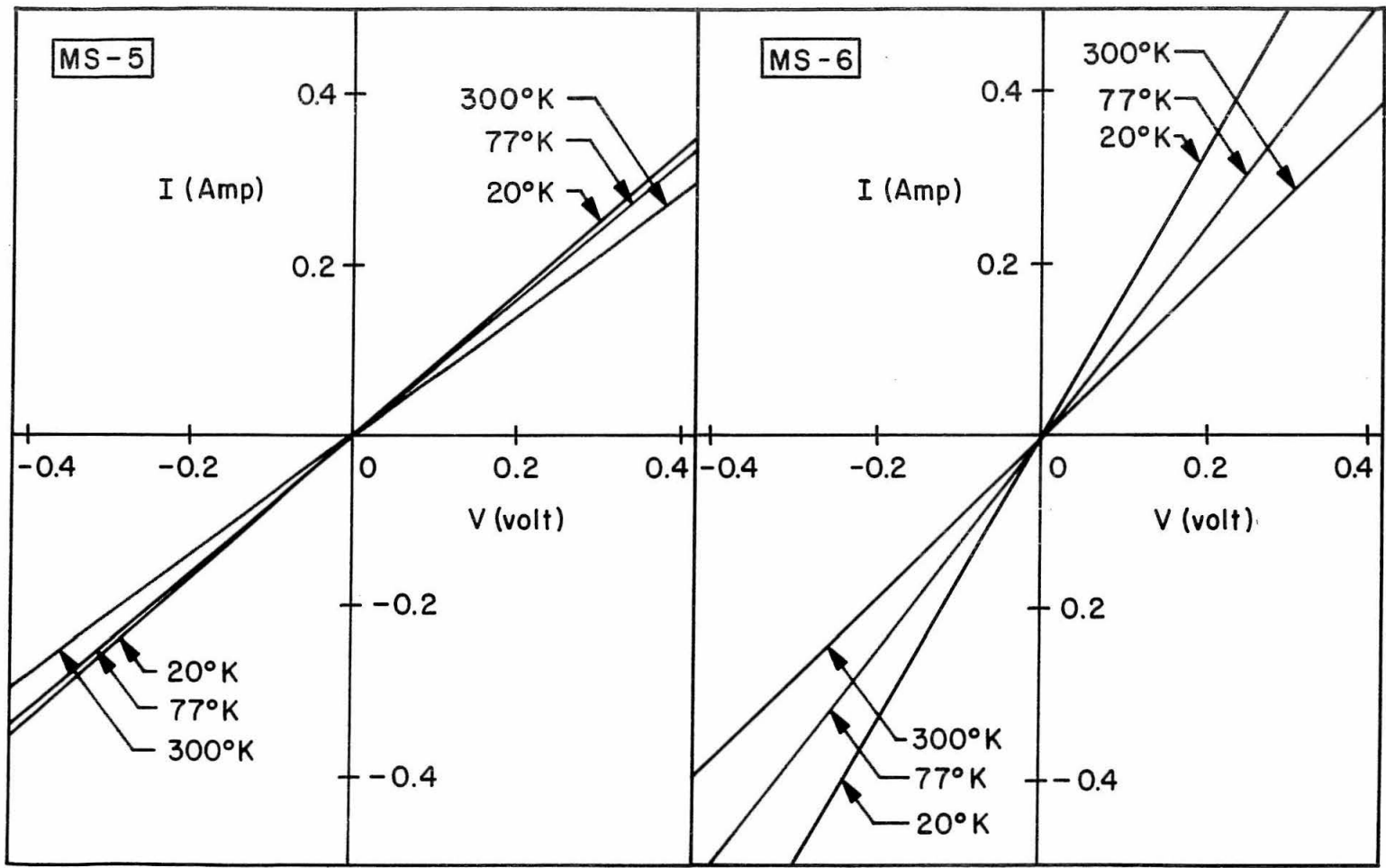
The results of the above investigation were (a) the eutectic Au-Tl alloy, with a melting point of 131°C (27) provided an ohmic contact with p-type PbTe and (b) the non-eutectic metallic solution of weight composition 25% In, 37.5% Sn, 37.5% Pb, with a melting point of 138°C (28), provided an ohmic contact with n-type PbTe.
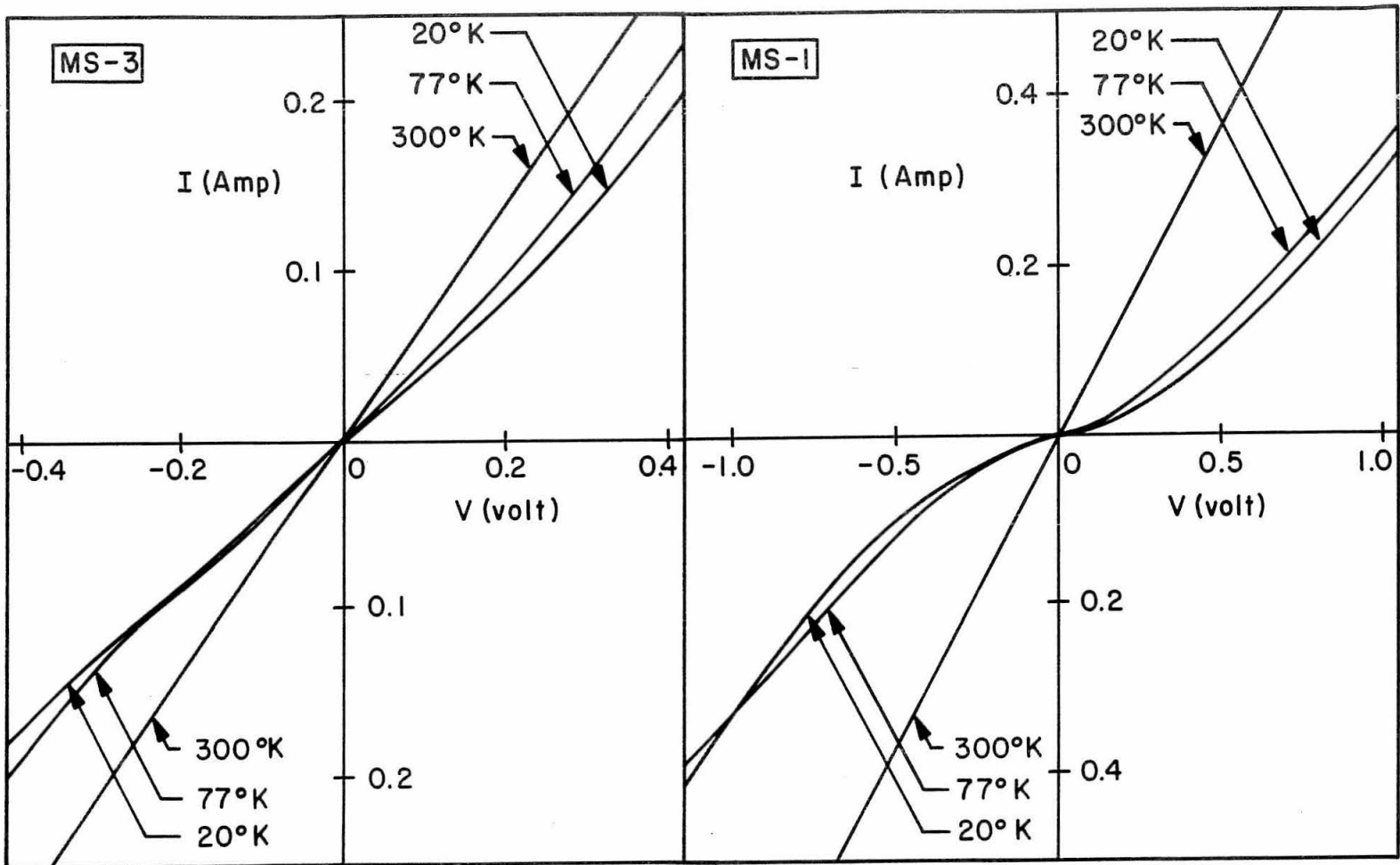
(a) MS-3 I-V CURVES   (b) MS-I I-V CURVES

Figure 2-2

(a) MS-5 I-V CURVES   (b) MS-6 I-V CURVES

Figure 2-3

Table 2-1

Sample	PbTe Impurity Type	Alloy	Contact
MS-1	p (polished)	In-Tl-Hg	non-ohmic
MS-2	p (cleaved)	In-Tl-Hg	non-ohmic
MS-3	p	In-Sn	non-ohmic
MS-4	p	Sn	non-ohmic
MS-5	n	In-Sn-Pb	ohmic
MS-6	p	Au-Tl	ohmic

2.3   Preparation of the Lead Telluride P-N Junction Diodes

2.3.1   General Remarks

The preparation of PbTe p-n junction diodes required several independent processes which were carried out in sequential order. These processes are described in the following paragraphs and in the same order in which they were performed.

2.3.2   Preparation of the Bulk Material

The bulk material used for the diodes was single crystal p-type PbTe grown by a modified Bridgeman method (29). Experiments with photo-induced radiation from PbTe single crystal p-type material have shown that a higher radiative efficiency is obtained from crystals which have been annealed in a hydrogen atmosphere (9). Therefore the crystals used for this experiment were annealed in a hydrogen atmosphere at a pressure of 10^{-1} torr. The final concentration of p-type carriers in the material was on the order of $10^{17} \, cm^{-3}$ (30). The annealed crystals were hand-polished in the (100) plane to a thickness

of approximately 3/4 mm, using a 0.3 micron alpha-alumina abrasive
material mixed with distilled water. The hand-polished crystals were
then electrolytically polished in a special solution consisting of 10
grams sodium hydroxide, 100 cc distilled water, and 50 cc glycerol.
The PbTe crystals were held in the electrolytic solution for 10-20
minutes using a special pair of stainless steel pincers. The PbTe
acted as the anode, with a large area stainless steel plate acting as
the cathode. The electrode potential was controlled at 10 volts dur-
ing the process. The above procedures resulted in polished single
crystals with dimensions of about 2 mm by 2 mm in the (100) plane and
a 3/4 mm thickness.

2.3.3 Diffusion of the Bulk Material to Form P-N Junctions

The diffusion of an n-type layer onto the p-type bulk material
required the use of a Pb-rich two-phase ingot of Pb and Te, chemically
combined in a sealed quartz tube. The quartz tube was washed with
48% hydrofluoric acid, rinsed in distilled water, drained dry and
vacuum pumped down to 10^{-6} torr. During vacuum pumping the tube was
flamed with a hydrogen torch. Quantities of 99.999% pure powdered Pb
and Te were weighed out in relative proportions of 51 and 49 atomic
percent respectively, with a total weight of about 10 grams. The
materials were loaded into the quartz tube which was again vacuum
pumped and sealed off at a pressure of less than 10^{-6} torr. The sealed
tube was heated with a torch flame long enough for a partial reaction
of the contents to take place. It was then heated at 950°C for three
hours and quenched in water. The resulting ingot was used for the dif-
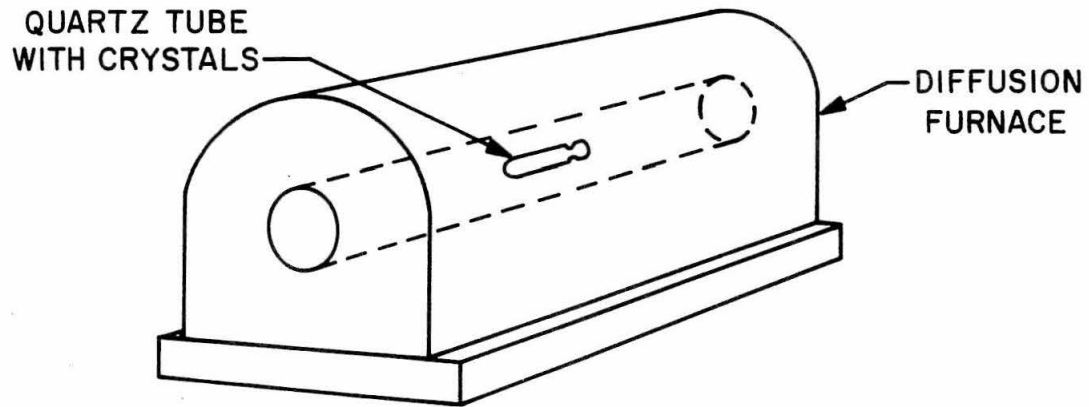fusion of the p-type PbTe crystals.

The diffusion of the PbTe took place in a quartz tube 5 inches long and with an outer diameter of 2.5 cm. This tube was cleaned and prepared in the same manner as the tube in which the diffusion ingot was made. Just prior to the placement of the ingot and p-type PbTe crystals in the diffusion tube, both were washed in 5% nitric acid and rinsed with distilled water. The ingot and crystals were then placed in the quartz tube and the tube vacuum pumped down to 10^{-6} torr. During the vacuum pumping the tube was gently heated with a hydrogen-oxygen torch flame. The tube was then sealed off with the torch and checked for leaks with a Tesla-coil. The sealed tube diffusion configuration is shown in Figure 2-4(a).

The sealed tube was placed in the center of a diffusion furnace which had been pre-heated to 650°C and stabilized at that temperature for 24 hours (see Figure 2-4(b)). The vapor diffusion of the PbTe single crystals by the Pb-rich ingot took place for one hour at a controlled temperature of $650 \pm 10^{\circ}$C. At the end of the hour, the quartz tube was removed from the furnace and quenched in water.

The single crystals of PbTe had thus been brought to thermal equilibrium, through the vapor phase, with the two-phase ingot of Pb and Te. During the one hour at 650°C, the Pb-rich material had diffused to a certain depth into the Te-rich, p-type material, forming an n-type layer completely surrounding the single crystals. The equilibrium conditions were "frozen in" by quenching the crystals at room temperature, thereby forming a permanent p-n junction at a given depth.
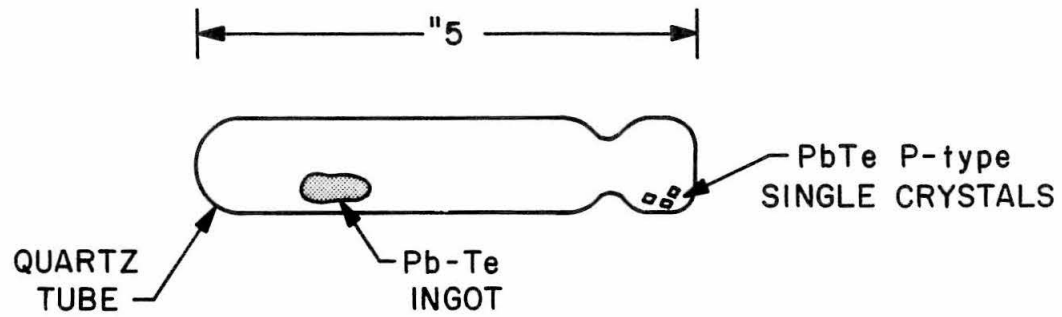
(a) PbTe DIFFUSION CONFIGURATION

(b) PbTe CRYSTALS IN DIFFUSION FURNACE

Figure 2-4

After quenching, the tube was broken open and the crystals were checked, using a thermoelectric probe (hot-point probe), to verify the presence of an n-type layer.

2.3.4 The Formation of Diodes from the Diffused Material

In order to form diodes from the diffused material, it was necessary to remove the diffused n-layer from all but a single surface in a (100) plane. In forming the planar diodes it was important not to damage the junctions by mechanical abrasion, etc. For this reason no mechanical polishing or lapping was used to form the sides of the diodes perpendicular to the junction plane.

As a first step in removing the n-layer the side opposite to the (100) junction-plane was mechanically lapped to a thickness of 0.5 mm, leaving the lapped surface sufficiently far away from the junction so as not to damage it. For the purpose of lapping the back surface, the crystals were mounted (junction face down) on a glass slide with a hand-setting, low melting point, red wax* as illustrated in Figure 2-5(a). The exposed surface was then hand-lapped (using a 0.3 micron alpha-alumina abrasive material mixed with distilled water) on a fine cloth surface. The removal of the n-layer from the crystals was verified with the use of the hot-point probe. During the removal of the n-layer, the material type and thickness were carefully checked after small amounts of repeated lapping. In this manner, the depth of the diffused layer was found to be 75 ± 10 microns. The lapped crystals were removed from the glass slide by melting the wax

*Bankers Special Wax
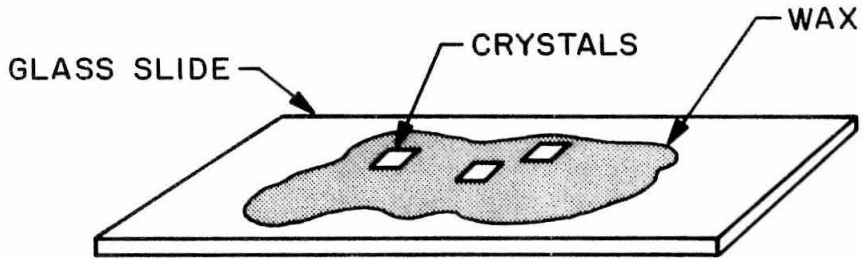
(a) LAPPING CONFIGURATION OF PbTe CRYSTALS
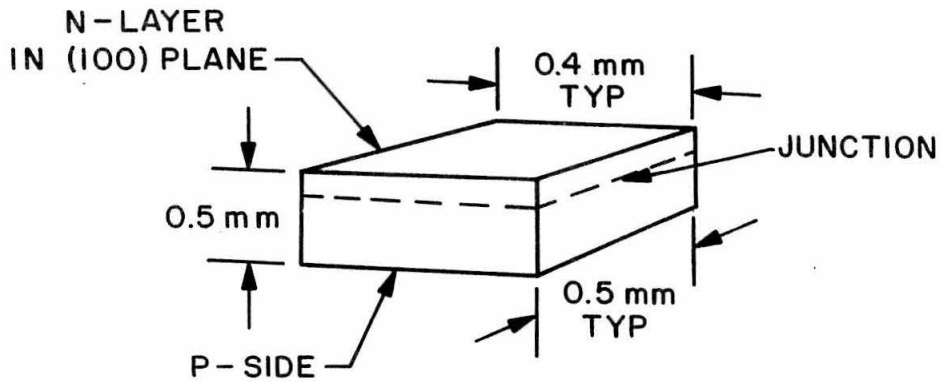
(b) CLEAVED PbTe DIODE

Figure 2-5

followed by cleaning with cotton dipped in alcohol.

With the crystals positioned lapped-side down on a glass slide and viewed under a microscope, the edges were cleaved perpendicular to the (100) junction plane, using a finely sharpened razor blade and tapping it gently with the point of a file. In a similar manner, the actual diodes were cleaved from the n-layer area to specific dimensions (usually about 0.5 mm by 0.4 mm). The diodes thus formed were rectangular in shape, as shown in Figure 2-5(b).

2.3.5 The Formation of Electrical Contacts to the Diodes

In order to obtain ohmic contacts to both the p and n sides of the diodes, the special soldering materials discussed in Section 2.2 were used. For convenience in handling and in the attachment of electrical leads, standard type TO-5 gold-plated transistor headers were used as diode mounts. Before soldering the p-type diode base to the surface of a header, the header surface was covered with a layer of Au-Tl eutectic alloy (melting point of $131^{o}C$) using a special solder flux* and a 25-watt, copper-tipped soldering iron. The gold plating on the headers allowed for a good flow of Au-Tl solder over the surface, thereby forming a good metal to metal contact between the solder and header surface. Using the same solder flux and soldering iron as before, the diode base was soldered to a header while the diode was held in place using a pair of fine pointed tweezers. This was done with the aid of a microscope. Thus a good semiconductor to metal ohmic contact was achieved between the p-side


*This flux is Superior No. 30 Super-Safe Soft Solder Flux

of the diode and the surface of the header. After this the diode and header was rinsed with alcohol to remove the solder flux residue.

For the formation of the contact to the n-layer, the special In-Sn-Pb alloy (melting point 138°C) was used as the soldering material. In order to prevent the short-circuiting of the junction during soldering, care was taken to prevent solder from flowing over the sides. Prior to the actual soldering to the diodes, small In-Sn-Pb solder "dots" were formed (under microscopic observation) from small pieces cut from wire stock. The small pieces were placed on a glass slide and covered with the special solder flux. The dots were then melted by radiative heating from a small custom soldering tool fashioned from 5 mil diameter nichrome wire and a 1/2 watt incandescent bulb socket. The nichrome wire was bent into a tip which was heated to a bright orange by passing a variac controlled current through it. The melted solder was immediately transformed into small spheres about 0.1 mm in diameter, providing good, shiny, solder pre-forms. After cooling, the spheres of solder were rinsed with alcohol to remove the flux residue. With the aid of a microscope, an In-Sn-Pb sphere was then placed in the center of the n-layer of the diode and barely moistened with solder flux. The nichrome wire soldering fixture was then used to melt the sphere by radiative heating, thereby causing the solder to bond itself to the n-side of the diode (see Figure 2-6(a)). Thus a good semiconductor to metal ohmic contact was achieved on the n-side of each diode.

In order to complete the electrical connection to the header, a 2 mil diameter gold wire was soldered to the n-layer solder dot of the
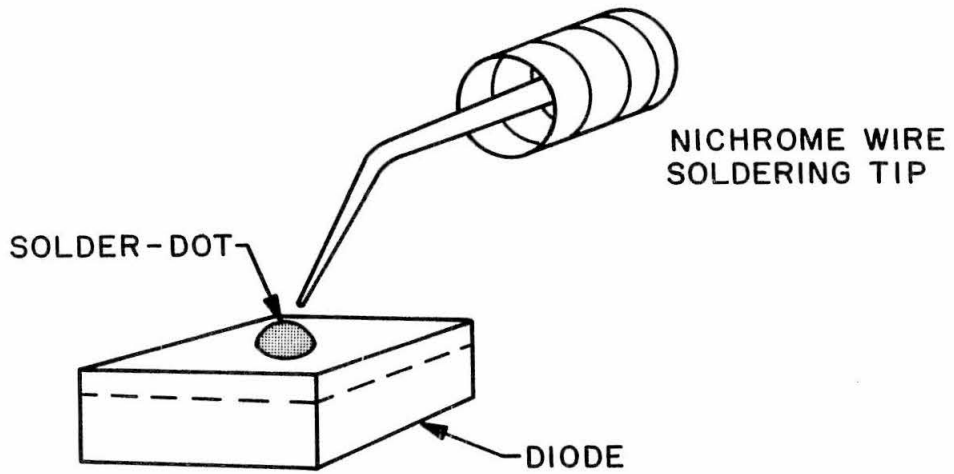
(a) SOLDER-DOT ON N-LAYER
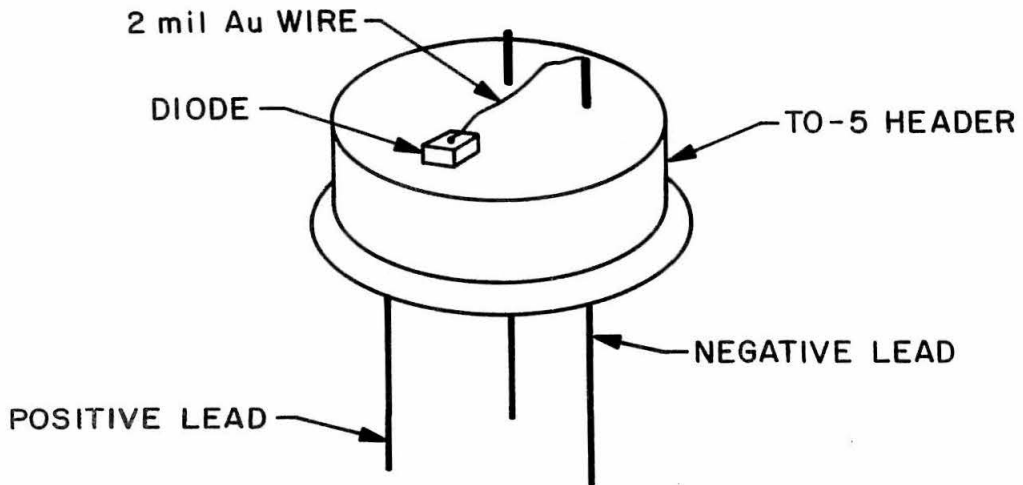
(b) ELECTRICAL CONNECTION OF DIODE TO HEADER

Figure 2-6

diode using the nichrome wire tool (the gold wire tended to alloy with the In-Sn-Pb). The free end of the wire was then soldered to one of the gold-plated contact pins, thereby completing the electrical connection of the diode to the header (see Figure 2-6(b)). These tasks were performed with the aid of a microscope.

2.4 Experimental Apparatus and Data Acquisition Schemes

2.4.1 General Remarks

This section describes the salient features of the apparatus and data acquisition systems used to obtain the experimental data. Of particular interest are the mercury-doped germanium photodectors, which are explained briefly in what follows. Since a considerable variety of data were obtained, the particular data-taking schemes will be explained primarily with block diagrams.

2.4.2 Photoconductive Detectors

The infrared radiation emitted by the PbTe diodes required the use of photodetectors which are sensitive to wavelengths greater than 6μ . This automatically eliminates the use of conventional phototubes, whose photo-response is limited to wavelengths less than about 2μ . It is also required that the detector be able to respond to pulses as short as 2 microseconds, which eliminates conventional infrared detectors (e.g. thermopiles). However, a family of doped-germanium photoconductive detectors have, within the last few years, reached the state of development where their reliable use is possible. These detectors utilize the presence of shallow impurity levels (usually acceptors, or p-type) which may be "ionized" with low energy photons. The impurity carriers are "frozen out" by cryogenic cooling, thus enabling the modulation of the material's electrical conductivity via photon excitation. These detectors also possess the necessary fast response, with their basic response time being the carrier

recombination lifetime ($\tau < 1$ microsecond)[*].

The basic scheme for light detection with a photoconductive detector is shown in Figure 2-7a. Following the notation of Figure 2-7a the ratio of the photo-induced change in voltage (ΔV) to the applied (DC) voltage (V_o) is given by

$$\frac{\Delta V}{V_o} = \frac{R_L \, \Delta R}{(R_L + R_D)^2} \cdot \left[1 - \frac{\Delta R}{(R_L + R_D)}\right]^{-1} \qquad (2\text{-}1a)$$

where R_D is the unilluminated resistance of the detector. The quantity R is the resistance modulation due to photo-excitation, given by

$$\frac{\Delta R}{R_D} = \frac{\Delta p}{p_o} \cdot \left[1 + \frac{\Delta p}{p_o}\right]^{-1} \qquad (2\text{-}1b)$$

where p_o is the unilluminated carrier (hole) population. The quantity Δp is the change in the hole population due to photon absorption and is given by

$$\Delta p = \eta_D G \, \Phi \, \tau \qquad (2\text{-}1c)$$

where G is the geometrical photon-loss factor[**], τ is the carrier recombination lifetime, Φ is the total number of photons emitted per second and η_D is the detector (external) quantum efficiency

---

[*]In practice, the response time is limited by the collective RC time-constant of the detector and its associated electronics.

[**]The geometrical loss factor (G) is just the solid angle subtended by the light emitting surface at the detector, divided by 2π .
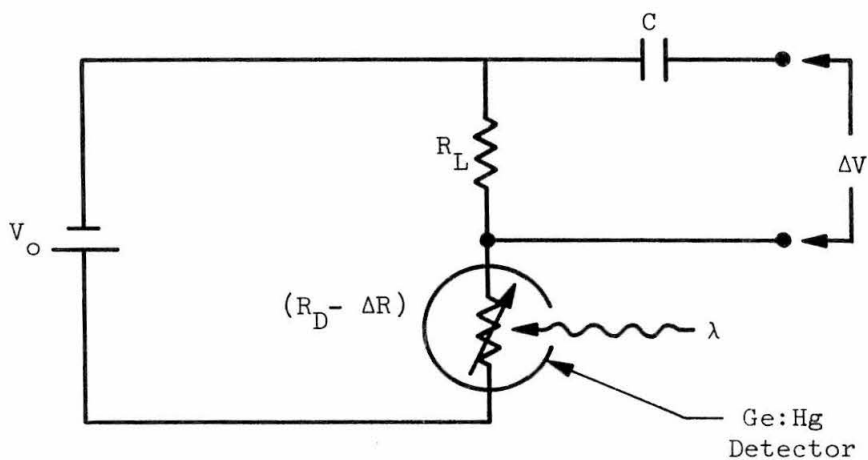
Figure 2-7(a).   Ge:Hg Detector and Circuit

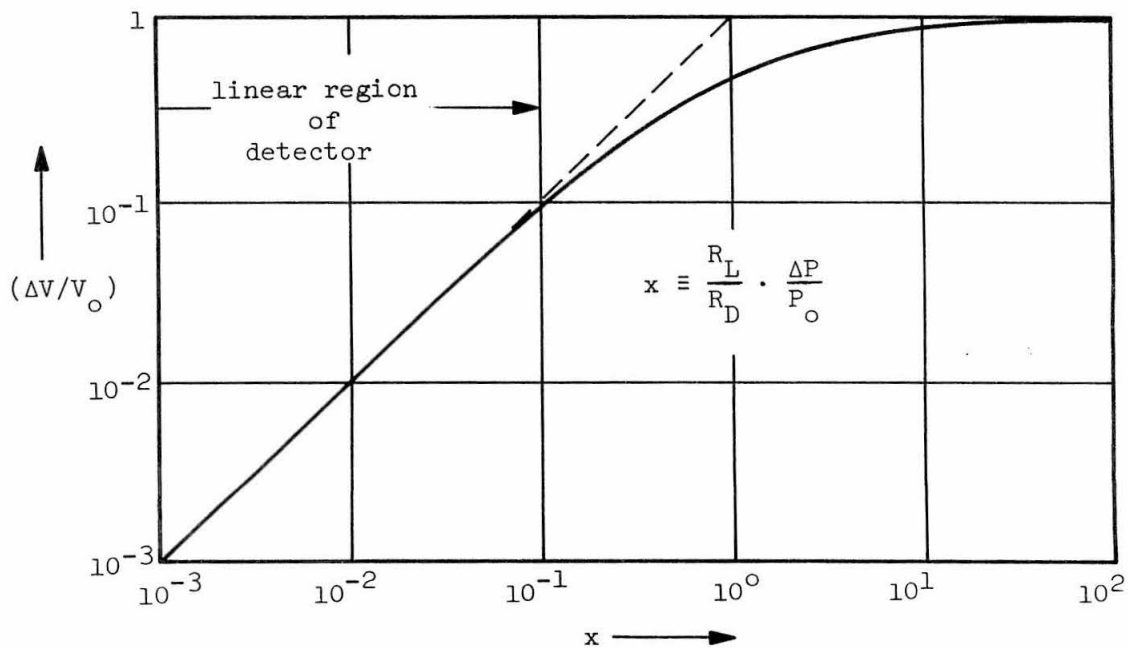$$x \equiv \frac{R_L}{R_D} \cdot \frac{\Delta P}{P_o}$$

Figure 2-7(b).   Detector Linearity

(i.e. the number of holes produced per photon intercepted by the detector)[*]. Now, for $R_L \ll R_D$ the expression 2-1a becomes

$$y \equiv \frac{\Delta V}{V_o} = \frac{x}{1+x} \tag{2-2a}$$

where

$$x \equiv \frac{R_L}{R_D} \cdot \frac{\Delta p}{p_o} \tag{2-2b}$$

The function 2-2a, plotted in Figure 2-7b, determines the region of linear response of the detector, i.e. the region where $\Delta V \sim \Phi$. As seen from Figure 2-7b, the detector remains linear up to signal voltages (ΔV) of magnitude 0.1 V_o[**]. In addition, for $R_L \ll R_D$ we may write

$$\Delta V = \eta_D G R_L (q\tau/\tau_t) \Phi \tag{2-3a}$$

where

$$\tau_t \equiv \ell^2/\mu_p V_o \tag{2-3b}$$

is the mobile charge transit time, ℓ is the distance between the contacts on the detector and μ_p is the carrier (hole) mobility of the

---

[*] The "external" quantum efficiency (η_D) of the detector includes photon losses due to (a) reflection at the surface of the detector, and (b) incomplete absorption of the photons by the detector material. The "internal" quantum efficiency of the detector (i.e. the number of holes produced per photon absorbed by the detector) is essentially 100% (43).

[**] This is a very convenient method of testing for detector linearity, i.e. by merely monitoring $\Delta V/V_o$.

detector material. We may therefore express the external quantum efficiency of a light-emitting diode (i.e. the number of photons emitted per charge carrier flowing through the junction) as

$$\eta_d = \frac{\Delta V}{\eta_D GIR_L} \ (\tau_t/\tau) \qquad (2-4)$$

where I is the total current flowing through the diode.

The detectors used for this experiment were constructed from single crystals of mercury-doped germanium (Ge:Hg).[*] The mercury atoms form an acceptor level located about 0.09 electron-volts above the valence band edge. The useful temperature range for Ge:Hg detectors is below 40°K.

2.4.3 Data Acquisition Schemes

2.4.3.1 $\mathcal{I}$ vs. I data. The experimental set-up used to obtain the total radiation intensity ($\mathcal{I}$) as a function of diode current (I) is illustrated in Figure 2-8. The diode is mounted adjacent to the Ge:Hg detector and both are submerged in a cryogenic liquid. Since the Ge:Hg is sensitive only below 40°K, data were obtained using liquid hydrogen (20.4°K) and liquid helium (4.2°K. The diode current was in the form of short (2 to 50 microsecond) pulses, in order to prevent joule heating of the diodes.

2.4.3.2 I vs. V data. The experimental scheme used to obtain the current-voltage (I-V) characteristics of the PbTe diodes is illustrated in Figure 2-9a. As indicated in the diagram, (10 microsecond)

---

[*] The concentration of mercury atoms is about 5×10^{15} cm^{-3}.
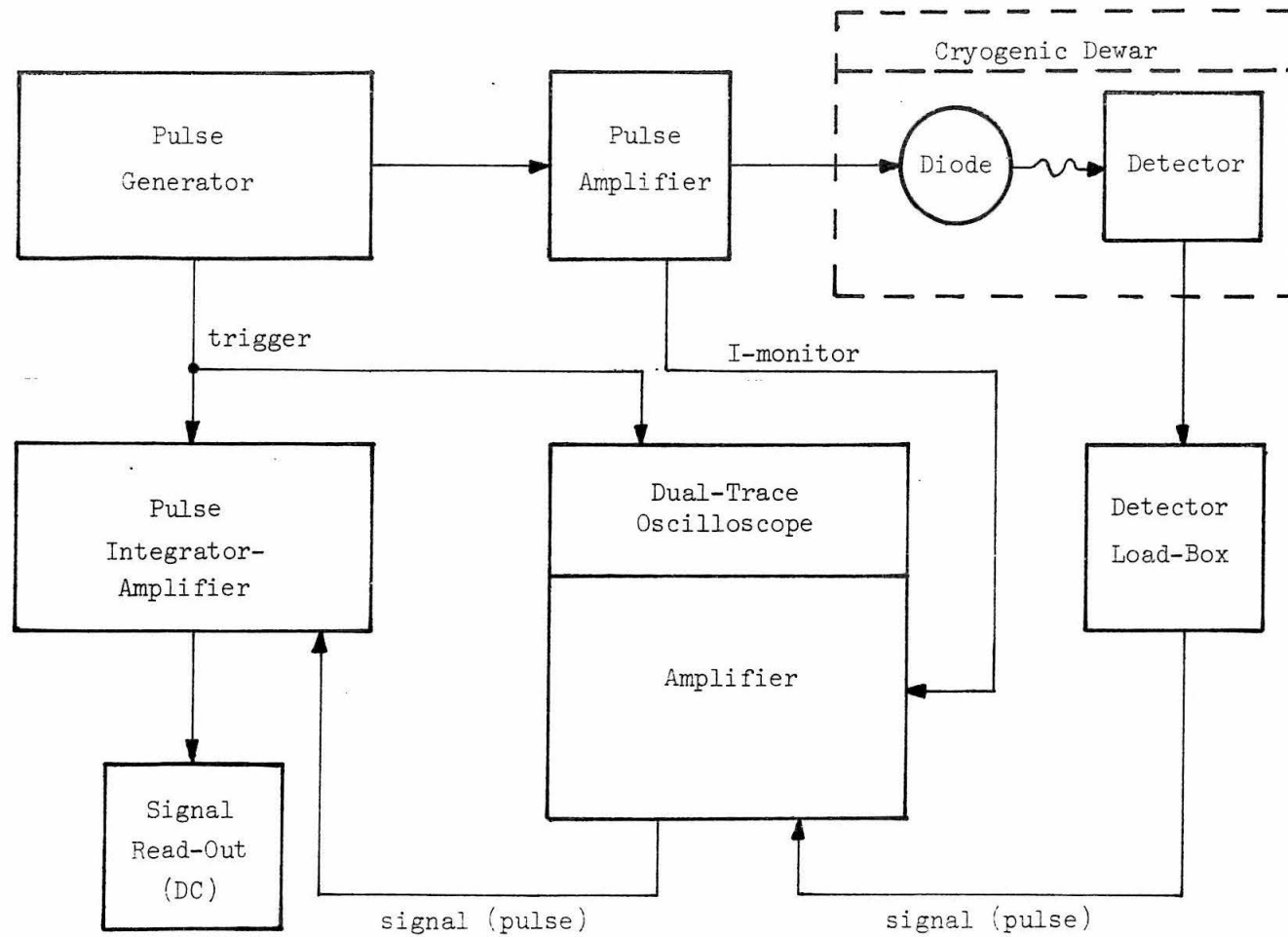
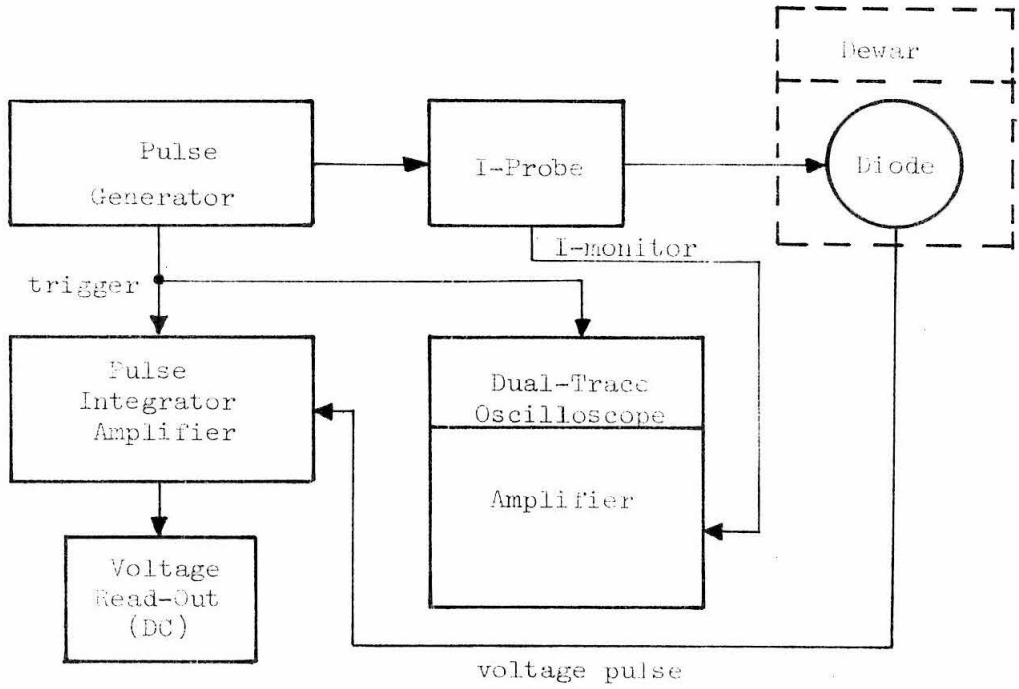Figure 2-8. $\mathscr{J}$-I Data Acquisition Scheme

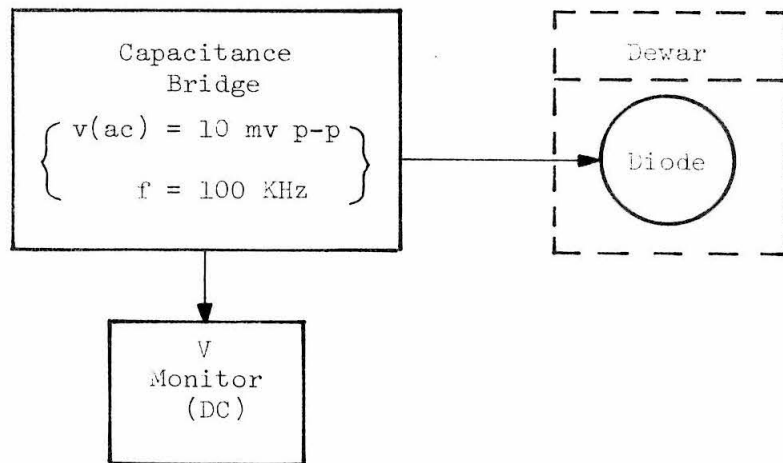Figure 2-9(a). I-V Data Acquisition Scheme

Figure 2-9(b). C-V Data Acquisition Scheme

current pulses were used for these measurements. The use of short
current pulses prevented the heating up of the diodes at high current
levels, just as for the $\mathcal{L}$ - I data. The I-V data were obtained with
diodes submerged in liquid nitrogen (77°K), liquid hydrogen (20.4°K)
and liquid helium (4.2°K) .

2.4.3.3 C vs. V data. The experimental arrangement used to
obtain the differential capacitance (C) as a function of applied (DC)
voltage (V) is illustrated in Figure 2-9b. The C-V data were obtained
at 77°K and 4.2°K .

2.4.3.4 Spectral intensity data. The spectral intensity
$\mathcal{L}(\lambda)$, of the stimulated emission from PbTe diodes was measured with
the system outlined in Figure 2-10. Stimulated emission spectra were
obtained from diodes in contact with a cryogenic bath of liquid hydro-
gen (20.4°K). The diodes were attached to a special "cold-finger"
which was mounted on a cryogenic dewar. As before, the diode current
consisted of short (2-5 microsecond) pulses to prevent heating. Special
lenses made from arsenic-trisulphide (As_2S_3) were used because of their
required infrared transmission characteristics. The monochromator
shown in the illustration contains a diffraction grating[*], which was
used in the first order. The Ge:Hg detector was cooled to 20.4°K with
liquid hydrogen. Optical alignment of the data system and the diodes
was accomplished with the use of a He-Ne gas laser ($\lambda = 6328$Å) .

2.4.3.5 Image-scan and far-field intensity data. The total
intensity of PbTe-diode stimulated emission was measured in both the

---

[*] The diffraction grating is "blazed" for $\lambda = 6\mu$ (in first order).

Figure 2-10(a). $\mathscr{L}(\lambda)$ Data Acquisition Scheme (optics)
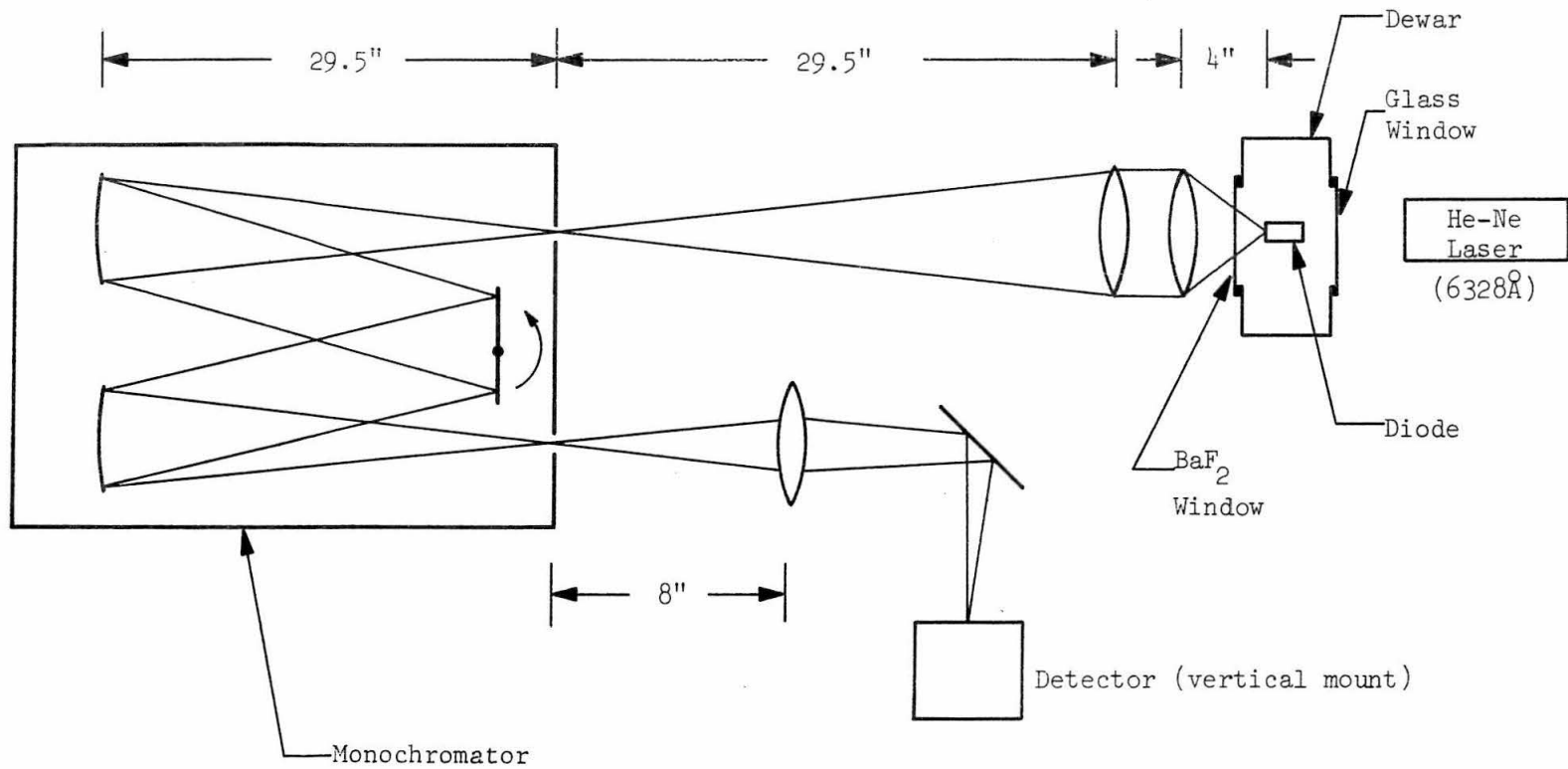
NOTE: Lenses are made of As_2S_3

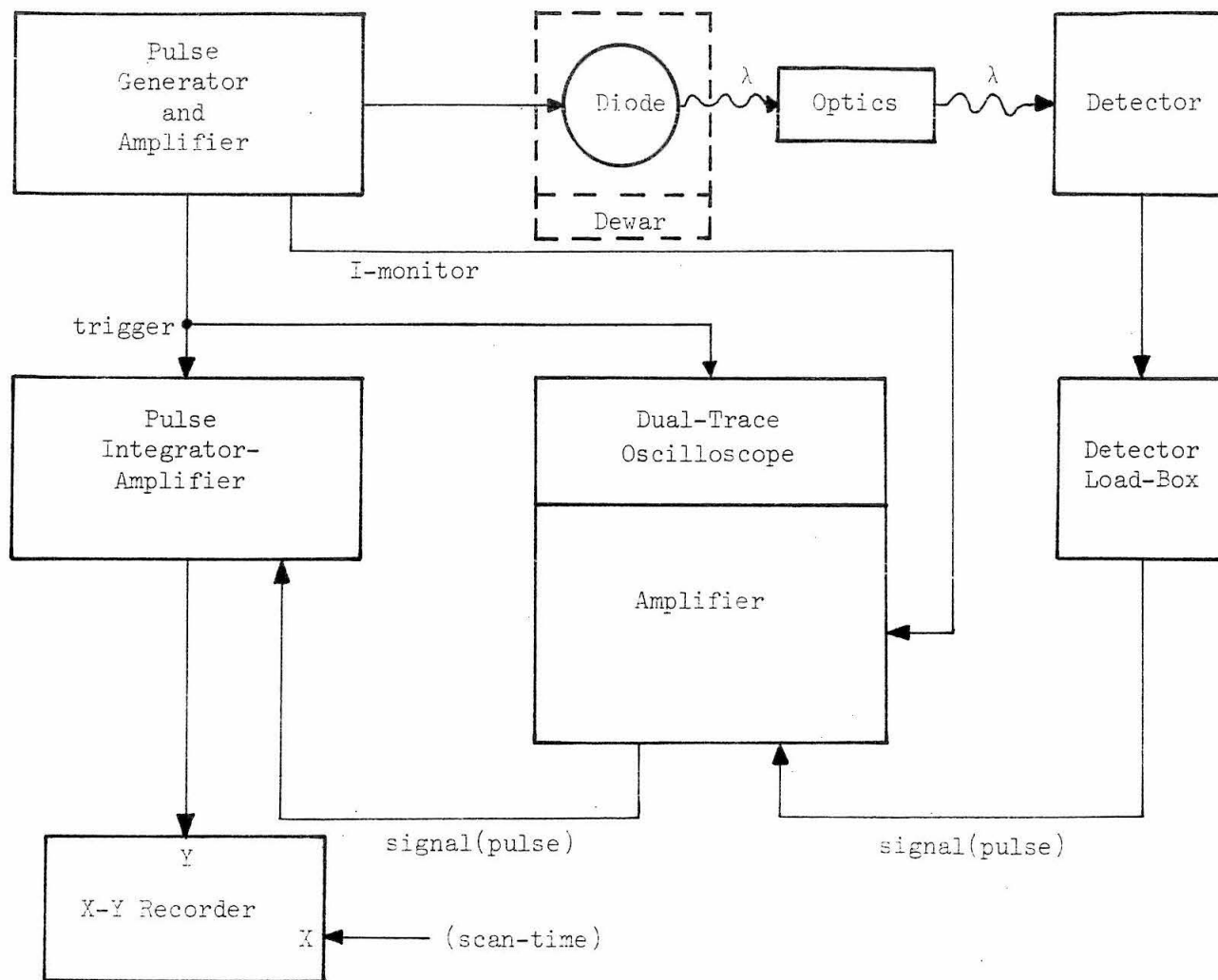Figure 2-10(b). $\mathcal{J}(\lambda)$ Data Acquisition Scheme (electronics)

image plane, $\mathcal{J}(x)$, and in the far-field plane, $\mathcal{L}(x')$. The experimental arrangements for the measurement of $\mathcal{J}(x)$ and $\mathcal{L}(x')$ are illustrated in Figures 1-4b and 1-5a, respectively. The data were taken with a liquid hydrogen "cold-finger" (20.4°K), with current pulses and detector-signal amplification as indicated previously.*

---

*The detector used for these measurements is a cooled (77°K), lead selenide photoconductive cell. This particular detector was used (in spite of its reduced sensitivity and frequency response) because of its horizontal operating position. The detector was cooled to 77°K with a special (Joule-Thompson) compressed N_2 cooler.

III. PRESENTATION OF EXPERIMENTAL RESULTS

3.1 General Remarks

The purpose of this chapter is to present the various data obtained during the course of the experiment. Each type of data is explained and illustrated in a separate section, along with a brief discussion of the particular data obtained. A comparative discussion and analysis of all the data is given in Chapter IV.

3.2 Total Light Intensity vs. Diode Current

The total radiated light intensity $(\mathcal{J})$ from the PbTe diodes was measured as a function of diode current (I) . These measurements were taken over a current range of three orders of magnitude, with a corresponding intensity range of six orders of magnitude. Figure 3-1 illustrates the $\mathcal{J}$-I data taken on diode J-2, at a temperature of $20.4^\circ K$. The data can be broken up into the following four distinct regions (in order of increasing current): (a) region A, where $\mathcal{J} \sim I^m$, $m \geqq 1$, with m approaching 1 as I increases; (b) region B, where $\mathcal{J} \sim I^2$; (c) region C, where $\mathcal{J}$ increases very rapidly with I , and (d) region D, where $\mathcal{J}$ is again linear with I . For reasons which will become evident as we progress, the four regions are characterized by the following types of current injection and recombination radiation:

(a) region A: photon-assisted tunneling,

(b) region B: spontaneous emission from "thermionic" injection,

(c) region C: threshold region for stimulated emission, and

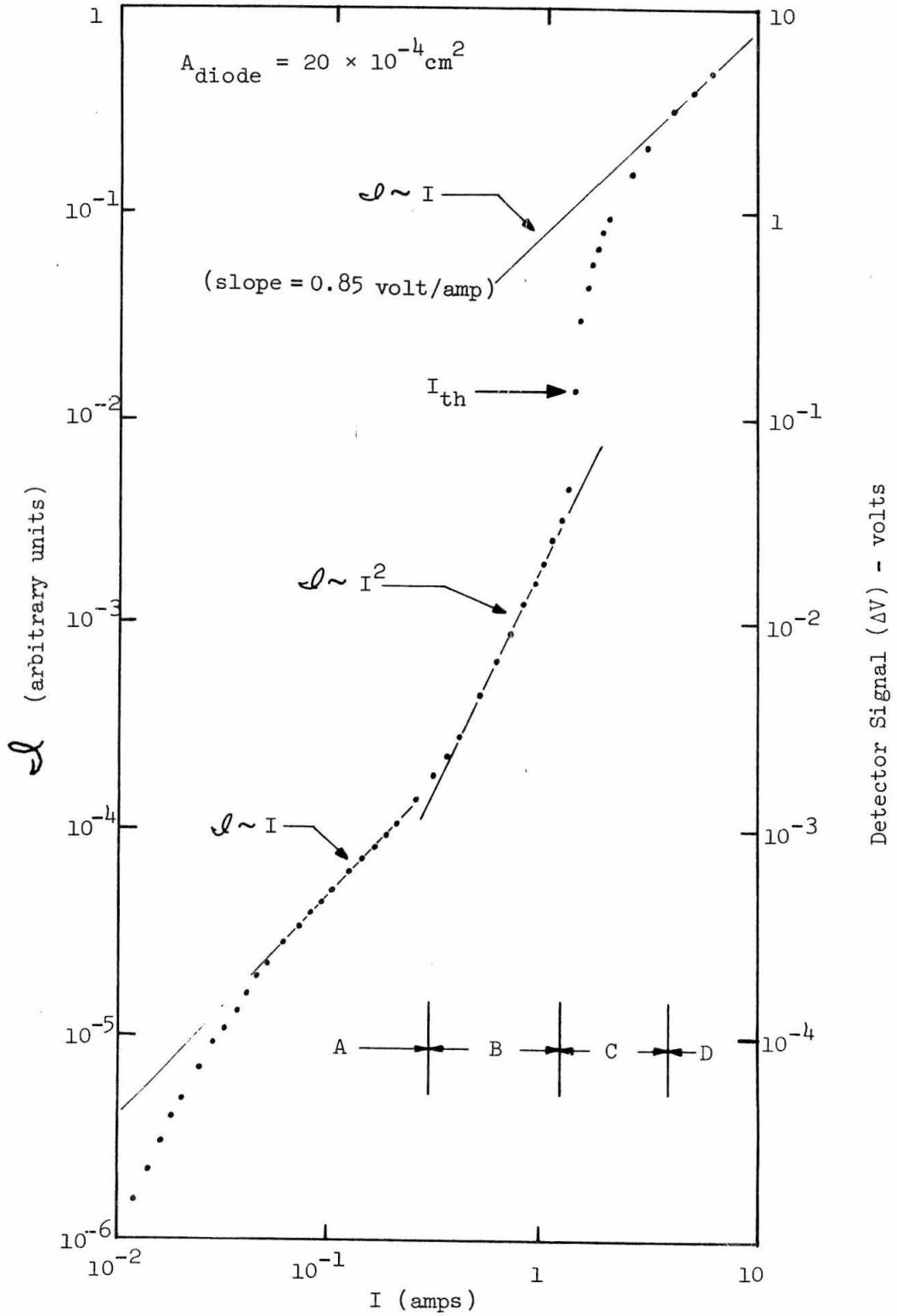(d) region D: "saturation" region for stimulated emission.

$A_{diode} = 20 \times 10^{-4} cm^2$

$\mathcal{I} \sim I$

(slope $= 0.85$ volt/amp)

I_{th}

$\mathcal{I} \sim I^2$

$\mathcal{I} \sim I$

$\mathcal{I}$ (arbitrary units)

Detector Signal (ΔV) - volts

A — B — C — D

I (amps)

Figure 3-1. $\mathcal{I}$ - I Data for Diode J-2 (20.4°K)

Figure 3-2, which shows an oscilloscope display of the detector output pulse and the corresponding diode current pulse, illustrates the sharp increase in intensity with increased current at the threshold for stimulated emission (region C). Figure 3-3 illustrates data taken on diode J-22, in region C and for temperatures of 20.4°K and 4.2°K. Figure 3-3 indicates a temperature dependence of the threshold current for stimulated emission. Figure 3-4 shows data obtained from diode J-23 in region A, at 20.4°K and 4.2°K. In Figure 3-4 it is of particular interest that the linear dependence of J on I in region A is independent of temperature (at least between 20.4°K and 4.2°K). These data are discussed further in Chapter IV.

3.3 Diode Current vs. Voltage

The "raw" current-voltage (I-V) data obtained from diode J-23 are shown in Figure 3-5, for diode temperatures of 77°K, 20.4°K and 4.2°K. The "S" shaped curves clearly illustrate a middle region of exponential dependence of current on voltage. The apparent "increase" in diode current at low voltages is a direct manifestation of the existence of electrical shunt-paths around the junction of the diode. The presence of junction-shunts was verified by observing the effect of the chemical etching* of the diodes on the magnitude of the shunt-current. By properly etching the diodes, the amount of shunting of the junction by foreign material was minimized. The amount of etching which could be done was, or course, limited by the amount of damage done to the electrical contacts by the etchant. The apparent "decrease"
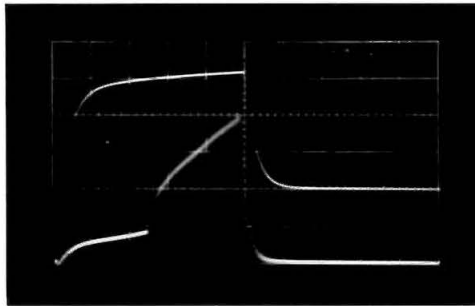
---

*The etching solution used was 5-20% (by volume) nitric acid.

A. Upper Trace

    vertical scale: current (0.5 amp/cm)

    horizontal scale: time (1 μsec/cm)

B. Lower Trace

    vertical scale: detector (0.05 volt/cm)

    horizontal scale: time (1 μsec/cm)

Figure 3-2. Current and Light-Detector Pulses
for Diode J-2 at I_{th} (20.4°K)

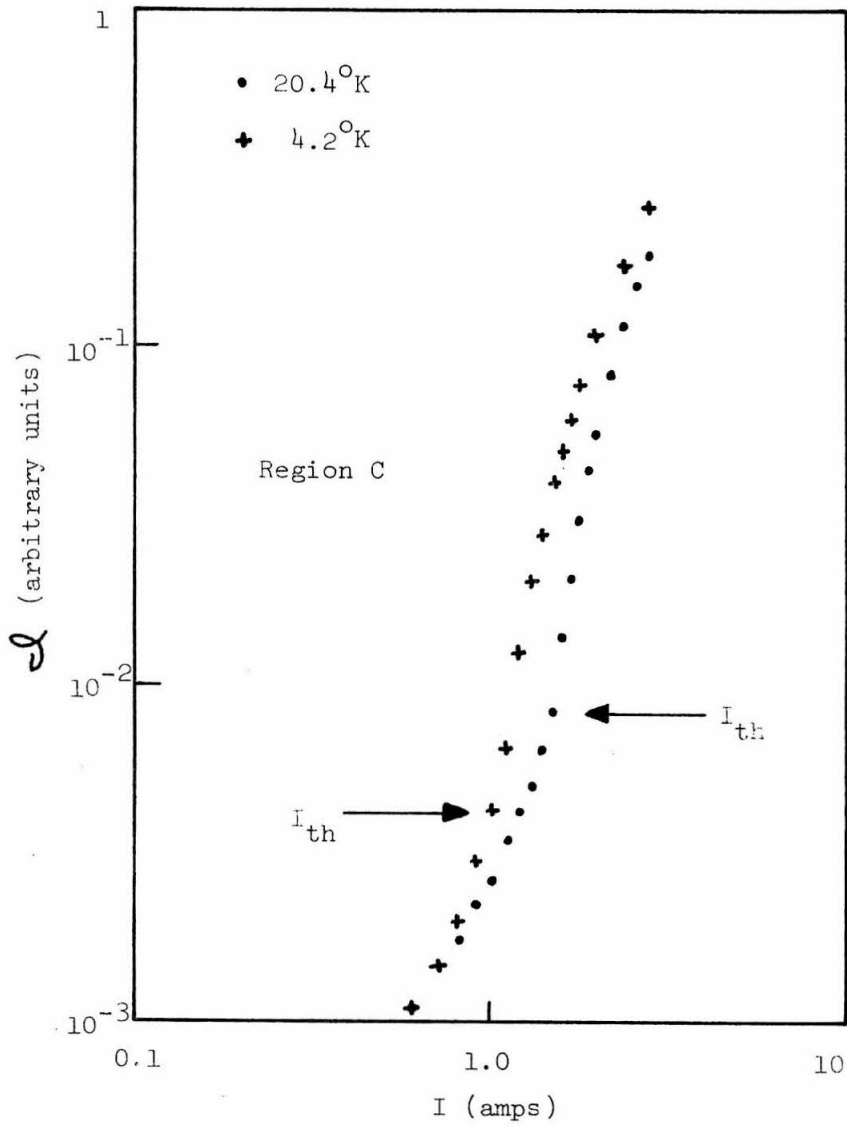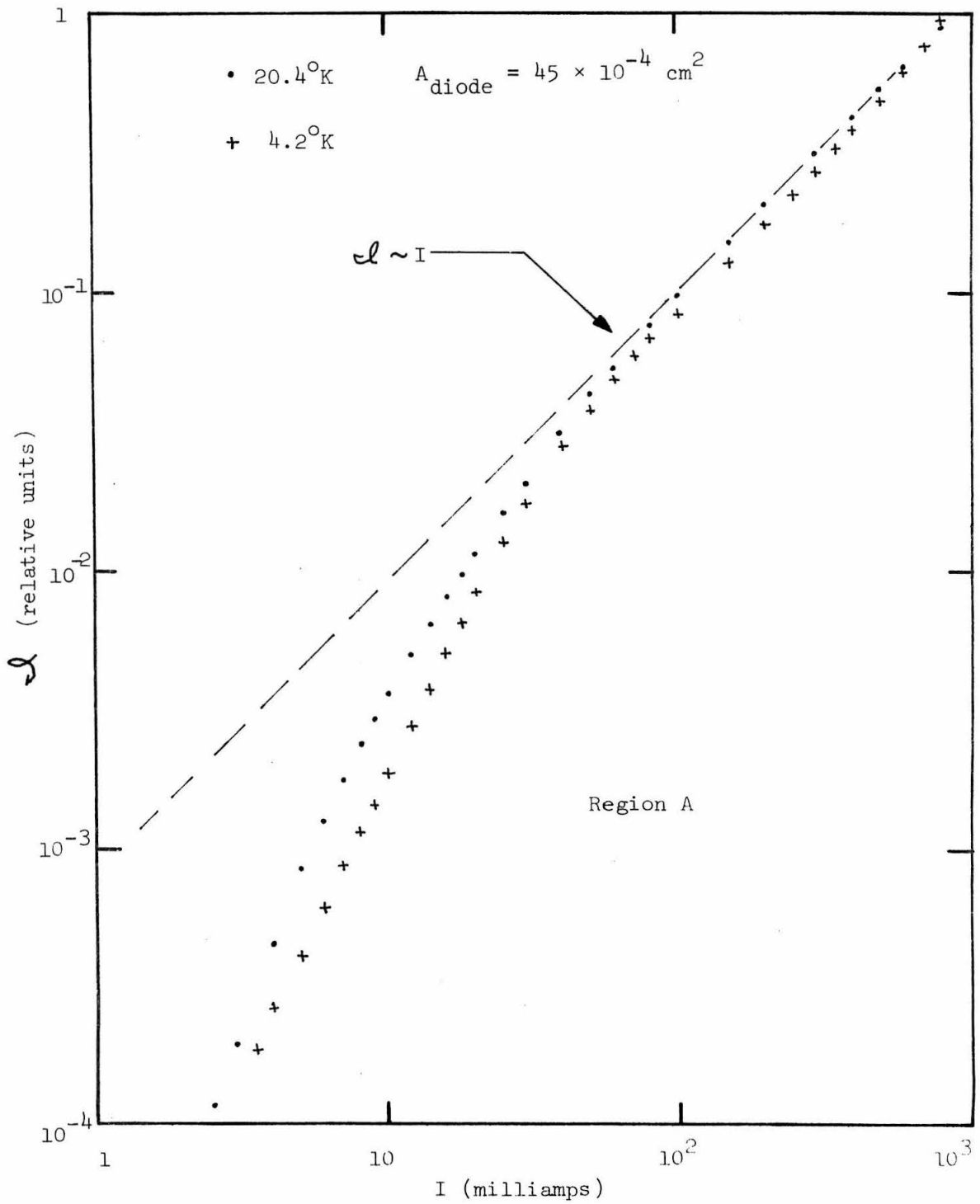Figure 3-3. $\mathcal{J} - I$ Data for Diode J-22

Figure 3-4. $\mathscr{L}$ - I Data for Diode J-23
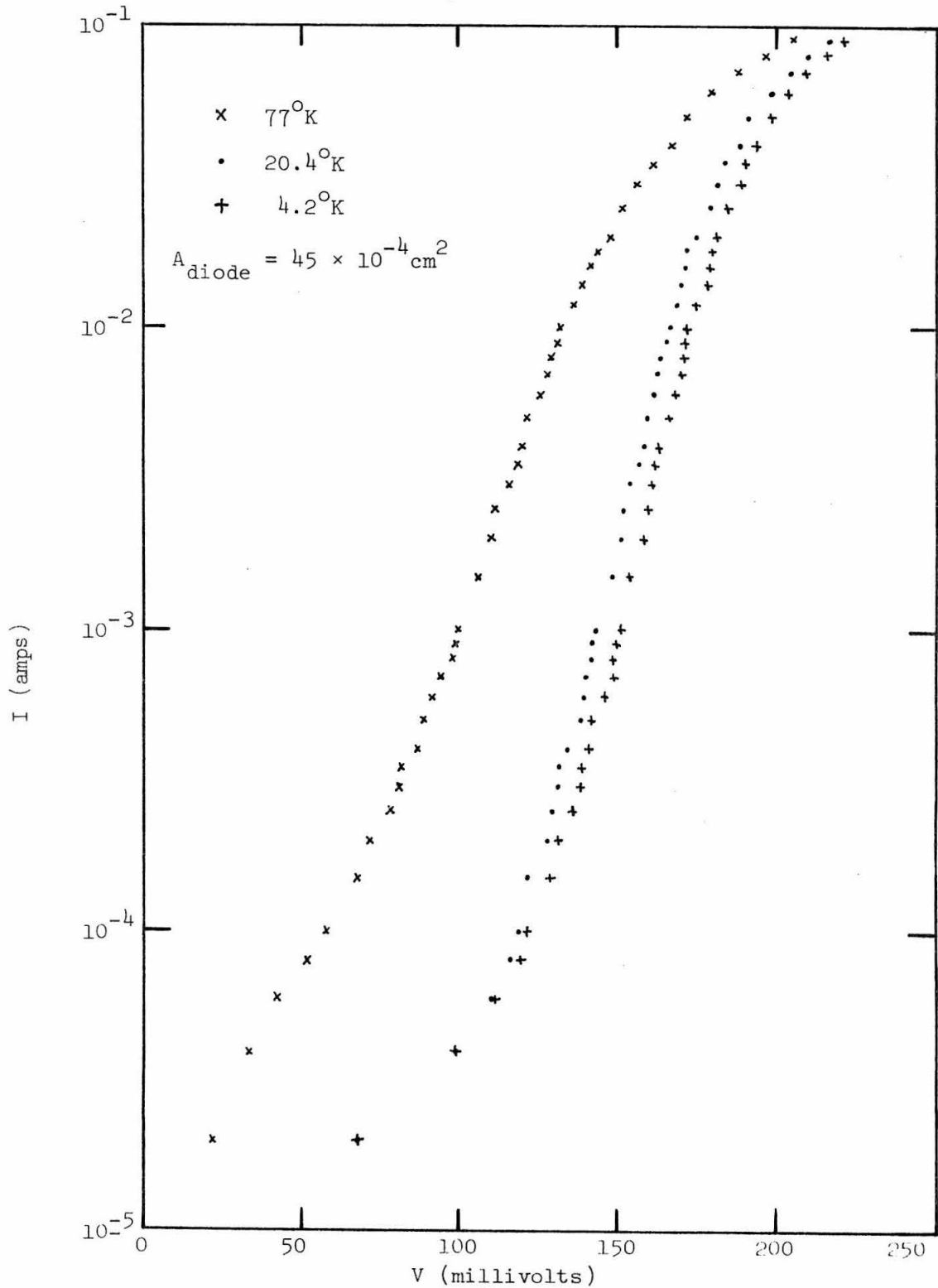
Figure 3-5.   I-V   Data for Diode J-23 ("raw")

in the current at high voltages is due to series resistance.

The I-V characteristics in Figure 3-5 were corrected for series resistance. The "corrected" I-V curves for diode J-23 are shown in Figure 3-6. The upper limit of the corrected curves is approximately the point where the voltage shift due to series resistance is equal to the corrected voltage. Beyond this point, the corrected data are not reliable.

3.4   Diode Junction Capacitance vs. Voltage

Measurements of the differential junction capacitance (C) as a function of applied (DC) voltage (V) are illustrated in Figure 3-7 for diode J-23 at 77°K and 4.2°K. The linear relationship between $(1/C^2)$ and V indicates that the PbTe diodes have "abrupt" junctions. The small change in the slope (S_c) of $(1/C^2)$ vs. V between 77°K and 4.2°K is most likely due to small temperature dependences in the parameters included in S_c (see equations 1-53b and 1-76a).

3.5   Spectral Light Intensity

The stimulated emission spectra, $\mathcal{J}(\lambda)$, provide confirmation of the threshold for stimulated emission (region C of the $\mathcal{J}$-I data). Figure 3-8 displays the $\mathcal{J}$-I data in regions B, C and D for diode J-4 at a temperature of 20.4°K. The corresponding spectral data for J-4 at 20.4°K (near the threshold for stimulated emission)are shown in Figure 3-9. The current at which the narrow bandwidth[*], stimulated mode

---

[*]The narrowness of the spectral lines (about 15$\overset{\circ}{A}$) is limited by the resolution of the monochromator.
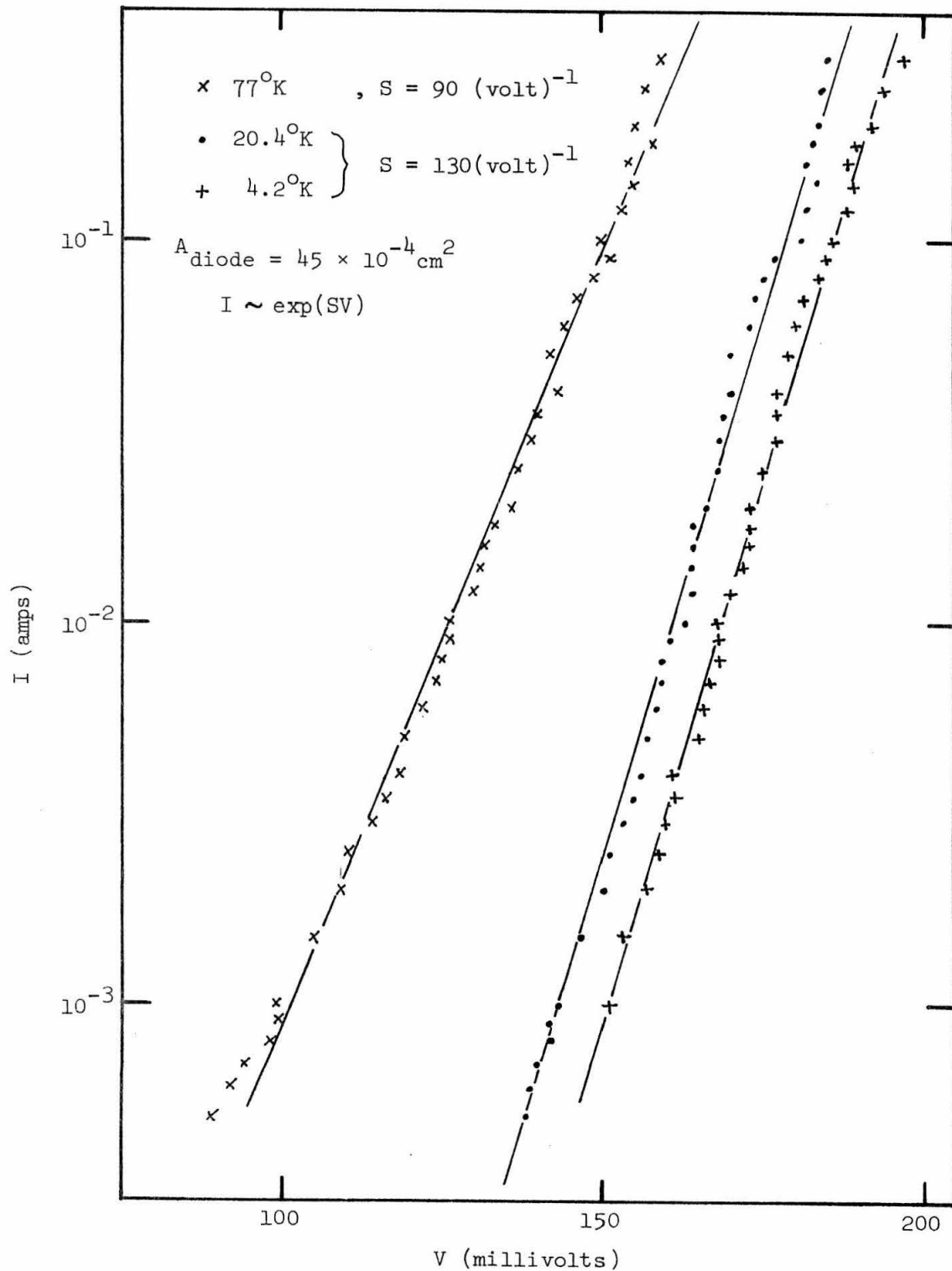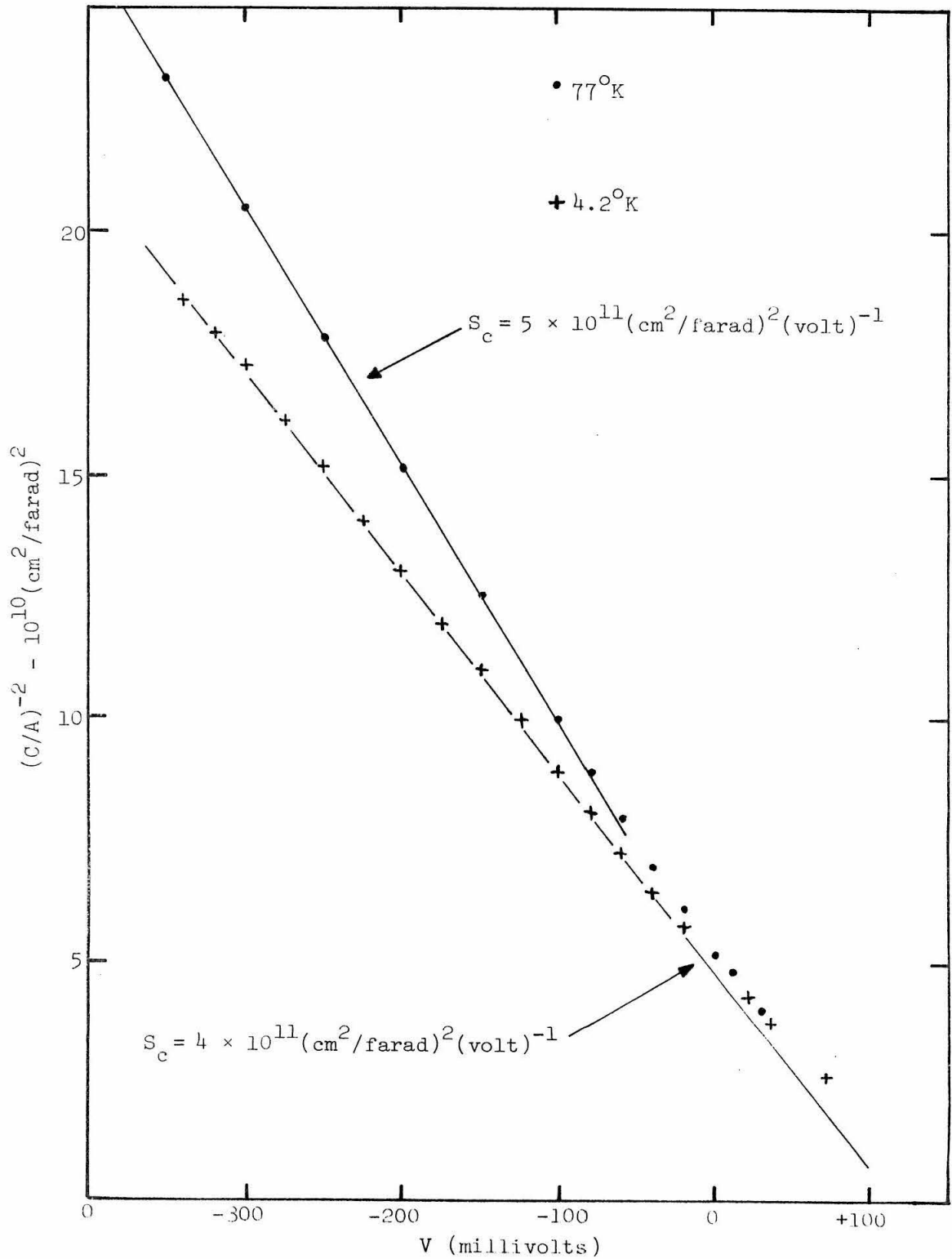
Figure 3-6.   I-V Data for Diode J-23 (corrected)

Figure 3-7. C-V Data for Diode J-25

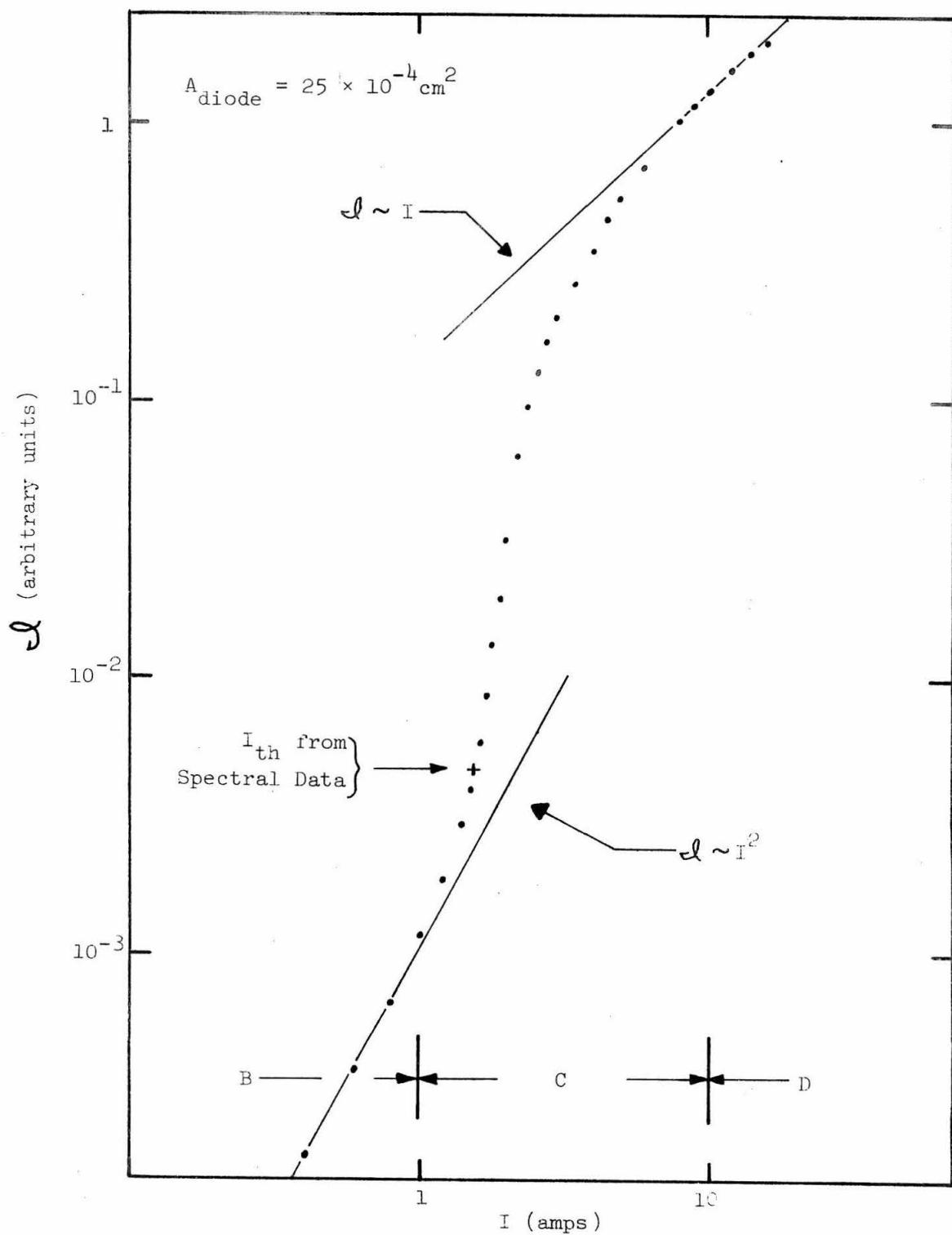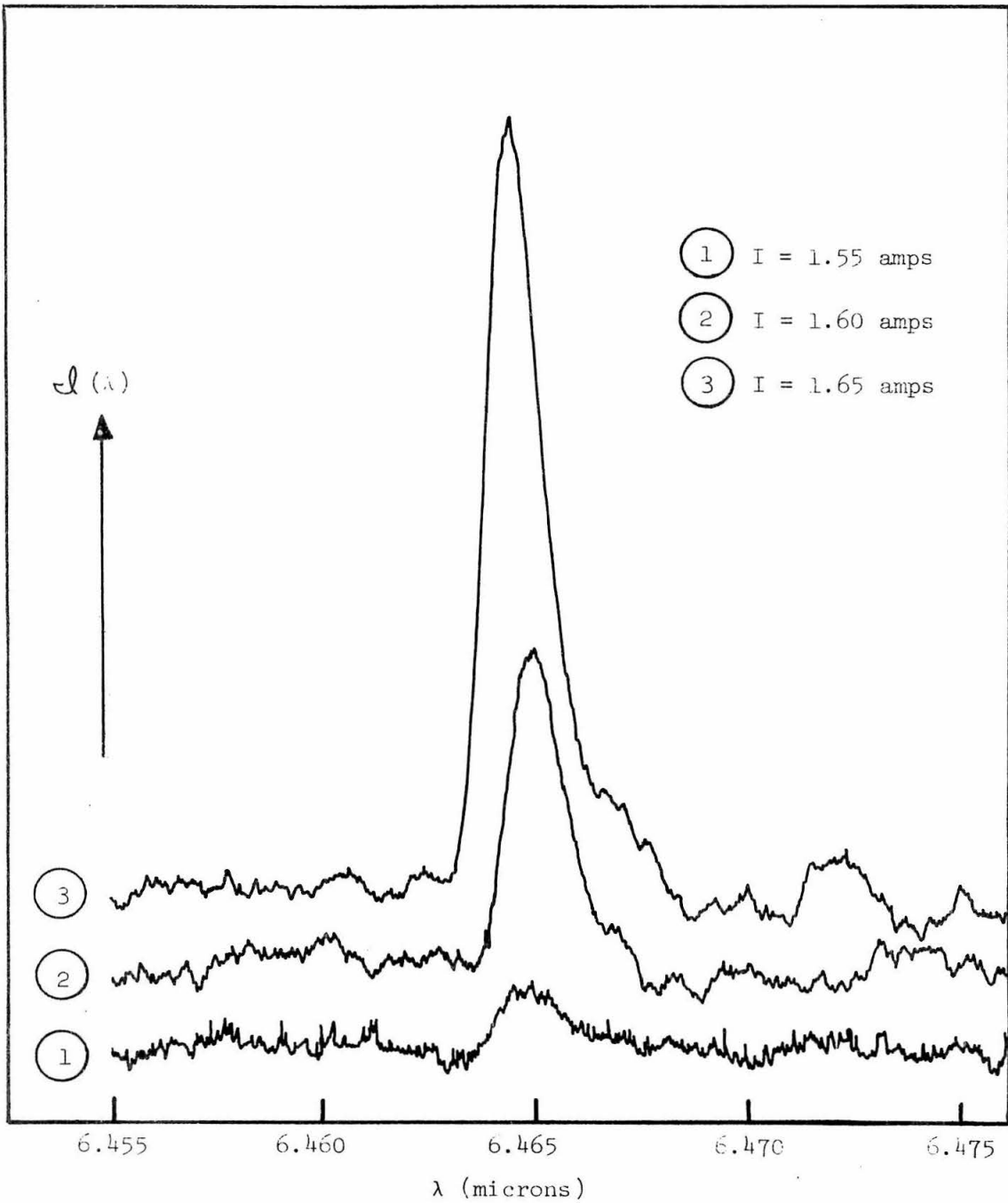Figure 3-8. $\mathcal{L}$ – I Data for Diode J-4 (20.4°K)

Figure 3-9. Spectral Intensity Data for Diode J-4 (20.4°K)

(λ = 6.465μ) appears is the threshold current (I_{th} = 1.55 amps for

J-4). The spectrally determined I_{th} is seen to correspond to the

beginning of region C in Figure 3-8. Therefore, region C is justi-

fiably called the threshold region for stimulated emission. The

emission spectrum of J-4 for a current of 3.0 amps (well above thresh-

old), is shown in Figure 3-10. For I = 3.0 amps, several modes are

oscillating simultaneously, each mode being represented by a relative

peak in the spectrum. Further discussion of the stimulated emission

peaks in Figure 3-10 is obtained in Chapter IV.

3.6 Image-scan and Far-field Intensity

The stimulated radiation intensity, $\mathcal{J}(x)$, in the plane of the

diode's emitting surface as a function of distance (x) perpendicular

to the junction, is shown in Figure 3-11 for diode K-4 at 20.4°K. The

data in Figure 3-11 were obtained using the method illustrated in

Figure 1-4(b). The curve in Figure 3-11 is for a diode-current of

8.0 amps. However, image-scan data were obtained for currents ranging

from 2.0 amps to 8.0 amps, with no significant changes in the relative

shape of the curves for $\mathcal{J}(x)$. In addition to the measurement of

$\mathcal{J}(x)$, the diffracted far-field intensity, $\mathcal{J}(x')$, was measured per

the scheme shown in Figure 1-5a. The plot of $\mathcal{J}(x')$ for diode K-4 at

20.4°K, and for a current of 2.0 amps is shown in Figure 3-12. The

stimulated emission spectrum for J-4 (20.4°K and I = 2.0 amps) is

given in Figure 3-13. The spectrum in Figure 3-13 indicates that the

dominant oscillating mode (λ = 6.48μ) is much more intense than any of

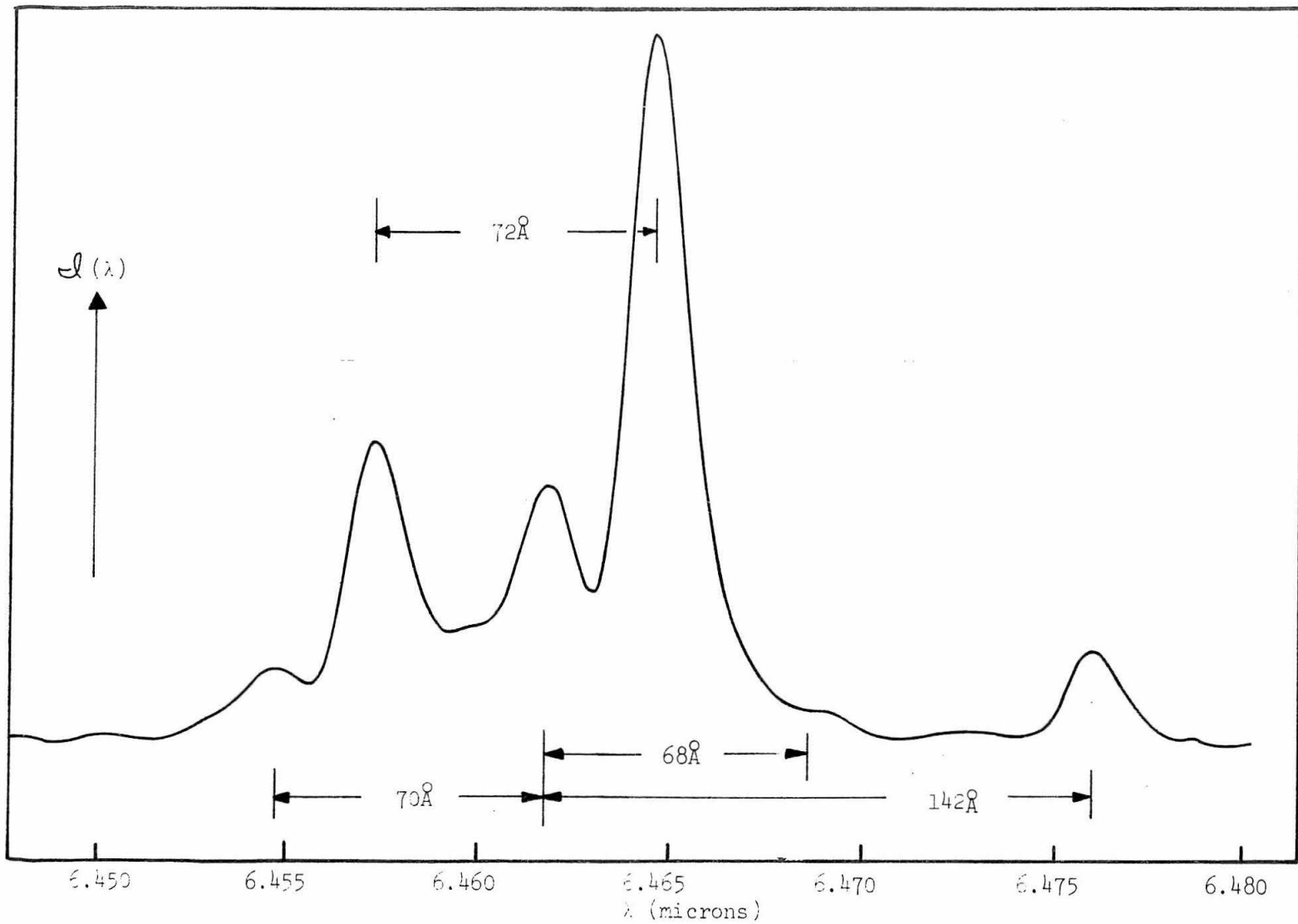the other modes present. The method described in Section 1.3.4 was

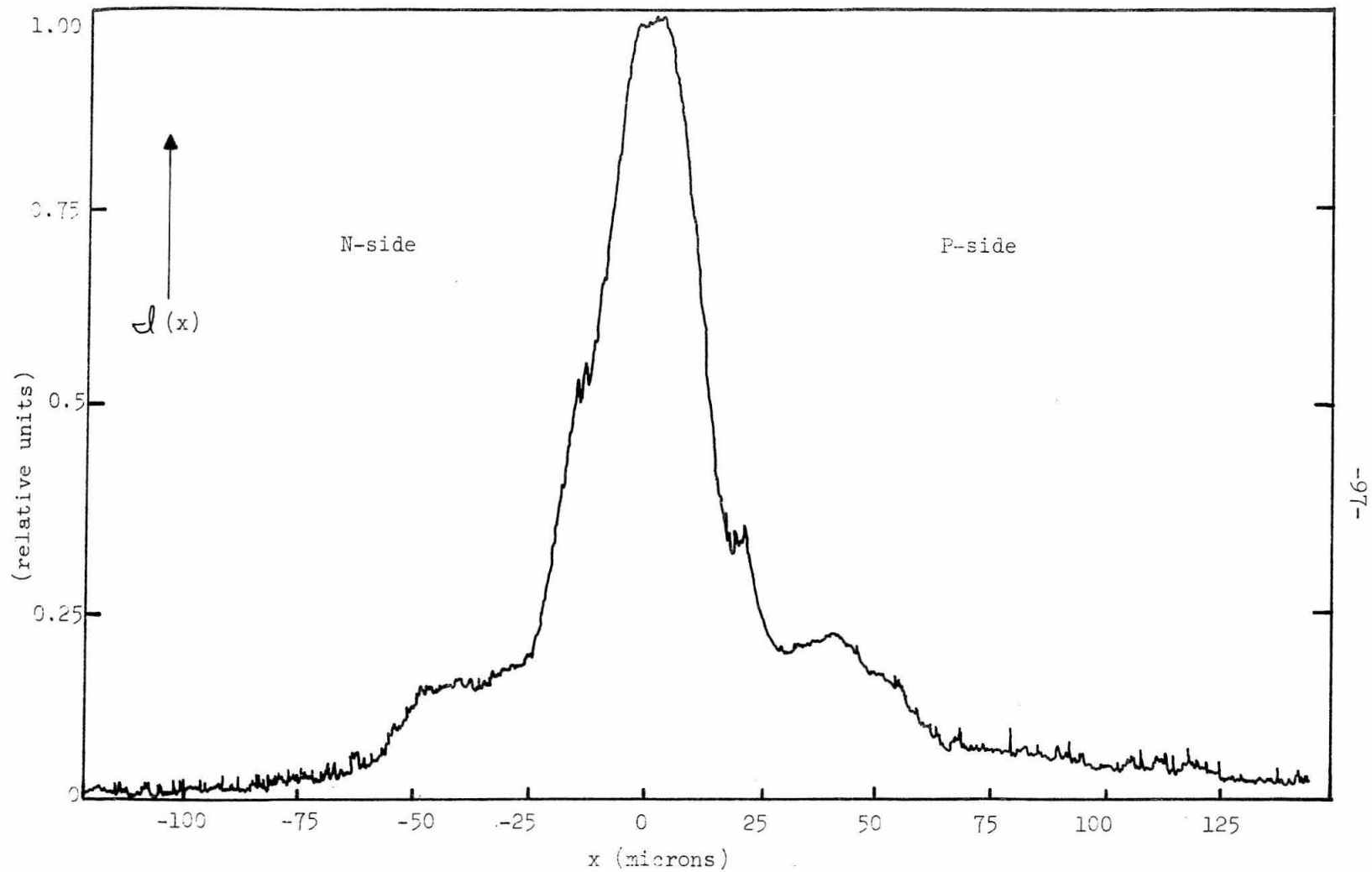Figure 3-19. Spectral Intensity Data for Diode J-4 (I = 3.0 amps, 20.4°K)

Figure 3-11.   Image-Scan Intensity Data for Diode K-4 (I = 8.0 amps, 20.4°K)
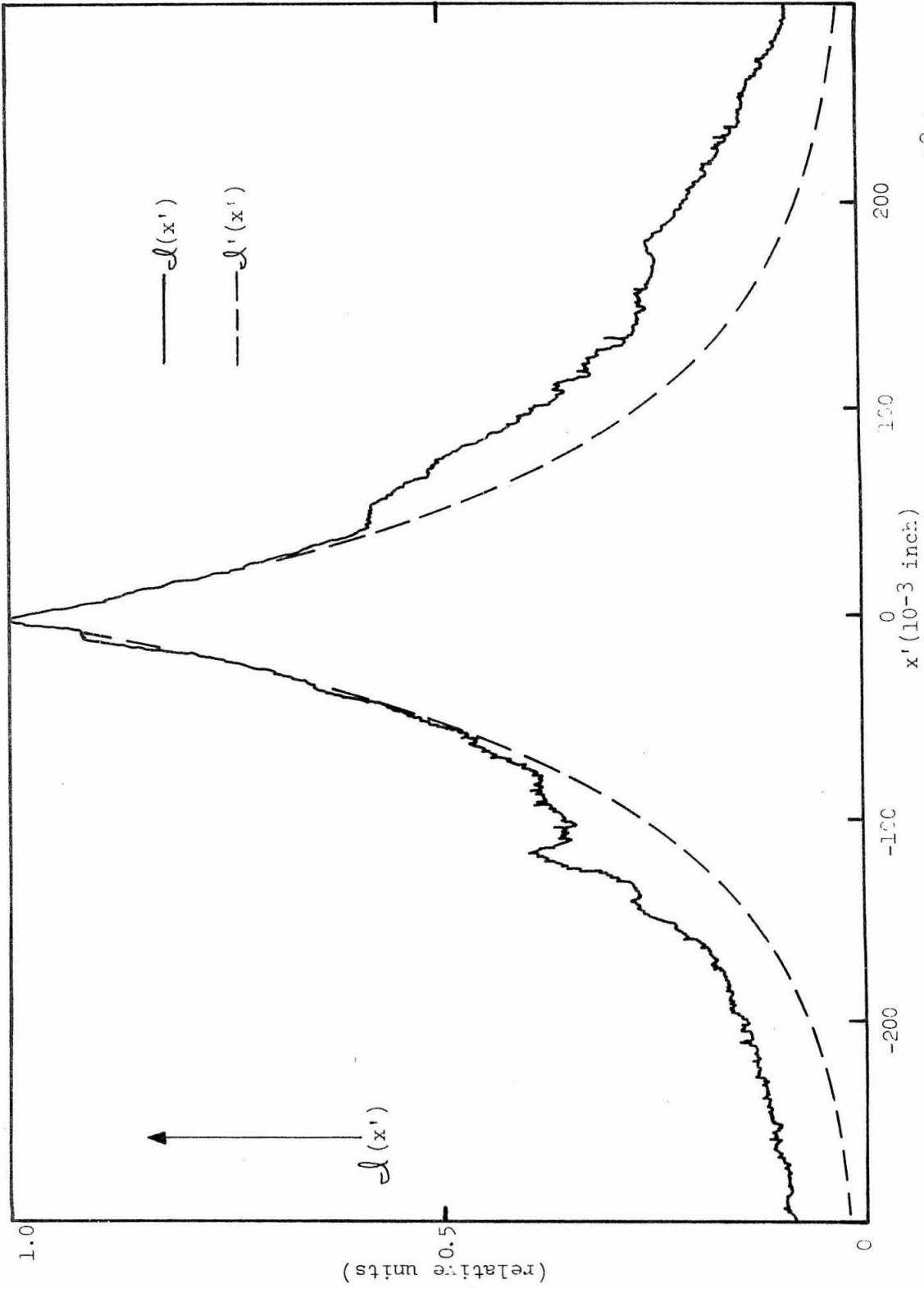
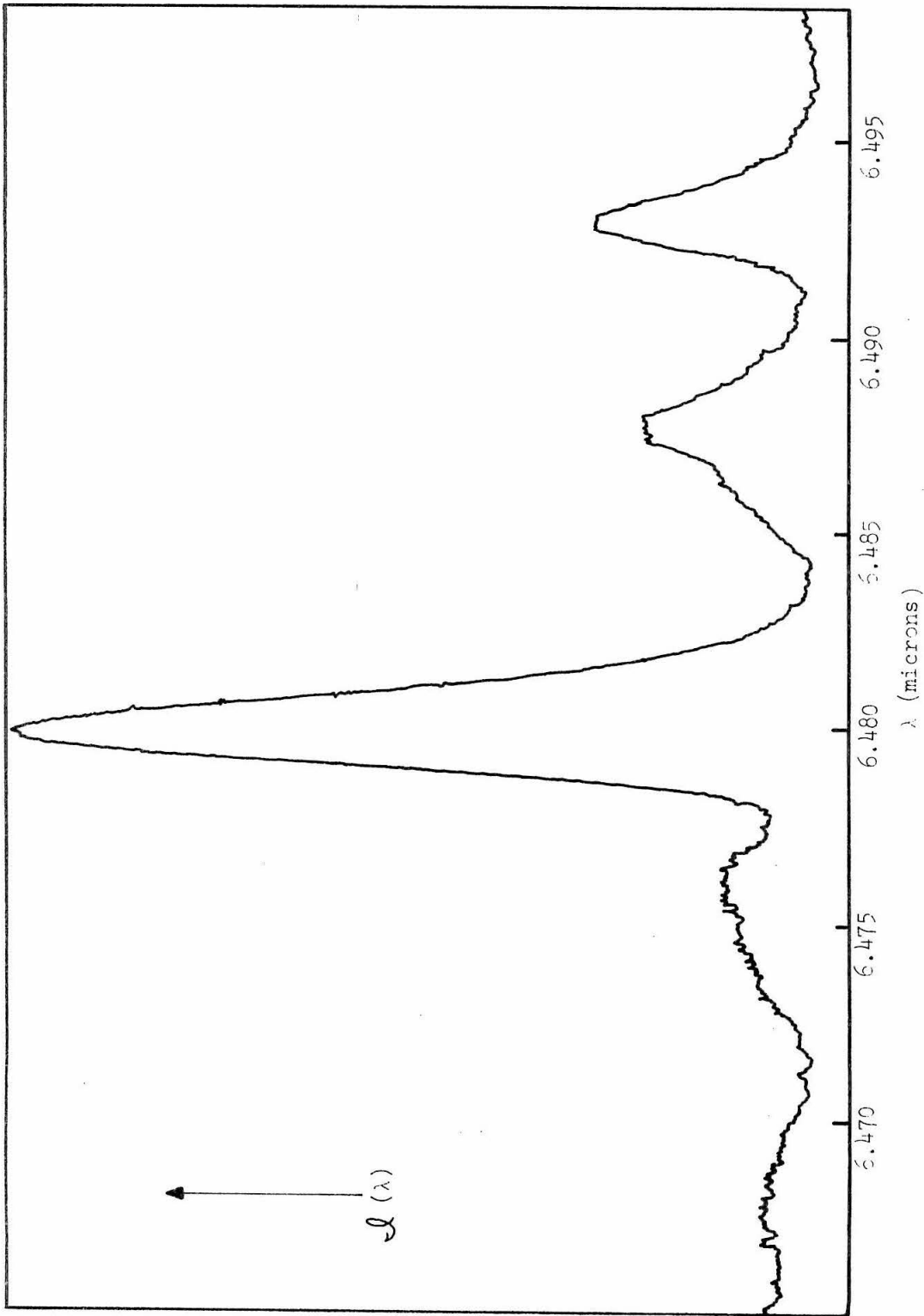Figure 3-12. Far-Field Diffraction Intensity Data for Diode K-4 (H= 2.0 amps, 20.4°K)

Figure 3-13. Spectral Intensity Data for Diode K-4 (I = 2.0 amps, 20.4°K)

used (with the aid of the IBM 7090 computer) to transform the $\mathcal{J}(x')$
data in Figure 3-12 into corresponding values for $\mathcal{J}_F(x)$. The result
of the numerical transformation is illustrated in Figure 3-14. A
further analysis of Figure 3-14 is given in Chapter IV.

3.7 Threshold Current for Stimulated Emission vs. Reciprocal Cavity Length

The threshold current (per unit junction area) for stimulated
emission (J_{th}), given by equation 1-66, is inversely proportional to
the diode cavity length (L) . In order to observe (experimentally) the
variation in J_{th} with changes in L , diodes which are alike in every
other respect are required. To achieve this, the diodes used should
be made from adjacent areas of the diffused PbTe crystal. In order
to obtain nearly identical diodes for this experiment, diode J-4 was
recleaved to form two additional diodes, K-4 and K-42. Each of the
two new diodes had cavity lengths shorter than J-4. The measured
values of J_{th} for the three diodes, as a function of their reciprocal
cavity length, were plotted in Figure 3-15. The results of Figure
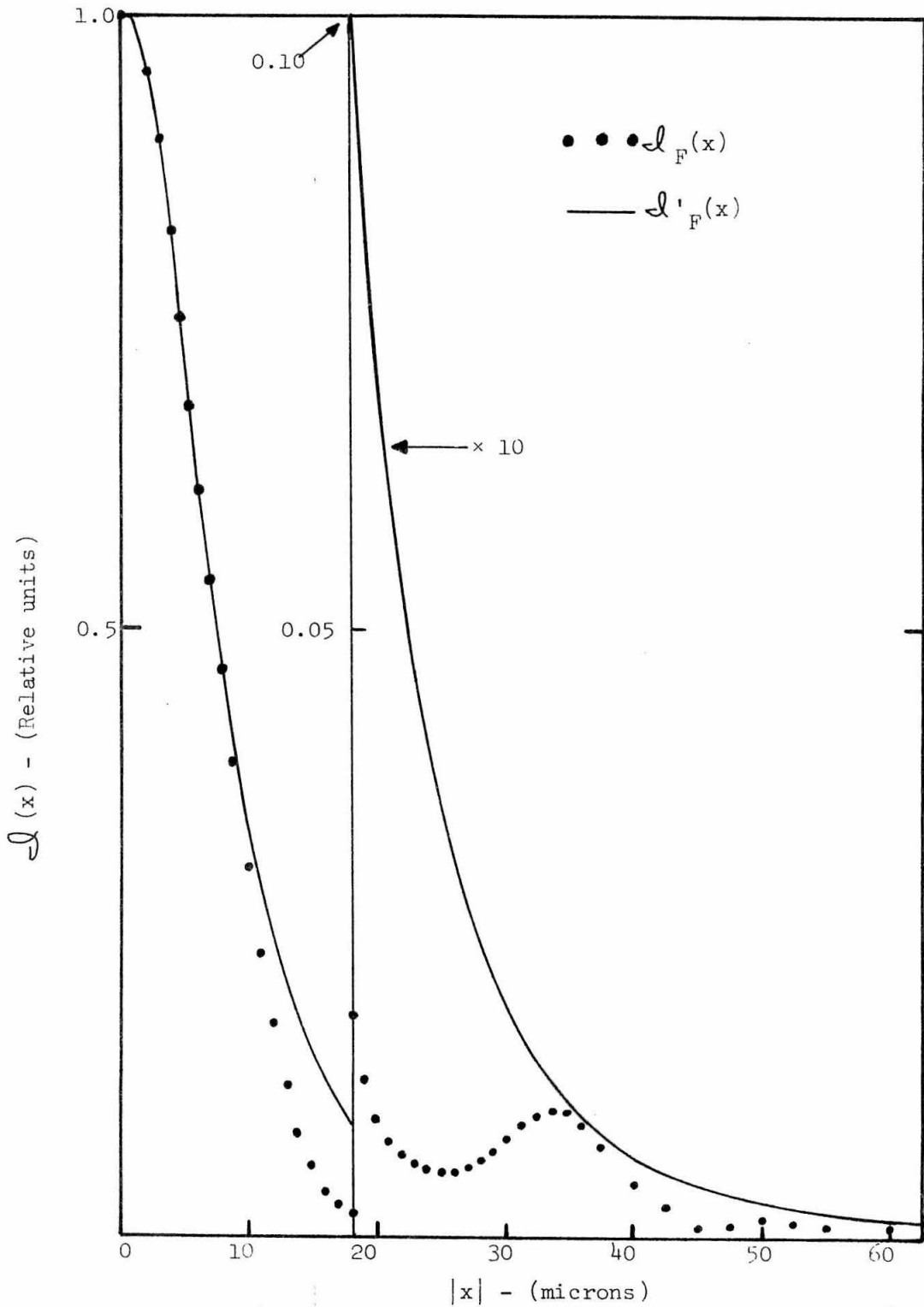3-15 are discussed in Chapter IV.

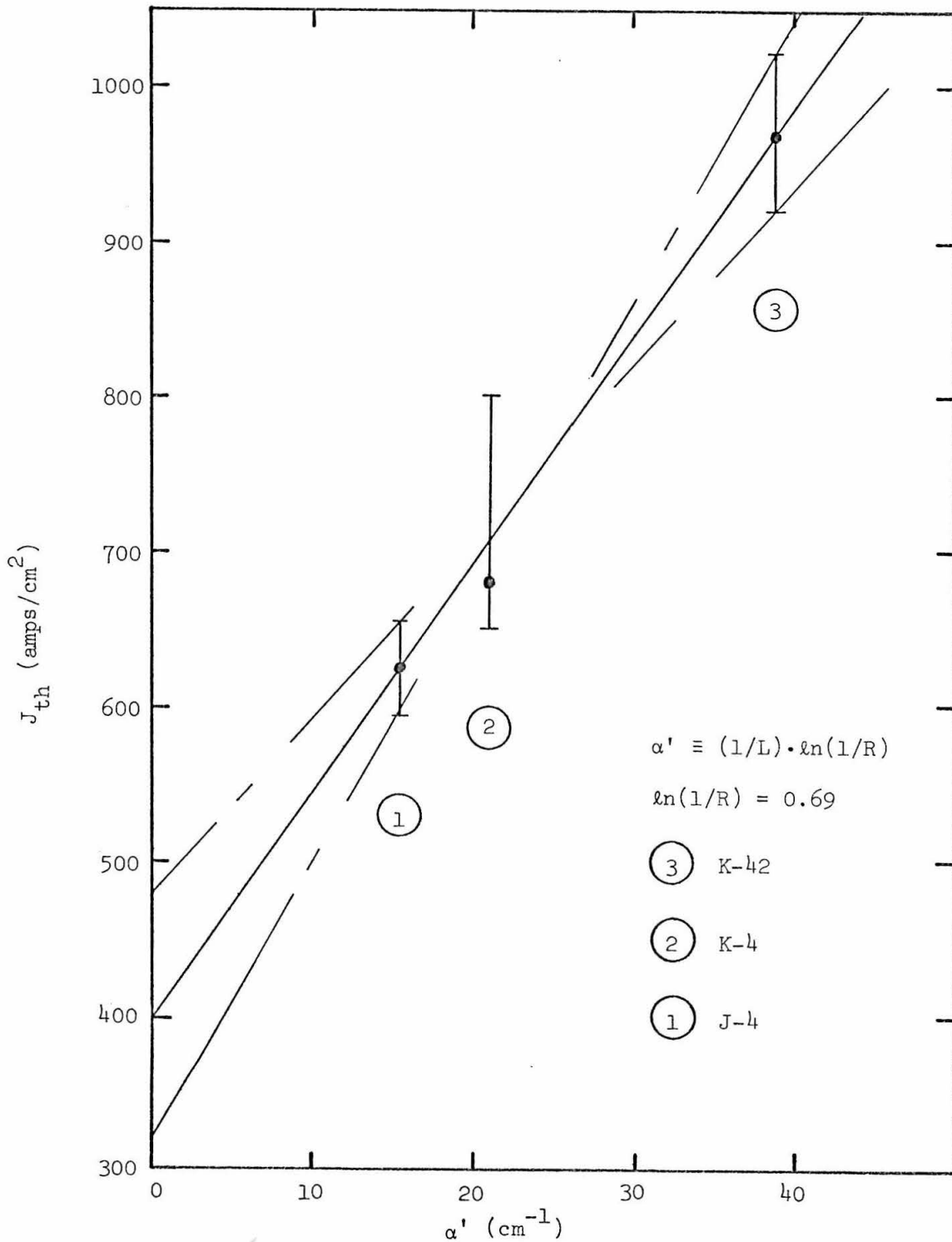Figure 3-14. Intensity Profile Data for Diode K-4 (20.4°K)

Figure 3-15. J_{th} vs. $1/L$ Data (20.4°K)

IV. DATA ANALYSIS AND DISCUSSION

4.1 General Remarks

This chapter contains the over-all analysis of the data presented
in Chapter III. The discussion is broken up into two main areas:
(a) light emission and electrical characteristics at low current levels
(regions A and B, with currents less than I_{th}), and (b) stimulated light
emission at high current levels (regions C and D with currents greater
than I_{th}). By arranging the analysis and discussion of the data as
outlined above, an optimum amount of comparison of the different types
of data is hopefully achieved.

4.2 Light Emission and Electrical Characteristics at Low Current Levels

4.2.1 Electrical Characteristics

The I-V data in Figure 3-6 indicate an exponential dependence of
current on voltage. The (natural) logarithmic slopes obtained from the
data have the same value of $130(\text{volt})^{-1}$ for $4.2^{\circ}K$ and $20.4^{\circ}K$, with a
smaller value of $90(\text{volt})^{-1}$ for $77^{\circ}K$. It therefore appears that the cur-
rent (at least below $20.4^{\circ}K$) is not thermionic in nature, since the
exponential coefficient would then be inversely proportional to the
absolute temperature (as indicated by equation 1-55). In addition, the
slope (q/kT) for thermally generated current flow has values of
$150(\text{volt})^{-1}$, $570(\text{volt})^{-1}$ and $2760(\text{volt})^{-1}$ for temperatures of $77^{\circ}K$,
$20.4^{\circ}K$ and $4.2^{\circ}K$, respectively. However, owing to the large increase in
current (at a given voltage) in going from $20.4^{\circ}K$ to $77^{\circ}K$ (Fig. 3-6), one
might expect that the current flow is thermionic at $77^{\circ}K$, with a slope
$(qv/\beta kT)$, and where $\beta = 5/3$. The thermal saturation current (I_{o} in

equation 1-55) for a p-n junction formed by extrinsic semiconductor
materials is given by (31)

$$I_o = (qkT)^{1/2} \left[\frac{1}{N_d}(\frac{\mu_h}{\tau_h})^{1/2} + \frac{1}{N_a}(\frac{\mu_e}{\tau_e})^{1/2} \right] n_i^2 \qquad (4-1)$$

where μ and τ are the carrier mobility and lifetime (the sub-
scripts h and e denoting holes and electrons), and where n_i is
the intrinsic carrier concentration given by 1-19. The reliable cal-
culation of I_o at low temperatures for PbTe, using 4-1, is prohibited
by the lack of reliable data for μ, τ and n_i .

The logarithmic slope (S_T) for photon-assisted tunneling (equa-
tion 1-75) was calculated using the value of S_c obtained from the
C-V data in Figure 3-7, and using the reduced tunneling mass discussed
in Section 1.3.5.2 ($M_T = 0.011 \ m_o$). The resulting (calculated) value
for S_T is

$$(S_T)_{calc.} \simeq 150 \, (volt)^{-1} \qquad (4-2)$$

in fair agreement with the measured logarithmic slope of the I-V data
at 20.4°K and 4.2°K in Figure 3-6.

In summary, the following results for low temperatures (20.4°K
and 4.2°K), discussed in the above paragraph, indicate that the low-
level current flow is due to tunneling; (a) the temperature independence
of the logarithmic slopes of the I-V characteristics, (b) the measured
value of the logarithmic slope being much less than the slope (q/kT)
for the thermionic model and (c) the rather good agreement of the

measured slope with the calculated value of S_T .

4.2.2 Light Emission Characteristics in Region A

The $\mathcal{l}$ -I data in region A, shown in Figures 3-1 and 3-4, indicate a linear dependence of total radiation intensity on current at the high current end of the region. At about the middle of the region, the light intensity begins to fall off more rapidly with decreasing current. The region may therefore be characterized by

$$\mathcal{l} \sim I^m \tag{4-3}$$

where $m = 1$. In the analysis of Section 4.2.1, the I-V characteristic for region A was demonstrated to be

$$I \sim e^{S_T V} \tag{4-4}$$

where S_T is the exponential coefficient obtained in Section 1.3.5.2 for "diagonal" tunneling. Using the ideas developed in Section 1.3.2, we may write 4-3 as

$$\mathcal{l} \sim \eta_r I \sim \eta_r e^{S_T V} \tag{4-5a}$$

where

$$\eta_r \sim I^{m-1} \tag{4-5b}$$

is the radiative quantum efficiency. As I increases in region A, m approaches the value 1 and η_r becomes constant, giving

$$\mathcal{l} \sim e^{S_T V} \tag{4-6}$$

as predicted by the model for radiative diagonal tunneling. In the

low current part of Region A (i.e. where m > 1), the radiative recombination is competing with a "non-radiative" process.[*] However, the I-V data exhibit a single exponential slope for all values of I in region A . Therefore, the I-V data indicate that the same exponential slope (S_T) obtains for both radiative and nonradiative diagonal tunneling. This result is certainly a tenable one, since the transition matrix elements involved in the calculation of S_T do not necessarily require radiative transitions (24).[**] As a result, the total current flow due to both radiative and nonradiative recombination can be expressed as in 4-4, which is indeed verified by the I-V data (Section 4.2.1). However, since the radiative recombination is competing with a nonradiative process, the $\mathscr{l}$ -V characteristic must be written as in 4-5.

---

[*] The radiative recombination is competing with either (a) a nonradiative process, or (b) a radiative process in which the emitted photon wavelength exceeds the long-wavelength limit of the detector. (For a Ge:Hg detector, $\lambda_{max} \approx 15\mu$) .

[**] The only requirement is that the transition matrix elements (M_{cv}) be of the form given by equation 5 of reference (24), i.e.

$$M_{cv} = \int \overline{\psi}_c(\vec{r}) \; \hat{P} \; \psi_v(\vec{r}) \; dV$$

where $\psi_c(\vec{r})$ and $\psi_v(\vec{r})$ are the conduction and valence band wave functions, given by 1-51c and 1-51d, respectively (the "bar" over $\psi_c(r)$ denotes complex conjugation), and where $\hat{P}$ is the momentum operator.

A possible model for the source of nonradiative recombination
is the existence of impurity energy levels within the band-gap. Even
though "impurity" levels due to excess stoichiometric proportions of Pb
and/or Te atoms lie very near the band edges (as discussed in Section
1.1.3.2), foreign-impurity atoms may give rise to carrier-trapping
levels deep inside the band-gap. These impurities may provide for the
radiationless relaxation and recombination of tunneling electrons and
holes through either one or several impurity levels, as illustrated in
Figure 4-1. This allows for the nonradiative, diagonal-tunneling recom-
bination of electrons and holes. Again following the ideas of Section
1.3.2, the quantum efficiency (η_r) for radiative transitions, as used
in 4-5, may be expressed as

$$\eta_r = \frac{t_b}{t_b + t_r} \qquad (4-7)$$

where t_b and t_r are the respective nonradiative and radiative life-
times. As the tunneling-current (I) increases, it is expected that the
impurity levels within the band-gap would become saturated by the non-
radiative recombination process. As a result, the nonradiative lifetime
would increase with respect to the radiative lifetime, i.e. (t_b/t_s)
would increase. Hence in the limit of $t_b \gg t_r$, the radiative
quantum efficiency (η_r) in 4-7 would approach unity. This is consistent
with the experimental observation of $m \to 1$ as I increases. It then
follows (from the $\mathcal{J}$ -V relationship in 4-6 and the equality $\eta_r = 1$)
that the total current flow can be supported by radiative, "diagonal"
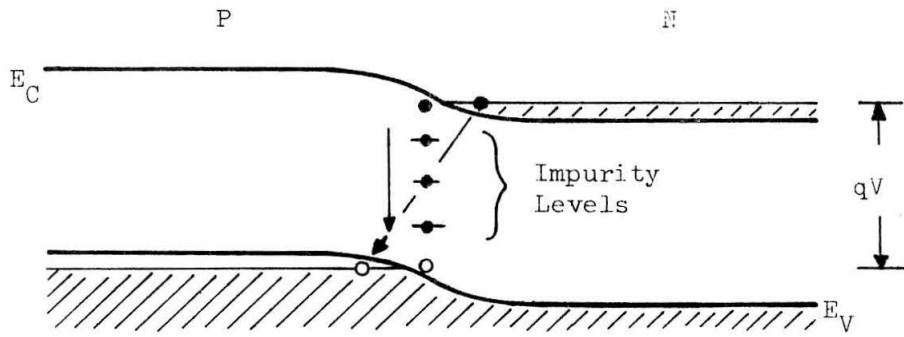tunneling in that part of region A where $\mathcal{J} \sim I$. In summary, the

Figure 4-1.   Model for Radiationless Diagonal Tunneling
via Impurity Levels

recombination radiation observed in region A is explained by the model for photon-assisted "diagonal" tunneling, with the $\mathscr{l}$-V characteristic given by 4-5.

4.2.3 Light Emission Characteristics in Region B

The total intensity of light emission in region B is characterized by the relationship $\mathscr{l} \sim I^2$, as illustrated in Figures 3-1 and 3-3. The rather abrupt transition from $\mathscr{l} \sim I$ in region A to $\mathscr{l} \sim I^2$ in region B indicates a possible change in the current injection mechanism. Although the I-V data (Figure 3-6) cover only region A, the transition from $\mathscr{l} \sim I$ in region A to $\mathscr{l} \sim I^2$ in region B in the $\mathscr{l}$-I data suggests that the current injection mechanism changes from photon-assisted tunneling in region A to thermionic injection in region B. Again following Section 1.3.2, we now have the case expressed by 1-60 and with $m = 2$. Using 1-61a, we have $\eta_s \sim I$, which for the case of $t_b \gg t_s$, yields

$$(t_b/t_s) \sim I \qquad (4-8a)$$

where t_b is the nonradiative lifetime and t_s is the spontaneous (radiative) lifetime. Since t_s is constant, we then have

$$t_b \sim I \qquad (4-8b)$$

The above empirical results can be explained on the basis of nonradiative carrier recombination via impurity carrier-trapping levels lying in the band-gap, presented as follows. According to 1-58b, we may write the total diode current as

$$I = I_b + I_s \qquad (4\text{-}9a)$$

with

$$I_b \equiv \frac{qn_2}{t_b} \qquad (4\text{-}9b)$$

and

$$I_s \equiv \frac{qn_2}{t_s} \qquad (4\text{-}9c)$$

where n_2 is the total number of injected minority carriers, and where I_b and I_s are the current components due to nonradiative and radiative recombination, respectively. We now postulate the presence of N_t^o impurity (trapping) states within the band-gap and within approximately a diffusion length of the junction. Next we write

$$N_t^o = N_t^e + N_t^f \qquad (4\text{-}10)$$

where N_t^e and N_t^f are the numbers of empty and full traps, respectively. Now, the quantity I_b may be written as

$$I_b = \frac{qN_t^e \, n_2}{t_1} \qquad (4\text{-}11)$$

where t_1 is the (constant) "lifetime" for the trapping of a carrier by one empty trap. Using 4-11, 4-9 becomes

$$I = \frac{qN_t^e \, n_2}{t_1} + \frac{qn_2}{t_s} \qquad (4\text{-}12a)$$

which gives

$$n_2 = \frac{I \, t_1 t_s}{q(N_t^e \, t_s + t_1)} \qquad (4\text{-}12b)$$

Now for steady-state conditions we may write

$$\frac{dN_t^e}{dt} = \frac{N_t^f}{t_2} - \frac{n_t N_t^e}{t_1} = 0 \qquad (4\text{-}13a)$$

or

$$\frac{N_t^f}{t_2} = \frac{n_2 N_t^e}{t_1} \qquad (4\text{-}13b)$$

where t_2 is the (constant) lifetime of a filled trap. Using 4-10 in 4-13b, we get

$$N_t^e = \frac{N_t^o}{[(n_2 t_2/t_1) + 1]} \qquad (4\text{-}13c)$$

Substituting 4-12b into 4-13c, we then obtain

$$N_t^e = \frac{N_t^o}{\left[(\frac{1}{q}) \left(\dfrac{I\, t_s t_2}{N_t^e\, t_s + t_1} \right) + 1 \right]} \qquad (4\text{-}14a)$$

For a sufficiently large injection current, i.e. for $(I\, t_2/q) > N_t^o$ and $(I\, t_2/q) > (t_1/t_s)$, we can write 4-14a as

$$N_t^e \simeq \frac{q N_t^o\, t_1}{I\, t_s t_2} \sim I^{-1} \qquad (4\text{-}14b)$$

i.e. the number of empty traps is inversely proportional to the total current (I). Now, if the current flow is due mainly to nonradiative recombination via traps (i.e. $t_b \ll t_s$), equation 4-12a gives

$$I \simeq q \frac{N_t^e \, n_2}{t_1} \sim n_2 \, N_t^e \qquad (4\text{-}15a)$$

From 4-14b and 4-15a it follows that

$$n_2 \sim \frac{I}{N_t^e} \sim I^2 \qquad (4\text{-}15b)$$

and hence

$$\mathcal{J} \sim I_s = \frac{q n_2}{t_s} \sim I^2 \qquad (4\text{-}16a)$$

or

$$\mathcal{J} \sim I^2 \qquad (4\text{-}16a)$$

which is just the empirical result presented in the last paragraph. We also obtain from this analysis

$$n_s = \frac{I_s}{I} \sim I \qquad (4\text{-}16b)$$

and

$$t_b \sim n_s \sim I \qquad (4\text{-}16c)$$

thus completing the explanation of the empirical results on the basis of trapping impurity-levels in the band-gap.

4.3 Stimulated Light Emission at High Current Levels

4.3.1 Total Light Emission in Regions C and D

Following the discussion in Section 1.2.1, and using equation
1-47c, we may write the total photon emission rate (W_T) as the sum of
the total spontaneous and induced (stimulated) rates (W_s and W_I,
respectively), or

$$W_T = W_s + W_I = W_s(1 + \frac{N_p}{n_m}) \tag{4-17}$$

In 4-17 N_p is the total number of photons in all of the stimulated
(oscillating) modes and n_m is the total number of modes in the spon-
taneous spectrum. For the case of radiative recombination far below
the threshold for stimulated emission (region B), $N_p \ll n_m$. Therefore
$W_T \simeq W_s = 1/t_s$, where t_s is the spontaneous lifetime. However, as
the current approaches and surpasses the threshold for stimulated
emission, the total number of photons (N_p) in the cavity approaches and
surpasses n_m. As a result, the total emission intensity increases
sharply, as indicated by the data in region C of Figures 3-1, 3-3 and
3-8.

As the input power to the diode is increased, the photon-field
builds up to the point where $N_p \gg n_m$. In the limit of $N_p \gg n_m$,
the total emission rate is essentially the induced rate, or

$$W_T \simeq W_I \sim \frac{N_p}{t_s} \tag{4-18}$$

where t_s is constant. The total radiated power (P) is related to the

external power supplied to the p-n junction (IV) by

$$P = \frac{N_p h \nu_p}{t_s} \sim IV \qquad (4\text{-}19)$$

Since the junction voltage at high current-injection levels is essentially constant, and since the total radiated intensity ($\mathcal{l}$) is just the power per unit area, we have

$$\mathcal{l} \sim N_p \sim I \qquad (4\text{-}20)$$

The case described by 4-20 obtains in region D, as illustrated by Figures 3-1 and 3-8. From Figures 3-1 and 3-8, $\mathcal{l} \sim I$; hence the differential quantum efficiency (i.e. $d\mathcal{l}/dI$) is constant in region D. Therefore region D is called the saturation region for stimulated emission (Section 3.2).

The over-all increase in the measured values of $\mathcal{l}$ in going through region C into region D is accentuated by the fact that the spatial character of the radiation changes from isotropic (at the beginning of region C) to essentially collimated. The isotropic radiation obviously suffers the greater loss (absorption) in the diode before getting out of the cavity, where it is detected.

4.3.2 Spectral Light Intensity Data

The narrow-band spectral lines which characterize the stimulated emission from PbTe diodes are shown in Figures 3-9 and 3-10. As indicated by Figure 3-9 (for a liquid hydrogen cold-finger at $20.4^{\circ}K$), an increase in current at threshold gives rise to a single, dominant

oscillating mode. Figure 3-10 (20.4°K) shows that as the diode power (current) is increased, several modes can oscillate simultaneously, with the dominant mode being the one for which the gain, $\gamma(\nu)$ in equation 1-62, is largest.

The data in Figure 3-10 indicate the presence of two families of stimulated modes. The existence of different families of modes is easily understood from the condition for constructive interference given by 1-50. Microscopic "steps" in the cleaved faces (which form the reflecting ends of the diode cavity) can form individual cavities, each with its own characteristic length (L) . Therefore, it is indeed possible to have several families of modes which can oscillate simultaneously. The measured wavelength separation for both families of modes is $\Delta\lambda = 70\text{Å} (\pm 2\text{Å})$. The "effective" index of refraction (n'_r) defined by

$$n'_r \equiv n_r \left[1 - (\frac{\lambda}{n_r})(\frac{dn_r}{d\lambda}) \right] \tag{4-21a}$$

can be expressed in terms of $\Delta\lambda$, λ and L by using 1-67, or

$$n'_r = \frac{\lambda^2}{2L(\Delta\lambda)} \tag{4-21b}$$

Using the following experimental values for diode J-4,

$$\Delta\lambda = 72 \pm 2\text{Å}$$
$$\lambda = 6.46 \times 10^{-4} \text{ cm}$$
$$L = 0.05 \text{ cm} \tag{4-22a}$$

the calculated value of n'_r is

$$n_r' = 6.0 \pm 0.2 \qquad\qquad (4\text{-}22b)$$

This result is consistent with the published value $n_r = 5.8$ for PbTe (32). Therefore, no dispersion effects are evident from the mode separation data in Figure 3-10.

4.3.3 Stimulated Light Intensity Profile and Mode Confinement

4.3.3.1 Discussion of the intensity profile data. The image-scan intensity data, $\mathcal{I}(x)$, shown in Figure 3-11, are a measure of the total stimulated light intensity from all oscillating modes of the diode (as a function of the distance x perpendicular to the junction). As illustrated in Figure 3-13, there are several modes in the stimulated emission spectrum of the diode, with the dominant mode being at $\lambda = 6.48\mu$. Since the different modes need not occupy the same volume in the diode cavity, the "bumps" in the decaying "tails" of $\mathcal{I}(x)$ in Figure 3-11 might very well be due to separate oscillating modes. Conversely, the source-intensity profile $\mathcal{I}_F(x)$ in Figure 3-14 (obtained from the diffraction pattern intensity $\mathcal{I}(x')$ of Figure 3-12 using the method described in Section 1.3.4), is due almost entirely to the dominant mode. The effects of interference with the other, weaker modes is manifest in $\mathcal{I}_F(x)$ by the small amplitude valleys and peaks on either side of the dominant peak. Therefore, the true intensity profile of the dominant mode lies between the two curves $\mathcal{I}_F(x)$ and $\mathcal{I}(x)$ displayed in Figures 3-14 and 3-11, respectively. The effects of the interference of different modes on the far-field intensity ($\mathcal{I}(x')$ in Figure 3-12) are expected to be the largest for values

of x' away from the peak. Proceeding on the assumption that $\mathcal{J}(x')$ is not affected by mode interference for small values of x', we may extrapolate the exponential dependence of $\mathcal{J}(x')$ on x' from small values of x' to include the entire range of the far-field pattern. The result of this extrapolation, $\mathcal{J}'(x')$, is shown in Figure 3-12. By carrying out the same calculations with $\mathcal{J}'(x')$ as were used to obtain the source intensity $\mathcal{J}_F(x)$, we now may obtain the "true" source intensity $\mathcal{J}'_F(x)$ of the single dominant mode. The resulting curve for $\mathcal{J}'_F(x)$ is shown in Figure 3-14, together with $\mathcal{J}_F(x)$. As seen in Figure 3-14, the curve $\mathcal{J}'_F(x)$ is the envelope of $\mathcal{J}_F(x)$, and is apparently free of any interference effects.

In summary, the net difference between the curve $\mathcal{J}(x)$ and the curve $\mathcal{J}'_F(x)$ (illustrated together in Figure 4-2) is just that due to all oscillating modes and a single oscillating mode, respectively. In effect, the observation of the far-field diffraction pattern intensity (and the subsequent transformation of the data back to the source-plane) acts as a spatial-filter for all but the dominant oscillating mode.

4.3.3.2 Comparison of data with dielectric-waveguide theory. The data for $\mathcal{J}'_F(x)$ are plotted on a semilogarithmic scale in Figure 4-3. This plot of $\mathcal{J}'_F(x)$ shows a cosine-squared decrease for small x , gradually changing to an exponential dependence which holds for an order of magnitude change in $\mathcal{J}'_F(x)$. Therefore, the general nature of the source intensity $\mathcal{J}'_F(x)$ is in accord with that predicted by the dielectric-waveguide theory (equation 1-72). The values obtained
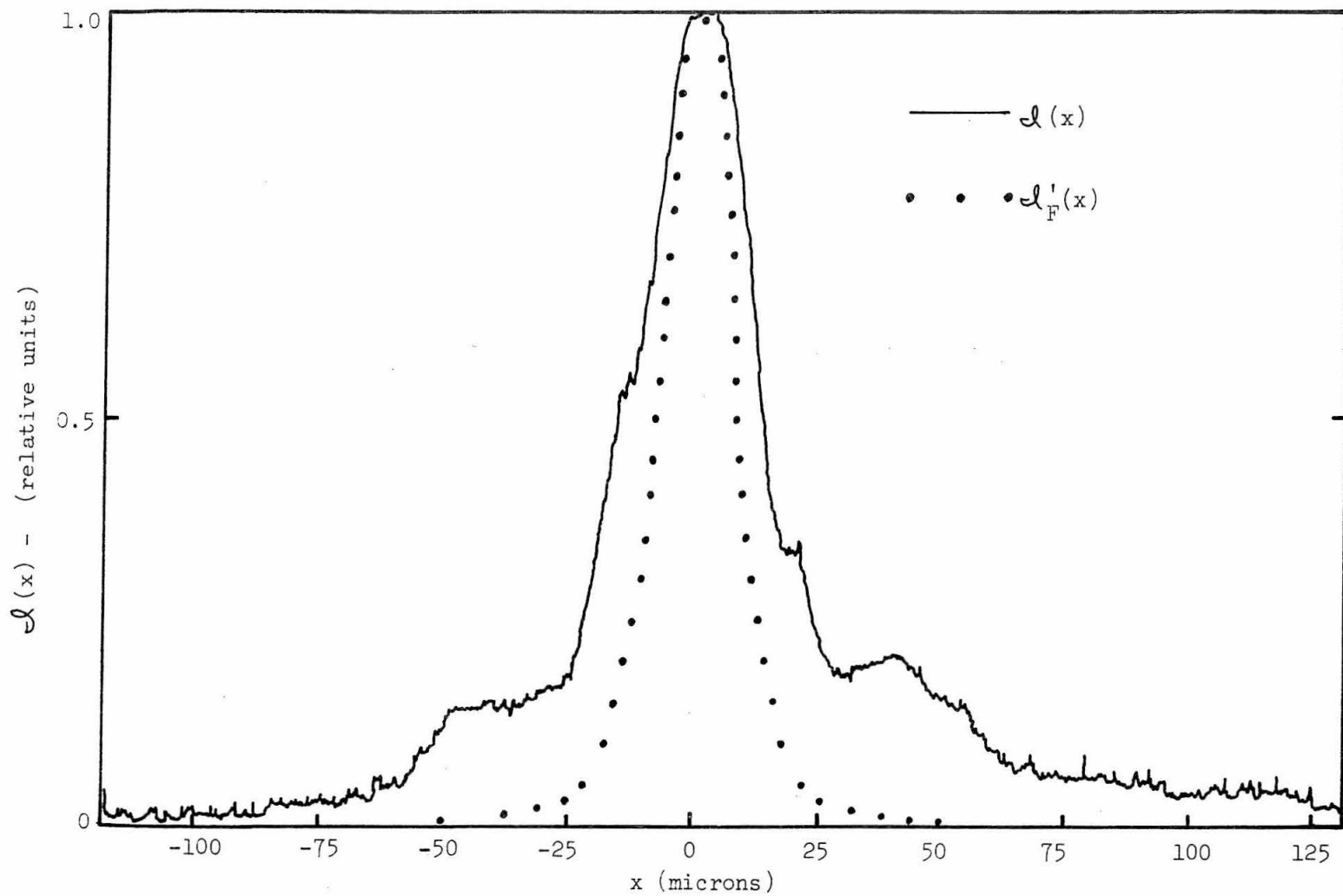
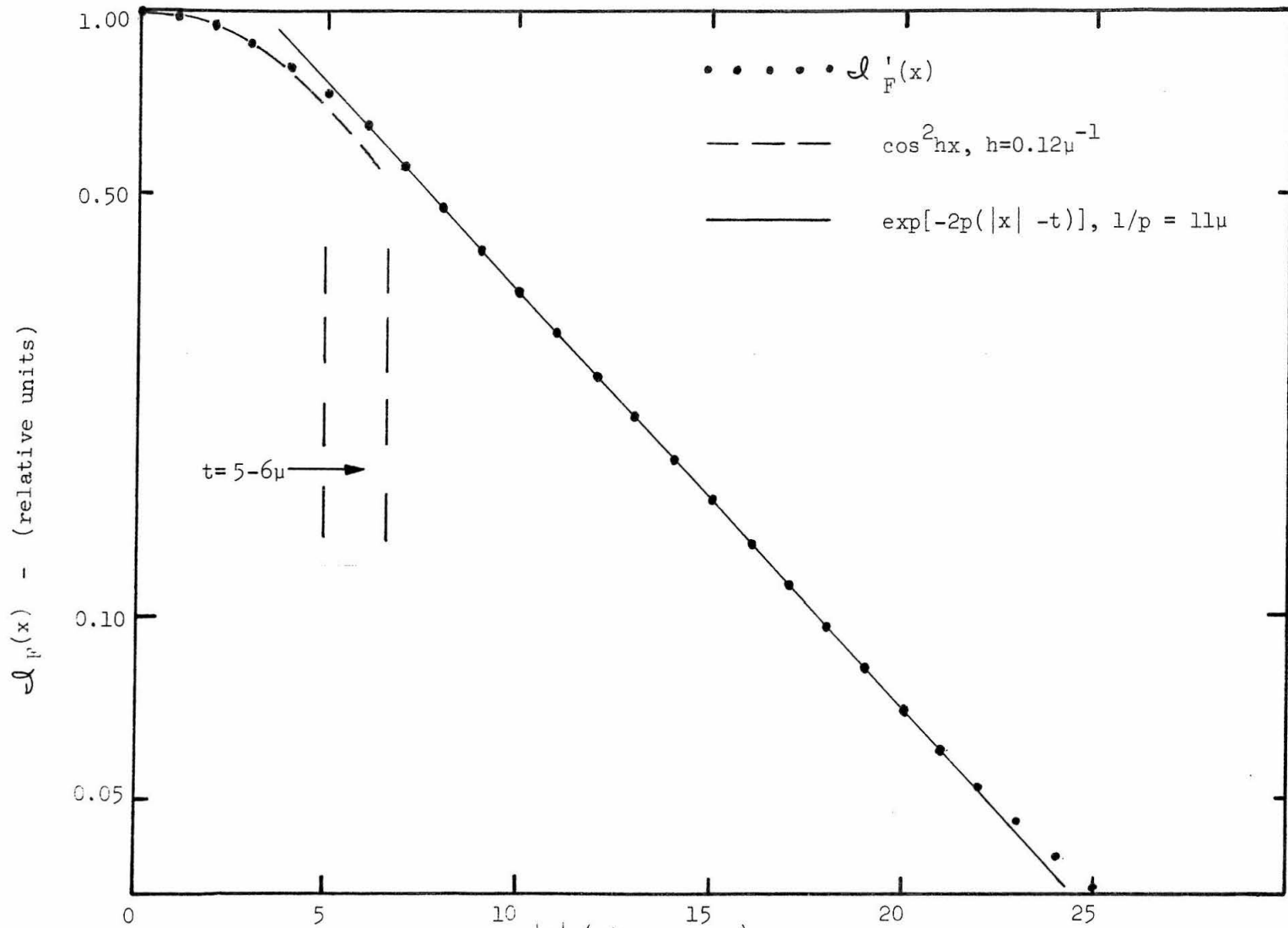Figure 4-2. Source Intensity Profiles for Diode K-4 (20.4°K)

Figure 4-3. $\log \mathcal{l}_F'(x)$ vs. $|x|$

from Figure 4-3 for the parameters in 1-72 are as follows:

$$t = 5-6\mu$$

$$h \simeq 0.12\mu^{-1}$$

$$1/p \simeq 11\mu \qquad\qquad (4\text{-}23a)$$

A self-consistency check can be made on the above experimentally determined parameters with the use of equation 1-71a. Using the values of h and p given by 4-23a, the corresponding value of t is

$$t = \frac{1}{h} \tan^{-1}(p/h) \simeq 5.3\mu \qquad\qquad (4\text{-}23b)$$

in good agreement with 4-23a. In addition, equation 1-71b may be used to calculate the dielectric discontinuity $(\delta\varepsilon/\varepsilon)$ in the diode cavity (Figure 1-4a); that is,

$$\frac{\delta\varepsilon}{\varepsilon} \equiv (K-1) = \frac{p^2 + h^2}{k^2} \simeq 2/3 \times 10^{-3} \qquad\qquad (4\text{-}24)$$

where $k = 2\pi n_r/\lambda$ and λ is the measured wavelength of the dominant oscillating mode. The numerical value for $(\delta\varepsilon/\varepsilon)$ in 4-24 indicates the smallness of the dielectric discontinuity needed for the confinement of electromagnetic modes.

    4.3.3.3 <u>The physical basis for mode confinement</u>. The physical mechanism which gives rise to the discontinuity $(\delta\varepsilon/\varepsilon)$ in the real part of the dielectric constant of semiconductor-diode lasers has been studied by several investigators (33). One such mechanism is based on the enhancement of the dielectric constant in the depletion region

about the diode junction, due to the absence of free charge carriers. The corresponding dielectric discontinuity is given by (34)

$$\frac{\delta\epsilon}{\epsilon} = \frac{\omega_p^2}{\omega^2} \qquad (4\text{-}25a)$$

where ω is the radiation frequency and ω_p (called the plasma frequency) is given by

$$\omega_p^2 \equiv \frac{Nq^2}{m^*\epsilon} \qquad (4\text{-}25b)$$

where N is the density of the free charge carriers outside the depletion region and m* is their effective mass. The extent of the region of high dielectric constant (thickness 2t in Figure 1-4a) is therefore just the width (w) of the depletion region, given by equation 1-53. The capacitance measurements (Figure 3-7) indicate that with the high forward current flow needed for laser action, the width of the depletion layer is less than 0.1μ . However, the data illustrated in Figure 4-2 indicate the value for 2t to be on the order of 10μ . Therefore, the observed thickness of the high intensity region precludes the physical origin of $(\delta\epsilon/\epsilon)$ as prescribed by 4-18.

It is intuitively reasonable to expect that the high gain characteristics needed for laser action might somehow determine the extent of the region of high intensity in the diode structure. We have already seen from equation 1-56 and Figure 1-3b that the region of population inversion can extend out to roughly a diffusion length (L_D) on either side of the junction. However, without some means of confining the radiation within the cavity, the EM modes could "spread out"

over the total volume of the diode. Therefore, one is motivated to look for a mechanism whereby the cavity modes are confined to a volume which is at least approximately coincident with the volume of high gain (as determined by the minority carrier diffusion lengths). In this mechanism the change in the dielectric constant should be directly related to the gain characteristics of the medium. Such a mechanism has been applied to the case of GaAs laser diodes (35), and is discussed in the next paragraph.

The possible effect of the gain in a light-emitting diode on the dielectric constant can be seen by examining the Maxwell equation

$$\vec{\nabla} \times \vec{H} = \sigma\vec{E} + \epsilon \frac{\partial \vec{E}}{\partial t} \qquad (4\text{-}26a)$$

For a sinusoidal variation of $\vec{E}$ with time (t) of $\exp(i\omega t)$, 4-26a becomes'

$$\vec{\nabla} \times \vec{H} = \sigma\vec{E} + i\omega\epsilon\vec{E} \qquad (4\text{-}26b)$$

where σ is the electrical conductivity of the medium. Considering σ to be complex (i.e. $\sigma = \sigma_r + i\sigma_i$), we may write

$$\vec{\nabla} \times \vec{H} = i\omega\epsilon' \vec{E} \qquad (4\text{-}26c)$$

where ϵ' is the effective complex dielectric constant given by

$$\epsilon' = \epsilon_r + i\epsilon_i$$

with

$$\epsilon_r = \epsilon[1 + (\sigma_i/\omega\epsilon)] \qquad (4\text{-}26d)$$

and

$$\epsilon_i = -(\sigma_r/\omega)$$

From 4-26d we see that the fractional change in the <u>real part</u> of the dielectric constant, due to a complex conductivity, is

$$\frac{\delta\varepsilon}{\varepsilon} = \frac{\sigma_i}{\omega\varepsilon} \tag{4-26e}$$

Since the real part of the conductivity (σ_r) is associated with the ordinary loss of the medium (e.g. joule heating), the gain region of the cavity is characterized by $\sigma_r < 0$. The quantity σ_r may be expressed in terms of the total (exponential) intensity loss coefficient, α_t ($\mathcal{Q} \sim e^{-\alpha_t z}$). For the case where $(\delta\varepsilon/\varepsilon) \ll 1$ (already satisfied in 4-24), σ_r is given by

$$\sigma_r = \frac{\alpha_t \omega\varepsilon}{k} \tag{4-26f}$$

We next require that the power generated in the gain region of thickness (2t) equal the power loss in the surrounding "lossy" region of thickness (2/p) (in order for stimulated emission to occur). The required power balance is expressed as

$$\frac{2}{p} \left(\frac{1}{2}|\sigma_r^\ell|E_{mode}^2\right) = (2t) \left(\frac{1}{2}|\sigma_r^g|E_{mode}^2\right) \tag{4-27a}$$

where E_{mode} is the amplitude of the electric field due to the oscillating mode(s). With the approximation that E_{mode} is constant over the total mode volume, 4-27a becomes

$$|\sigma_r^g| = \frac{|\sigma_r^\ell|}{pt} \tag{4-27b}$$

where σ_r^g and σ_r^ℓ are the real parts of the conductivity for the gain

and loss regions, respectively. Using 4-26f, we may write

$$\left|\sigma_r^g\right| = \frac{\alpha_t \epsilon \omega_{mode}}{kpt} \qquad (4\text{-}27c)$$

where ω_{mode} is the oscillating-mode frequency, and k is the propagation constant $(2\pi n_r/\lambda)$. Now, the real and imaginary parts of the conductivity are related via the Kramers-Kronig relations (36). For the case of a Lorentzian dependence of $\sigma_r(\omega)$ on ω, it can be shown that $\left|\sigma_i(\omega_{mode})\right| \approx \frac{1}{2}\left|\sigma_r(\omega_{mode})\right|$ is required in order to achieve the power balance in equation 4-27a. It then follows from 4-26e and 4-27c that

$$\frac{\delta \epsilon}{\epsilon} = \frac{\left|\sigma_i^g\right|}{\epsilon \omega_{mode}} \approx \frac{\alpha_t}{2\, kpt} \qquad (4\text{-}28)$$

Since $(\delta \epsilon/\epsilon) \equiv (K-1)$ we may obtain from the boundary condition of equation 1-71b the following equation for $(1/p)$:

$$(1/p)^3 - \frac{2h^2 t}{\alpha_t k}(1/p)^2 - \frac{2t}{\alpha_t k} = 0 \qquad (4\text{-}29a)$$

Using the experimentally determined values of h, t and k from Section 4.3.3.2, and a value of $\alpha_t = 50$ cm^{-1} (independently obtained for diode K-4 as discussed in the following section, 4.3.4) a numerical solution for $(1/p)$ in 4-29a yields the value

$$(1/p) = 10\text{-}11\mu \qquad (4\text{-}29b)$$

This independent value for $(1/p)$ is in good agreement with the value given by 4-23a, thereby adding credence to the above physical mechanism for mode confinement.

With the premise that the gain region extends to approximately a diffusion length on either side of the junction, it then follows from the experimental data that

$$L_D \simeq t \simeq 6\mu \qquad (4\text{-}30\text{a})$$

From equation 1-56b it follows that

$$\tau = \frac{L_D^2}{D} \qquad (4\text{-}30\text{b})$$

where τ is the minority carrier lifetime and D is the minority carrier diffusion constant. By extrapolating the experimental mobility (μ) data of (37) to 20.4°K, and obtaining D from the Einstein relation ($\mu/D = q/kT$), the value of τ calculated from 4-30a,b is

$$\tau \approx 10^{-9} \text{ second} \qquad (4\text{-}30\text{c})$$

for a diode temperature of 20.4°K ($D \approx 400$ cm^2/sec). The "order of magnitude" value for τ given by 4-30c is in agreement with the value obtained from photo-induced recombination radiation experiments using single crystals of PbTe (38).

4.3.4 Threshold Current Analysis

4.3.4.1 Diode-parameter analysis. The expression developed in Section 1.3.3.2 for the threshold current density for stimulated emission (equation 1-66) may be written as

$$J_{th} = \beta(\alpha + \alpha') \qquad (4\text{-}31\text{a})$$

where

$$\beta \equiv \frac{8\pi q \ d\nu^2 \Delta\nu}{c^2 \ \xi \ \eta_s} \tag{4-31b}$$

and

$$\alpha' \equiv \frac{1}{L} \ \ell n(1/R) \tag{4-31c}$$

with all other quantities having been previously defined. The quantities α and α' represent the losses due to the cavity medium and the imperfect cavity-end reflection, respectively. In terms of the total loss factor (α_t) we may write

$$J_{th} = \beta \ \alpha_t \tag{4-32a}$$

where

$$\alpha_t \equiv \alpha + \alpha' \tag{4-32b}$$

It is also illuminating to express J_{th} as

$$J_{th} = J'_{th} + \beta\alpha' \tag{4-33a}$$

where

$$J'_{th} \equiv \beta\alpha \tag{4-33b}$$

is the threshold current density in the limit of an infinitely long cavity (i.e. for $\alpha' \sim \frac{1}{L} \approx 0$) .

The experimental determination of J_{th} as a function of α' for the set of "matched" diodes described in Section 3.7 is illustrated in Figure 3-16 (for a diode temperature of $20.4^\circ K$). The experimental results in Figure 3-15 yield the following values for three of the parameters defined above:

$$\alpha = (30 \pm 15) \ cm^{-1} \tag{4-34a}$$

$$\beta = (15 \pm 5) \ amp/cm \tag{4-34b}$$

$$J'_{th} = (400 \pm 80) \text{ amp/cm}^2 \qquad (4\text{-}34c)$$

Using equation 4-31b we may express the quantity $(\xi \eta_s)$ as

$$\xi \eta_s = \frac{8\pi q \ d\nu^2 \Delta \nu}{c^2 \beta} \qquad (4\text{-}35a)$$

From the total spread of stimulated modes observed in the emission spectra from PbTe diodes at $20.4^\circ K$, the spontaneous bandwidth $(\Delta \nu)$ is estimated to be

$$\frac{\Delta \nu}{\nu} \approx 10^{-2} \qquad (4\text{-}35b)$$

The width (d) of the volume which contains all of the oscillating modes is observed (Figure 3-11) to be in the range of $d = 50\text{-}100\mu$. It then follows from 4-35a,b, the measured value of ν from the stimulated emission spectra, and the range of values for β given by 4-34b, that

$$\xi \ \eta_s \approx 10^{-1} \qquad (4\text{-}35c)$$

For sufficiently low temperatures, it is valid to assume that $\xi \simeq 1$. Based on this assumption, we then have

$$\eta_s \approx 10^{-1} = 10\% \qquad (4\text{-}35d)$$

for the (internal) efficiency of spontaneous emission.

From equations 1-57b and 1-59c, we obtain the following expressions for the spontaneous lifetime (t_s) and the nonradiative lifetime (t_b) in terms of the minority carrier lifetime (τ) and η_s :

$$t_s = \frac{\tau}{\eta_s}$$

and

$$t_b = \frac{\tau}{(1-\eta_s)} \qquad (4\text{-}36a)$$

By using the empirical values for τ, 4-30c, and η_s, 4-35d, we obtain

$$t_s \approx 10^{-8} \text{ second}$$

and

$$t_b \approx \tau \approx 10^{-9} \text{ second} \qquad (4\text{-}36b)$$

for a temperature of 20.4°K.

The $\mathcal{L}$-I data in Figure 3-3 indicate a decrease of approximately 25% in the threshold current by decreasing the diode temperature from 20.4°K to 4.2°K. Equation 4-31 contains a number of parameters which may be temperature dependent (i.e. ν, $\Delta\nu$, ξ, η_s, etc.). However, the determination of the temperature dependence of each of these quantities between 20.4°K and 4.2°K would be an extensive effort by itself, and is not included herein. Therefore, the only conclusion which can be made here is that total effect of the temperature dependence of the diode parameters is to alter the threshold current as stated above.

4.3.4.2 Possible sources of diode-cavity loss (α). Two sources of loss which may contribute to the loss constant (α) of the diode-cavity are those due to (a) band-to-band absorption and (b) free-carrier absorption (39) of photons generated in the cavity.*

---

* A third loss mechanism, namely that of diffraction at the ends of the cavity, is essentially negated by the focussing effect (mode confinement) discussed in Section 4.3.3.

The minimum photon energy observed from the stimulated emission spectral data of PbTe diodes at 20.4°K is 0.191 ± 0.002 eV. This is in general agreement with the value for the band-gap given in Table 1-1. Therefore, the stimulated radiative transitions are apparently taking place between the edges of the conduction and valence bands. Now, the reverse process of band-to-band absorption (discussed in Section 1.2.1) is overcome in the region of high gain due to the population inversion obtained from minority carrier injection. Conversely, in the regions immediately surrounding the high gain volume, the rate of absorption may exceed the rate of emission, giving a net loss (photon absorption). However, in degenerate semiconductors there is an observed increase in the minimum photon energy which can be absorbed via band-to-band transitions (40). This effect (known as the Burstein shift) is a direct result of the complete filling of energy levels to within a few (kT) of the degenerate Fermi level, which, of course, lies within the conduction and/or valence band. Therefore, transitions due to photon absorption must take place between states within the conduction and/or valence bands, requiring photons with increased energy. On the other hand, radiative transitions can still occur between states near the band edges. For the case of electron injection into the p-side of the diode, the injected electrons occupy states at the edge of the conduction band. As the electrons diffuse into the p region, they can recombine radiatively with a hole at the edge of the valence band. Since the p-type material is degenerate, there are plenty of empty electron (hole) states near the edge of the valence band, into which conduction electrons can decay. In addition, the radiative

recombination of an electron-hole pair at the band edges is greatly favored by the conservation of "crystal" momentum (Section 1.2.3). As a result of the Burstein shift, it is possible that the effect of band-to-band absorption in the "lossy" regions of the radiating cavity is greatly reduced.

The effect of free-carrier absorption is of no significance in the depletion region of the diode (which is, of course, devoid of free carriers). However, this is countered by the increased absorption due to the electric fields present within the depletion region (Franz-Keldysh effect (41). Inasmuch as the depletion region accounts for roughly less than 1% of the total region of high mode intensity ($2t/W < 10^{-2}$ from Section 4.3.3.3), its net contribution to the cavity loss (α) is at most very small. This leaves only the free-carrier absorption outside the depletion region to be considered. On the basis of the estimate of α in equation 4.34 and the published empirical values for free-carrier absorption in PbTe at 20°K (42), it is possible to explain the cavity losses as being due to free-carrier absorption.

4.3.5 Calculation of the External (Stimulated) Quantum Efficiency

As a final exercise, it is interesting to estimate the external quantum efficiency for stimulated emission (i.e., the number of photons collected by the detector per carrier flowing through the diode junction) for a PbTe laser diode. The estimate given here is based on the calculation of η_d (equation 2-4) from the data contained in Figure 3-1 for diode J-2 at 20.4°K. Following equation 2-4, the stimulated quantum efficiency in the saturation region (D), in terms of the

detector-circuit parameters (Figure 2-7a), is given by

$$\eta_d = \frac{(\tau_t/\tau)}{\eta_D \ GR_L} \cdot \frac{d(\Delta V)}{dI} \qquad (4-37)$$

where τ_t is defined by 2-3b.

The quantity $d(\Delta V)/dI$ in 4-37 is the slope of the detector signal (ΔV) as a function of the diode current (I), as obtained from the ℓ-I data in region D . The numerical value of the slope for J-2 from Figure 3-1 is

$$\frac{d(\Delta V)}{dI} = 0.85 \text{ volts/amp} \qquad (4-38a)$$

The corresponding values for the detector parameters are

$$V_o = 40 \text{ volts}$$
$$R_L = 300 \text{ ohms} \qquad (4-38b)$$

The following numerical values are for the material parameters of the Ge:Hg detector at 20.4°K:[*]

$$\tau \simeq 10^{-8} \text{ second}$$
$$\mu_p \simeq 25 \times 10^3 \text{cm}^2/\text{volt-sec}$$
$$\eta_D \simeq 0.50$$
$$\ell = 0.40 \text{ cm}$$
$$G \simeq 1.00 \qquad (4-38c)$$

---

[*]The reference sources for these parameters are η_D and τ (43), and μ_p (44).

The value of τ_t resulting from equations 2-3b and 4-38b,c is

$$\tau_t \equiv \ell^2/\mu_p V_o \simeq 16 \times 10^{-8} \text{ second} \qquad (4\text{-}39)$$

The final value for η_d , as calculated from 4-37 and the above parameters, is

$$\eta_d \simeq 10\% \qquad (4\text{-}40)$$

Now the data in Figure 3-1 are due to radiation from only one end of the diode cavity. Therefore, the total calculated quantum efficiency due to radiation from both ends of the cavity is in the range of 10-20%. The corresponding radiative power of the stimulated light emission ($\lambda = 6.5\mu$) for a diode current of 6 amps is in the range of 120-240 milliwatts.

V. SUMMARY

The results of a number of experiments on the light emission and electrical characteristics of lead telluride p-n junction diodes have been presented. The capacitance-voltage data indicate that the vapor diffusion of an n-type layer into p-type bulk material produced an abrupt junction. At low current levels and temperatures (4.2°K to 20.4°K), the current-voltage data exhibit a temperature independent exponential variation of current with junction voltage. The current-voltage data, together with the total intensity data as a function of diode current, indicate that photon-assisted tunneling is the dominant injection mechanism at low current levels. As the ion current level is increased, the injection mechanism changes from photon-assisted tunneling to thermionic emission. The spontaneous emission of light in the thermionic injection region is apparently influenced by impurity trapping levels in the band-gap. Stimulated light emission occurs at high injection levels in those diodes where a reflecting cavity is formed by cleaving the ends of the crystal. The image-scan and far-field diffraction data indicate that the stimulated electromagnetic modes are confined to within approximately a diffusion length of the junction. The data indicate that the mode confinement is due to the optical gain in the diode cavity, a gain which obtains in the region where a population inversion exists. Therefore, both the gain and the mode profiles are diffusion controlled.

REFERENCES

1. J. R. Haynes and H. B. Briggs, Phys. Rev. 86, 647 (1952), Abstract.

2. J. P. Gordon, H. J. Zeiger and C. H. Townes, Phys. Rev. 95, 282 (1954).

3. R. N. Hall et al, Phys. Rev. Letters 9, 366 (1962); M. I. Nathan et al, Appl. Phys. Letters 1, 62 (1962); T. M. Quist et al, ibid, p. 91.

4. M. I. Nathan, Applied Optics 5, 1514 (1966).

5. J. F. Butler et al, Appl. Phys. Letters 5, 75 (1964).

6. C. A. Hogarth, Materials Used in Semiconductor Devices, Interscience Publishers, New York 1965, p. 109.

7. D. L. Mitchell, E. D. Palik and J. N. Zemel, Physics of Semiconductors, (edited by M. Hulin), Dunod, Paris 1964, p. 677.

8. K. F. Cuff, M. R. Ellet, C. D. Kuglin and L. R. Williams, ibid., p. 325.

9. E. R. Washwell and K. F. Cuff, Radiative Recombination in Semiconductors, Dunod, Paris 1964, p. 11.

10. R. N. Tauber, A. A. Machonis and I. B. Cadoff, J. Appl. Phys. 37, 4855 (1966).

11. A. K. Walton and T. S. Moss, Proc. Phys. Soc. 81, 509 (1963).

12. E. G. Bylander and M. Hass, Solid State Communications 4, 51 (1966).

13. F. A. Junga (private communication).

14. Y. Sato, M. Fujimoto and A. Kobayashi, Jap. J. Appl. Phys. 2, 688 (1963).

15. W. W. Scanlon, Phys. Rev. 126, 509 (1962).

16. A. Einstein, Phys. Z. 18, 121 (1917).

17. A. Yariv, Quantum Electronics, John Wiley and Sons, New York 1967, Chapter 13.

18. D. Dewitt and A. L. Rossoff, Transistor Electronics, McGraw-Hill, New York 1957, p. 68.

19. C. T. Sah, R. N. Noyce and W. Shockley, Proc. IRE 45, 1228 (1957).

20. M. G. A. Bernard and G. Durraffourg, Physica Status Solidi 1, 659 (1961).

21. W. V. Smith and P. P. Sorokin, The Laser, McGraw-Hill, New York 1966, p. 393.

22. A. Yariv, ibid., pp. 287-289.

23. J. D. Jackson, Classical Electrodynamics, John Wiley and Sons, New York 1962, p. 287. (Equation 1-73a in the text follows directly from equation 9.82 of this reference).

24. R. C. C. Leite et al, Phys. Rev. 137, A1583 (1965).

25. C. A. Mead, Solid-State Electronics 9, 1023 (1966).

26. J. F. Butler, J. Electrochem. Soc. 111, 1151 (1964).

27. M. Hansen, Constitution of Binary Alloys, McGraw-Hill, New York 1958, p. 239.

28. M. Ludwick, Indium, The Indium Corp. of America, 1959, pp. 136-139.

29. W. D. Lawson, J. Appl. Phys. 22, 1444 (1951).

30. L. R. Williams (private communication) and J. A. Zoutendyk (unpublished data).

31. D. Dewitt and A. L. Rossoff, ibid, p. 75.

32. A. K. Walton and T. S. Moss (reference 11).

33. A. Yariv, ibid., p. 290.

34. W. L. Bond et al, Appl. Phys. Letters 2, 57 (1963).

35. R. C. C. Leite and A. Yariv, Proc. IEEE 51, 1035 (1963).

36. A. Yariv, ibid., Appendix 1.

37. K. Shogenji and S. Uchiyama, J. Phys. Soc. Jap $\underline{12}$, 252 (1957).

38. F. A. Junga et al, Phys. Letters $\underline{13}$, 103 (1964).

39. R. A. Smith, Semiconductors, Cambridge University Press 1961, p. 216.

40. E. Burstein, Phys. Rev. $\underline{93}$, 632 (1954).

41. K. Tharmalingam, Phys. Rev. $\underline{130}$, 2204 (1963).

42. A. F. Gibson, Proc. Phys. Soc. London $\underline{65B}$, 378 (1952).

43. P. Bratt (private communication).

44. A. Yariv (unpublished data).

List of Figure Captions